ATTRACTORS
IN STRATIFIED FLUIDS

AANTREKKERS
IN GELAAGDE VLOEISTOFFEN

(met een samenvatting in het Nederlands)

PROEFSCHRIFT

ter verkrijging van de graad van doctor aan de Universiteit Utrecht
op gezag van de rector magnificus, prof.dr. J.C. Stoof,
ingevolge het besluit van het college voor promoties
in het openbaar te verdedigen op
vrijdag 12 maart 2010 des middags te 12.45 uur

door

JEROEN HAZEWINKEL

geboren op 20 december 1980 te Nijmegen

Promotoren:
Prof.dr. L.R.M. Maas
Prof.dr. A. Doelman
Co-promotor:
Dr. S.B. Dalziel

I don't like being stationary,
I like the rocky wavy motion of the sea.
Tracy Chapman

NIOZ Koninklijk Nederlands Instituut voor Zeeonderzoek

UNIVERSITY OF
CAMBRIDGE

CWI
Centrum Wiskunde & Informatica

Contents

Chapter 1

Introduction

Thinking of waves, we see waves on the water, breaking when they come too close to the shore. Rippling on the water, circles that spread out more and more. But below the surface, waves get serious and their behaviour really mysterious: characteristics that span the fluid like a maze, and their motion fills this aquatic space.

This thesis is about waves below the surface of a fluid, called internal waves. More specifically, the focus is on internal waves in a fluid that is confined to a domain. Considering confined fluids may seem an obvious choice. Fluids have no natural shape of their own, and always take the shape of their confinement. Given that internal waves occur inside the fluid, it seems therefore a natural question to ask what a confinement does to the internal waves. However, rather surprisingly, most studies of internal waves take the liberty to position the investigation of internal waves in a (semi) infinite domain, e.g. an infinitely long channel. Although this is mathematically easier to access, such a choice does not make the theory more realistic or natural. That confinement renders the mathematical description more difficult is because it plays an important role at a very fundamental level. This important role of the confinement on the internal waves is of key importance to understand internal wave patterns in fluids as measured in the laboratory and in the ocean.

The investigation of internal waves, as presented in this thesis, starts by examining their natural occurrence and some fundamental aspects. Most of the work in this thesis is of an experimental nature, hence extra attention will be paid to previous laboratory experiments. Of course, it is still illuminating to start the investigation on internal waves when boundary reflections play no role yet; i.e. in an infinite domain. But it will become clear that the limiting effect of a confined domain leads to unexpected dynamics, the formation of internal wave attractors.

1.1   Internal waves

As an example of an internal wave, let us start with a fluid having two densities, where the fluid with the highest density is lowest in the container. Between the layers of fluid there is
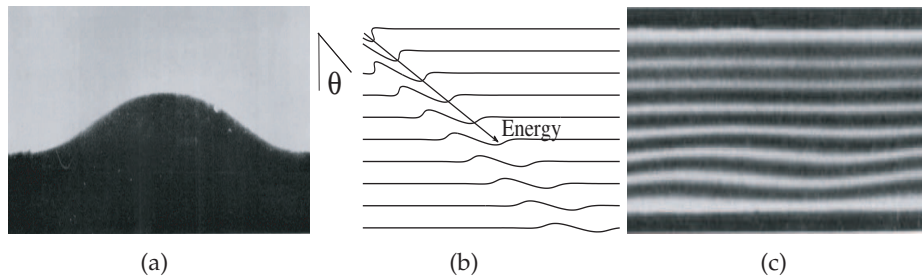
Figure 1.1: Internal waves in the laboratory for a) a two-layer fluid and c) a continuously stratified fluid, *Thorpe* (1968). b) A schematic illustration of the propagation of waves in a many layer fluid.

now an interface along which waves can propagate, similar to waves on the surface of a fluid. The difference in densities determines how strong the restoring force is, and subsequently, how high amplitudes can grow for a given (gentle) forcing and how long wave periods can be. The smaller the difference the higher the amplitude may become. The simplest home experiment to see this type of internal waves is in a transparent cup of hot coffee in which cold milk is poured gently down the sides. On the interface between the white layer (milk) and the black layer (coffee) waves will be seen. Although these waves are inside the fluid, they are still restricted to the interface, a more precise name therefore is 'internal interfacial gravity waves'. In the more advanced setting of a controlled laboratory experiment, large amplitude waves are found when two-layer fluids are subjected to some sort of sloshing, an example is given in figure 1.1a.

When more layers with different densities are involved, the waves on one interface will act on the next interface, that can in turn affect yet another interface. That waves exist in this fluid is a result of the stratification in a field of gravity. The stratification ensures that every bit of fluid that is displaced into another layer is either lighter or heavier than its surroundings. This means that gravity or buoyancy will act to bring the distorted fluid back to its level of neutral buoyancy, but, in doing so, will overshoot due to inertia, thereby reversing the situation; resulting in an oscillation. When no layers are present but rather a smooth increase in density, a continuous stratification, internal gravity waves have now lost their resemblance with interfacial waves. Rather curiously their energy propagates under an angle θ with the vertical, the direction into which gravity works. This is understood when we think again in layers, but many of them. Now a disturbance in one layer is not isolated from the rest of the fluid anymore as the full depth of the fluid is connected by the interaction of the layers. This is sketched in figure 1.1b where the grey lines indicate lines of equal density, the initial disturbance is visible at the top left. A wave traveling to the right at the top pushes the layer below also to the right in a similar shape, and this layer affects in turn the layer below that one etc etc. The disturbance at the top effectively propagates obliquely into the fluid, rather than forward along the top interface. In the limit with an infinite amount of layers, giving a gradual density change, the waves have now become true internal waves that can travel throughout the whole depth of the fluid. An example of an internal wave is given by a snapshot of a laboratory experiment where the stratification is made visible by dyelines, figure 1.1c.

1.2 The ocean and its laboratory models

Why would one be interested in waves in fluids that are stratified? A motivation comes from oceanography; the ocean is a density stratified fluid in which underwater waves are found. The oceans are stratified in density as a result of many geophysical processes, like evaporation, cooling, mixing with fresh meltwater, *etc*, playing a role at different locations on earth. Over millions of years, all these processes have created an ocean that below the restless surface layer has a gradually increasing density with depth. One might expect that below the surface things are quiet and no waves exist, but the opposite is true. The largest waves of the ocean are found under water. In the regions with a strong local change in density, internal waves have been observed to take a similar shape as surface waves, but with amplitudes well over 10 m. In the more gradually stratified regions of the ocean, typically the deeper parts, the waves lack such a density interface to travel along. Especially in regions with rough topography, such as continental slopes and underwater ridges, strong wave motion is observed with vertical displacements over 100 m. These strong motions have a very localised structure in the vertical (*Pingree and New*, 1991; *Lam et al.*, 2004; *Gerkema et al.*, 2004; *Cole et al.*, 2009). The wave energy propagates into the abyss, the deeper parts of the ocean. This region is exactly where our understanding of the ocean dynamics is lacking. Assessment of the structure of the abyssal ocean revealed that a certain amount of mixing is needed to maintain the observed stratification (*Munk and Wunsch*, 1998). The observed average rate of mixing is too low to do this. Thus, other more localised mixing processes are needed. Given the very localised structure of internal waves, they became prime suspect to play a role in mixing the deep ocean. Measurements in regions in the ocean with rough topography reveal that enhanced mixing is found, assumed to be related to internal wave breaking and dissipation (*Ledwell et al.*, 2000).

In order to understand internal wave generation and dynamics in a more controlled situation than in the oceans, many laboratory experiments have been performed. In the laboratory, the ocean is reduced to a fluid with a stratification, some forcing and some topography. Oftentimes the experiments were designed such that one of the spatial dimensions was irrelevant, making the experiments essentially two-dimensional. The interest in recent laboratory studies on oceanic internal waves has been on conversion of the barotropic tides, with a vertically uniform velocity profile, into baroclinic internal waves, whose velocity field varies with depth, moving particles under an angle with the lines of constant density. Experiments investigating the generation of internal waves from a model continental slope (*Gostiaux et al.*, 2006) or model ocean ridge (*Echeverri et al.*, 2009), showed that internal waves are indeed created near these locations, see figure 1.2. The waves are found to be restricted to very localised regions and look like beams emanating from the topography. Away from the topography, this very localised structure decayed into broader and much weaker motion (*Echeverri et al.*, 2009). Other mechanisms to break up the structure of the beams, were found to be reflections from small scale rough topography or from changes in the stratification (*Marthur and Peacock*, 2009; *Nye*, 2009). The reflection from a very strong change in density, representing the ocean's thermocline, could result in the local generation of internal solitary waves on that interface (*Gerkema*, 2001). So, most of these studies suggest that the conversion of the tide into the wavebeams happens very close to rough topography and that these wave beams rapidly transform into much weaker horizontal oscillations throughout the whole depth, so-called internal wave modes.
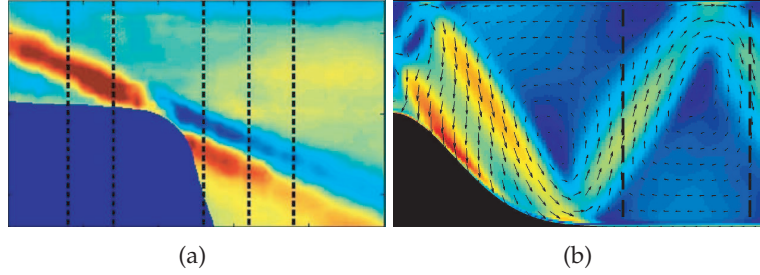
Figure 1.2: Laboratory observations of internal wave beams emanating from idealised topographies. Left a model continental slope *Gostiaux et al.* (2006) and right a model oceanridge *Echeverri et al.* (2009). In these vertical sections, the colour red indicates strong wave motion.

This indicates that the beams would play a limited role in the dynamics as they decay rapidly. However, in all experiments in the laboratory, very special care had to be taken that reflections from the sidewalls were eliminated. The idea was that the ocean is large and that reflections could not play any role of importance. In this thesis we will find that these reflections are very important nevertheless.

1.3 Stratified fluid in the laboratory

One could reduce the stratified ocean further to being in essence an almost two-dimensional stratified fluid with some sort of forcing. Consider a linearly density stratified fluid and an oscillating plate near the surface of the fluid (*Görtler*, 1943), see figure 1.3a. From this plate, the internal waves were found to propagate as beams in two vertical directions under the earlier mentioned angle θ. The inclined black and white bands in the figure indicate positive and negative distortions of the equilibrium density profile. Motions are in opposite direction on each side of the beam and the phase of the waves propagates perpendicular to the beams. This means that in one beam, the locations with upward motion (black regions of figure 1.3) turn into downward motions (white) half a period later. The particle excursion during a period is twice the amplitude of the wave. Lines of equal phase are thus along the beam and energy propagates along these phase lines (as the energy travels away from the source). In a similar setting, but with an oscillating bar reaching the middle of the fluid, the waves propagate out in a cross, the St Andrews cross (*Mowbray and Rarity*, 1967), see figure 1.3. In these experiments the vertical black line in the middle is the shadow of the oscillating bar. The experiments show that for a given forcing frequency, four typical or characteristic directions exist. Changing the frequency of the oscillation leads to a different angle of the beams, as seen comparing b) and c), where the last has the higher frequency. The higher the forcing frequency becomes, the smaller θ. When the frequency is too high, the fluid can no longer follow the oscillation and the waves do not radiate out anymore, they have become evanescent waves (*Gordon and Stevenson*, 1972).

Based on the observations of internal wave beams, theoretical predictions for the far field of a two-dimensional viscous fluid were developed (*Thomas and Stevenson*, 1972; *Hurley*, 1969;
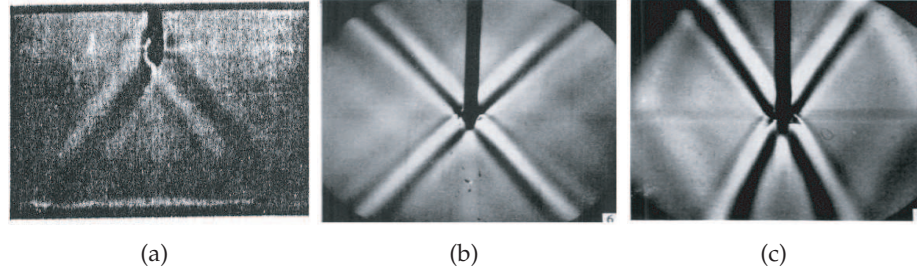
<div align="center">(a)   (b)   (c)</div>

Figure 1.3: Laboratory observations of internal wave beams by a) *Görtler* (1943) and b,c) *Mowbray and Rarity* (1967). All side views show that an oscillation in a linearly stratified fluid leads to internal waves in the shape of beams. The black and white bands indicate positive and negative distortions of the equilibrium density profile.

Hurley and Keady, 1997; *Tabaei and Akylas*, 2003; *Voisin*, 2003). With this theory we can now better understand the velocity fields and their beam structure, see figure 1.4. There is a point source in the lower left corner of this picture. The velocity field, arrows in figure a), show that the motion is in the opposite direction on each side of the beam, also called shear motion. The black and white background colour is similar to the pictures in figure 1.3. An indicative representation of the density field of the same wave is given in 1.4b. The internal wave is where the lines of equal density are distorted compared to their equilibrium position, the horizontal lines outside the beam. Experiments in a stratified fluid with oscillating sources of various shape, such as cylinders, all confirm the theoretical predictions concerning the beam structure, see recent experiments by *Dalziel et al.* (2000); *Sutherland et al.* (1999); *Ermanyuk and Gavrilov* (2008); *Nye* (2009). The fact that the viscous theory compared well with the experiments reveals that viscosity is important in the dynamics of internal waves (at least in the laboratory). Viscosity is a measure of the resistance of a fluid which is being deformed; the 'thickness' of a fluid (e.g. compare honey (thick) and water (thin)). The effect of viscosity is mainly the dissipation of the small scale shear structures in the beam such that away from the source the wave amplitude gets smaller and the beam broader.

Arguably the above reduction of the ocean to a two-dimensional stratified fluid in an unbounded domain with a localised forcing is a bit too much of a simplification. Clearly the experiments were performed in enclosed domains, and boundary reflections of the waves were already seen in some of the experimental examples. To investigate the effect of boundaries on a stratified fluid with forcing, we will neglect the effect of viscosity first and focus solely on the reflection of two-dimensional internal waves. Later on the damping effect of viscosity is reconsidered.

1.4 Reflection, the effect of boundaries

We observed that, in a constantly stratified fluid, an internal wave of frequency ω propagates at a fixed inclination of angle θ. We therefore will also refer to it as a monoclinical wave (*Whitham*, 1974; *Maas*, 2005). It is useful to study reflections of these monoclinical waves by studying

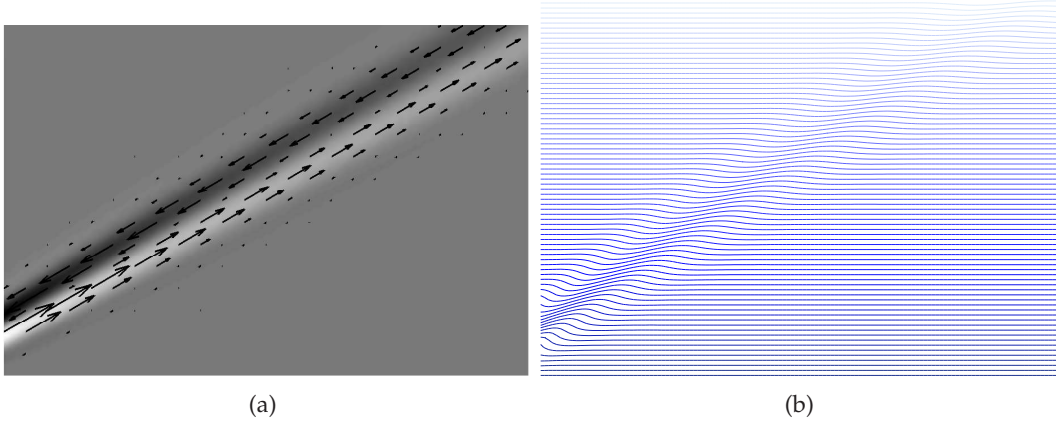(a)   (b)

Figure 1.4: Internal wave beam as found from viscous theory. a) Velocity arrows and comparison with beam structure in figure 1.3. b) Iso density lines of the same wave.

the reflections of rays, the paths along which the energy can travel (*Longuet-Higgins*, 1969a; *Hurley*, 1969; *Baines*, 1973). Bringing back to mind the four directions of the St. Andrews cross, 1.3b, we have four characteristic directions of these paths. A reflection of a ray then simply means a change of direction along one of the other paths (the wave has to remain inside the fluid domain). This also means that upon reflection the ray will preserve the angle with the vertical, disregarding the orientation of the boundary upon which it reflects. Ray tracing is simply following the wave beams, reduced to rays, in mathematics known as characteristics. The unusual behaviour of internal wave reflection is not clear when considering the reflection of internal waves on a horizontal or vertical boundary. Following the incoming characteristics, red arrows in figure 1.5, we see that one of the wave vector components changes sign, blue arrows. It seems that the reflection is the standard specular reflection where the angle with the normal to the reflector is preserved. This picture changes when the reflection from a sloping boundary (with angle α relative to the vertical) is considered, see figure 1.5b. Now the reflected blue rays are much closer together than the incoming red rays, in other words the internal waves get focussed. If we reverse the arrows, and follow an incoming beam consisting of blue rays, we see defocussing upon reflection from the sloping boundary.

When we interpret the distance between the incident rays as wave length λ_{in} we see that upon reflection the wavelength has changed to λ_{out}. Assuming that no energy is lost in the reflection, the wave energy is confined to a much narrower area. This indicates that the wave amplitude (particle excursion) is increased after a focussing reflection while being decreased upon defocussing reflection. An internal wave reflection from a slope can be interpreted as both an energy transfer from one wavelength to another and as a corresponding change of internal wave intensity.
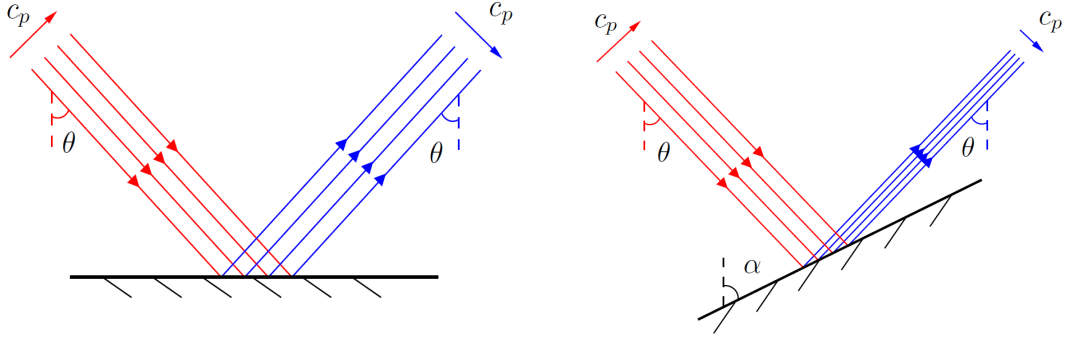
Figure 1.5: Ray tracing for reflection from horizontal boundary (left) and sloping boundary (sloping angle α) (right). Reflection of internal waves from a slope leads to focussing when the wave propagates to the right (or defocussing when propagating to the left). The direction of phase propagation c_p is indicated by cross beam arrows.

1.5 Attractors

Now we finally come to the main topic of this thesis: how do the internal waves behave in a confined stratified fluid? Having seen the reflection from the slope, let us consider a two-dimensional container with one sloping wall and the three other walls being horizontal or vertical. Again, we consider ray tracing, for the moment without asking where the waves come from. Starting from two positions at the top, red and blue in figure 1.6a, we follow the rays through the domain and see that after many reflections they end up at a periodic orbit, denoted in black. In fact, regardless of where we would have started or in which direction (left or right), this is where the rays will end: at the internal wave attractor. As the energy of the waves propagates along the rays, the attractor is also the limit cycle where wave energy is going to end; the attractor attracts all energy.

The fact that many domains have internal wave attractors was found by *Maas and Lam* (1995). The example presented here is a very simple version of such an attractor. As wave angle θ depends on the stratification and the forcing frequency, we can vary one or both of these two to find different attractor shapes. Two more examples are given in figure 1.6b,c where now only the attractor is shown by the black lines. Scanning through a whole range of angles and plotting only the attractor's reflections from one boundary of the domain, we find an overview as presented in a so-called Poincaré plot, see figure 1.7a. The black dots thus denote the position of the reflections of the attractor at one boundary, as is shown in figure 1.7b. When the attractor is simple, the number of reflections is limited, sometimes just one as in figure 1.6a. Below the Poincaré plot some attractors are presented in gray lines. There are clear intervals of θ in which we find simple attractors, having a small number of reflections, in between regions of complicated attractors.

How do we interpret that rays converge onto an internal wave attractor? It means that

(a)

(b)   (c)
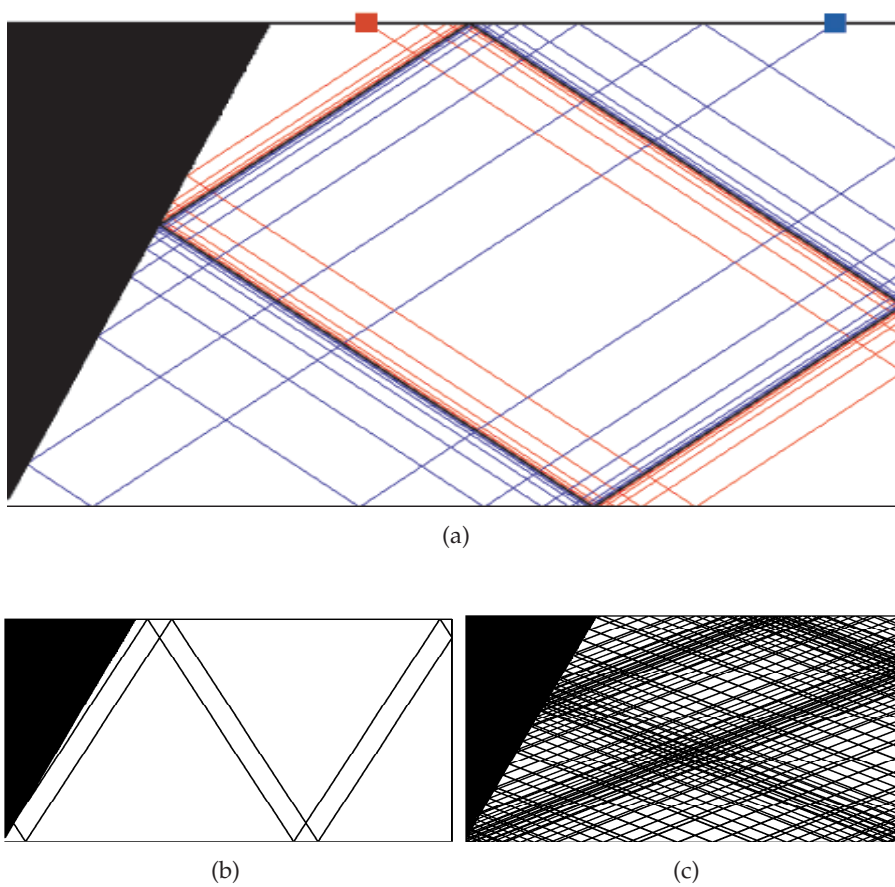
Figure 1.6: Ray tracing in a trapezoidal domain. Rays from two different starting points, red and blue rectangles, converge onto the black orbit; the internal wave attractor. Two more attractors are shown for rays under another angle of propagation (this means for different frequencies).
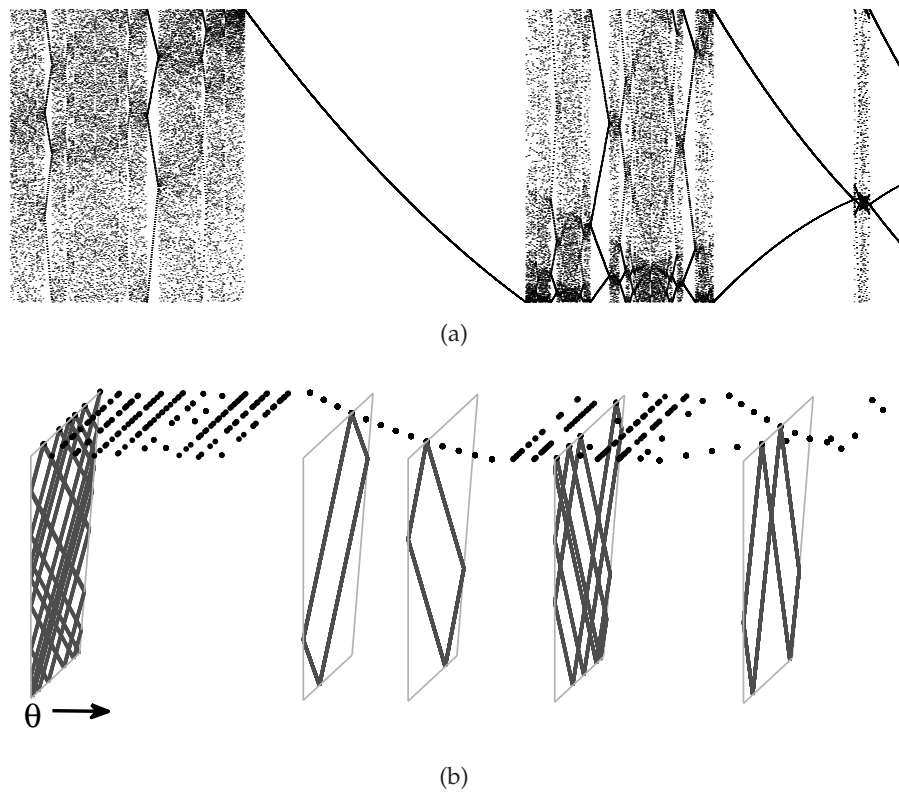
Figure 1.7: Plot of the position of boundary reflections of the attractors. Different propagation angles θ (and thus different frequencies) give a Poincaré plot (the black dots in a) and b)). In b) some attractors are plotted in perspective below to illustrate the difference between complicated attractors and simple attractors. a) is the high resolution top-view of b).

whenever waves are forced at a given frequency in the stratified fluid confined by the trapezoidal domain, they will eventually focus onto the attractor. However, as we have seen for the single reflection of a wave beam, the wavelength is also changed. This means that while the waves reflect towards the attractor, the wavelength get smaller and smaller. But, assuming energy conservation, at the same time their amplitude gets larger and larger. Intuitively, it is clear that something must be missing. Indeed, ray tracing does not take into account the damping by viscosity that, as mentioned before, damps the smaller scales much more effectively than the larger scales. Also wave breaking limits the growth in amplitude and leads to overturning and mixing of the stratification. So, for any realistic fluid there will be some limit to the focussing of the energy and the decrease of the wave length.

The confining domain does not have to be trapezoidal for there to be an attractor. Many examples are given by *Maas and Lam* (1995) including e.g. parabolic domains. Actually it is difficult to find any domain without attractors. The only exception is the situation where the focussing reflections are compensated by defocussing reflections, or if there are no focussing reflections at all. Examples of such domains are the circle and the 'non-tilted' rectangle. In both cases the rays always loop back onto the starting point and standing wave solutions can be found. The slightest geometrical departure from these domain shapes leads to attractors.

1.6   Internal wave attractors in the laboratory

The existence of internal wave attractors as predicted by the inviscid, two-dimensional ray tracing cannot be tested exactly in a real fluid. Real fluids occupy three dimensions and are viscous. Nevertheless, attractors were still found in a narrow trapezoidal tank containing a linearly stratified fluid (*Maas et al.*, 1997). The tank was oscillated and, although the whole fluid was forced by the oscillation, only very locally wave motion was observed. Re-analysis of the data (*Lam and Maas*, 2008) showed exponential growth over many periods that reached saturation only when the waves started to break.

This thesis will build further on this work. We oscillate a narrow trapezoidal tank, such that in the tank a small sloshing of the fluid surface is forced. This sloshing is then converted into internal waves at the sloping wall that subsequently reflect at the sidewalls and form the attractor, some are observations shown in figure 1.8. We will investigate how the attractor grows from rest and what the structure of the wavefield is. It will turn out that the wave beams of the attractor are very similar to the beams forced by an oscillating cylinder and have a surprising way of decaying once the forcing of the tank is halted. In subsequent chapters we will investigate whether the two-dimensional description is valid for our narrow tank (given that most of the above considerations assumed this) and compare the laboratory finding with the simulation of a numerical model. Having confirmed that our two-dimensional approximation is accurate, we study the existence of the attractors when the attractor shape is different from the simple orbit shown in figure 1.6a. We also consider different domains and stratifications and conclude that attractors are essential in the dynamics of stratified fluid in narrow tanks.
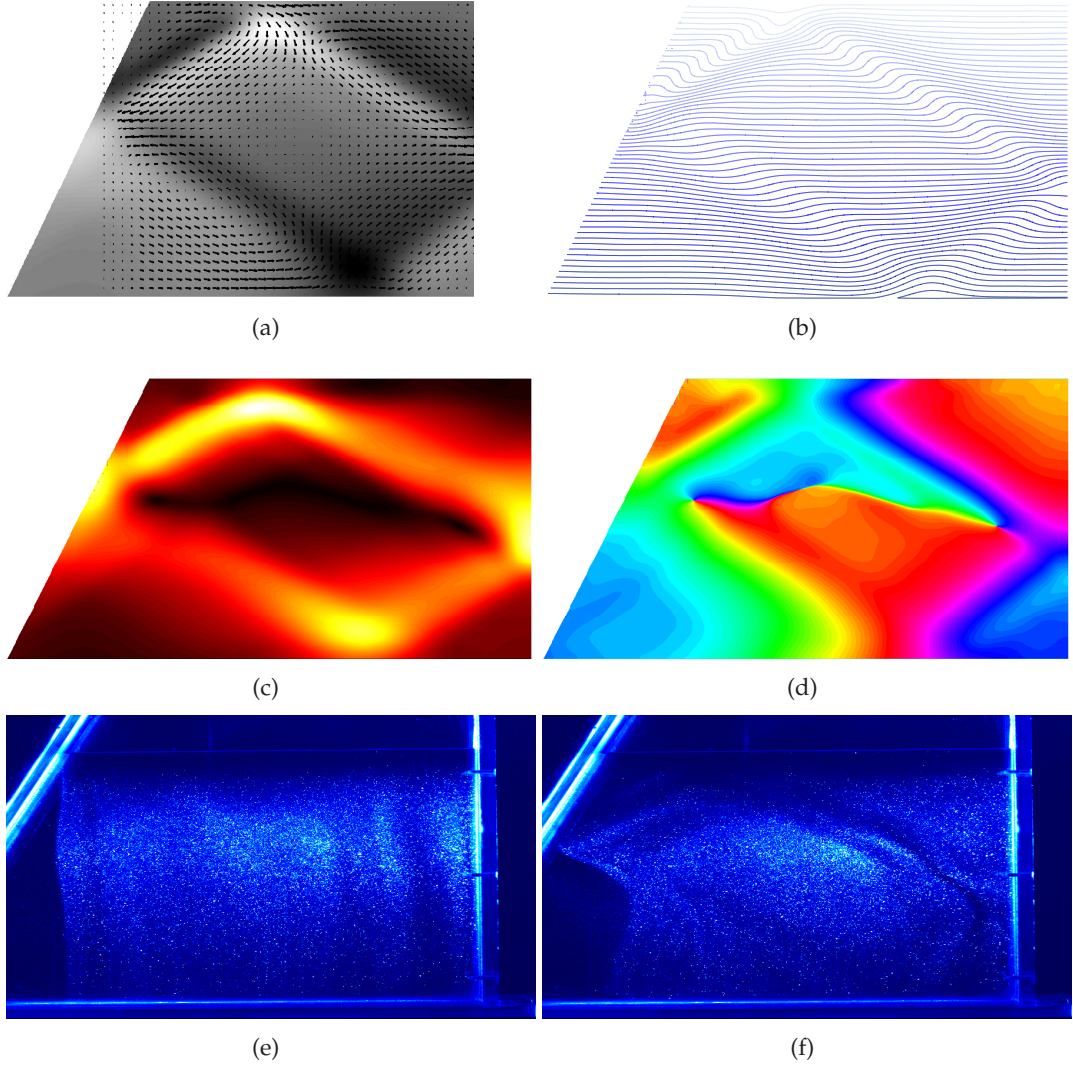
Figure 1.8: Internal wave attractors in the laboratory presented in this thesis. a) shows an example of the instantaneous density perturbation (black and white) and the velocity field (arrows) and b) the corresponding density field. c) The potential energy field being most intense (yellow/white) on the attractor and d) phase lines that align with the beams. e) and f) show particle distributions before and after an experiment, revealing transport by the attractor beams.

1.7   Transport by internal wave beams

A central question about internal waves in the ocean is whether these waves cause vertical transport of fluid and mixing. One of the major findings of this thesis is the fact that internal wave beams indeed drive a transport, also in the vertical. In chapter 7, we investigate this transport using the attractor, for this purpose regarded as four connected internal wave beams. The transport we find has two components: a relatively strong horizontal motion into the beam, about ten percent of the wave's particle excursion amplitude, and a weaker vertical component that is about one percent of the amplitude. The vertical transport is the most surprising however, as it is hindered by the stratification. The transport becomes very clear in the net displacements of the particles used to visualise the internal motions, see the distributions in figure 1.8 before and after the oscillation is turned on. The horizontal component of the transport drives particles into the beams, which results in a flow in the third direction, the direction perpendicular to the plane in which the attractor lies. In the long term the assumption of two-dimensional dynamics does not hold anymore, even in a narrow tank.

1.8   Three-dimensional internal wave attractors

Leaving the narrow tank and turning to fully three-dimensional domains, brings us new internal wave dynamics. The waves produced by an oscillating localised source in a stratified fluid for example propagate along an internal wave cone, or more precisely along two cones with their apex at the source; the three-dimensional version of the St. Andrews cross (*LeBlond and Mysak*, 1978). Interestingly, the wave field in one of the canonical papers was a cone (*Mowbray and Rarity*, 1967), but the measurements could not resolve this field since the symmetries cancelled front and back signals. Strictly speaking, ray tracing cannot be used to solve the three-dimensional wave field, but it can be used to predict wave reflection from the boundaries of a fully three-dimensional domain (*Maas*, 2005). The reflection of the waves now has to obey the restriction that the waves remain on the wave cone, set by the frequency. Furthermore the reflection depends on the three directional components of the incoming energy vector, pointing along the ray, and the local slope of the boundary. The component of the incoming rays that is in the along-slope direction is unchanged, the cross-slope component is subject to a focusing or defocusing reflection. Incorporating these rules, rays can be followed in a three-dimensional domain. In a parabolic channel, attractors were predicted by ray tracing. Numerical simulation of the same channel using the well known ocean model MICOM, showed enhanced wave motion near these regions (*Drijfhout and Maas*, 2008). In a paraboloidal domain *Maas* (2005) showed that rays could also eventually converge onto attractors, see figure 1.9. However, these considerations only follow a single ray. It turns out that following other rays, starting from the same position but in a different direction, converges onto an attractor that is not in the same plane as the other attractor. This shows that ray tracing in three dimensions is complicated, however ray tracing is useful to understand at least part of these reflections.

In chapter 8 of this thesis, we will investigate the wave field produced by an oscillating sphere in a stratified fluid contained in a paraboloidal domain. The reflections are indeed com-
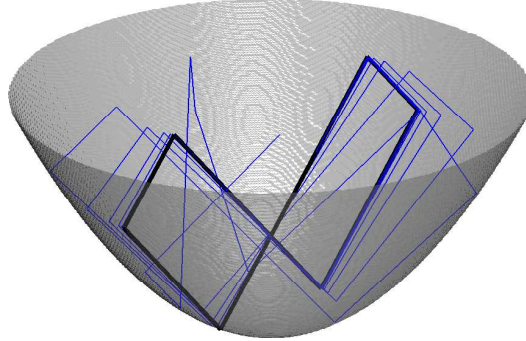
Figure 1.9: Ray tracing in a paraboloid, the blue ray converges after many reflections onto the attractor in black.
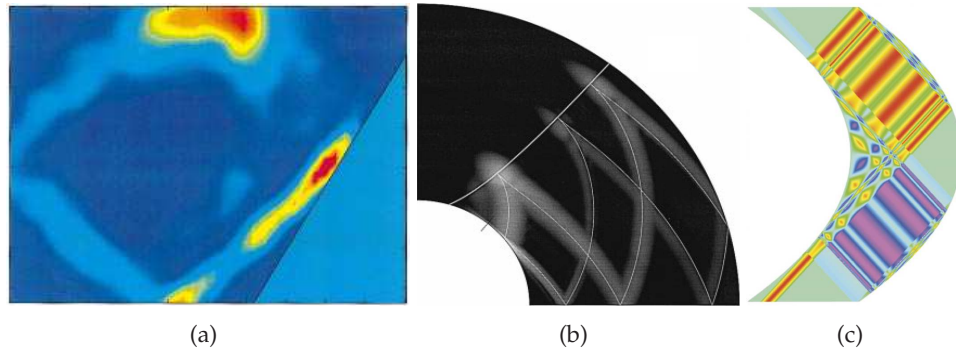
Figure 1.10: Attractors in rotating fluids. a) The attractor observed by *Maas* (2001) in a trapezoidal tank. b) Numerical simulation of a rotating, radially stratified spherical shell containing a turning surface (hyperbola) (*Dintrans et al.*, 1999). c) Streamfunction of an equatorial attractor (*Harlander and Maas*, 2007a).

plicated, but the reflection of the internal wave cone from the boundaries can be understood by tracing the first few reflections of rays. When the forcing frequency is in the internal wave attractor regime, we find that some of the energy is found in the regions of the attractors that are reached after many reflections. This observation is a strong indication of the persistence of internal wave energy to overcome dissipation.

1.9 Geophysical fluid dynamics

This thesis presents laboratory experiments in stratified fluids in a confined domain with a periodic forcing, resulting in internal wave attractors. The interest in these internal waves came from the ocean where similar waves are observed. Does that also mean that attractors can be found in the ocean? Or, more generally, are wave attractors of interest when studying fluid

(a)

(b)

(c)
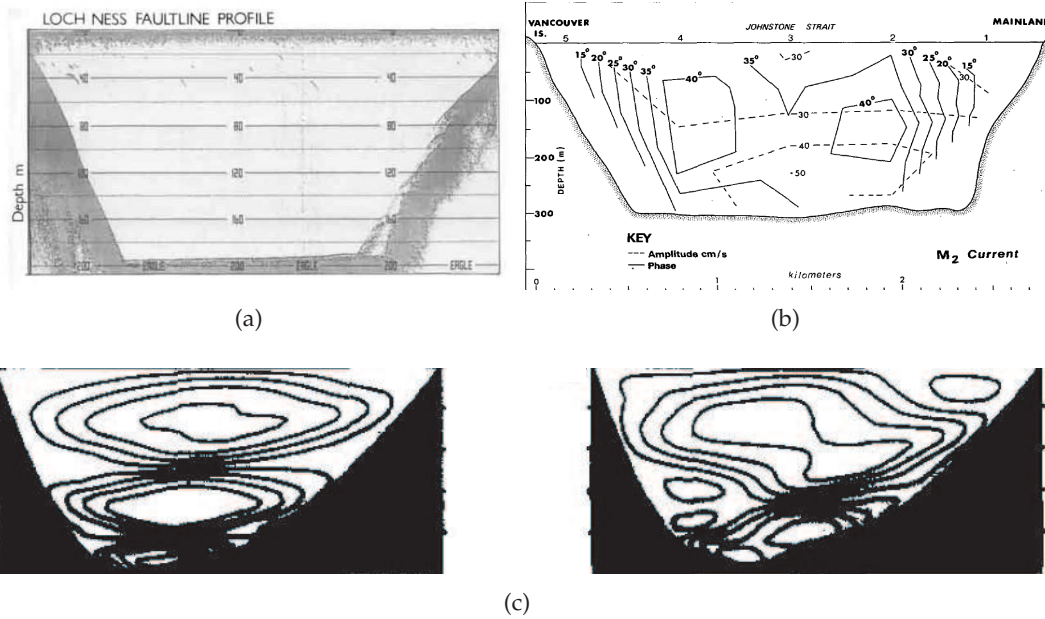
Figure 1.11: Cross-sections of deep fjords with surprisingly simple shape a) Loch Ness *Shine and Martin* (1988) and b) Johnstone Strait *Thompson and Huggett* (1980). Numerical simulation of an alpine lake showing complicated stream patterns *Münnich* (1996).

motion on a planet? In this thesis the fluid domains are very simple in shape and assuming that our tank represents an ocean or a planet would be presumptuous. Among the many things that make the ocean very different are a very complicated topography, stratification and a forcing that varies from place to place and, very importantly, the fact that it is rotating.

However, there is a remarkable similarity between stratified fluids and rotating homogeneous fluids. A rotating fluid has a 'stratification' in angular momentum, and the waves found in such fluids are called inertial waves. The dynamics of these waves is so similar, that also internal wave attractors are found for inertial waves in a homogeneous rotating fluid in an enclosed domain. In the laboratory, internal wave attractors were observed in homogeneously rotating fluids in a trapezoidal channel (*Maas*, 2001; *Manders and Maas*, 2003, 2004). Attractors were also found in the numerical simulation of a rotating fluid in a shell between two spheres (*Rieutord et al.*, 2001, 2002). Such a fluid is studied in the context of rotating astrophysical bodies with some sort of tidal forcing, for example the liquid outer core of the earth or rotating gaseous layers in stars (*Ogilvie and Lin*, 2004). Related to this is the fact that the equatorial region on a rotating stratified shell provides a natural confinement for the fluid and leads to trapping of inertia-gravity waves and the formation of attractors, see figure 1.10 (*Dintrans et al.*, 1999; *Maas and Harlander*, 2007; *Harlander and Maas*, 2007b).

So, rotation only adds to the dynamics and when we recall that the formation of attractors is a fundamental property of a forced stratified fluid in a confined domain, we cannot be certain about attractors in the ocean. Oceanographic observations are very limited and

poorly distributed over the world's oceans. Hence our spatial and temporal resolution is never enough to recover all fine scale processes in the ocean in detail. But perhaps we take the wrong starting point: there are many lakes and fjords where stratification is important, where the topography is remarkably simple and that have strong periodic motions. Examples of fjords with surprisingly simple topographies are Loch Ness and Johnstone strait, see figure 1.11 (*Thompson and Huggett*, 1980; *Shine and Martin*, 1988). In these areas observations or the numerical simulations could be done at higher resolution necessary to allow the observation of an attractor. Such a numerical simulation of an alpine lake showed velocity patterns that remind us of internal wave attractors (*Münnich*, 1996), see examples in figure 1.11c. This last observation suggests that attractor dynamics could play a role between ocean ridges as well. In such regions of very localised internal wave motion the transport by the internal wave beams (as presented in chapter 7) would be very strong.

Chapter 2

Theory

2.1 Two-dimensional internal waves

In this brief chapter, some established theory is presented that is helpful in understanding the results of the experiments in the following chapters. The concepts derived will be the Poincaré equation, the dispersion relation and an expression for the streamfunction of viscous internal wave beams.

2.2 Inviscid rotating stratified fluid

Oscillatory motions in a stratified fluid are better understood when considering the free motion of a fluid parcel. The gradually changing profile in the density of the fluid at rest is denoted by $\rho_0(z)$ in the vertical direction z, the direction that aligns with gravity g. It is assumed that the stratification is uniform in the horizontal x, y directions. When bringing a fluid parcel out of its level of neutral density the restoring forces, buoyancy and the gravity will act to bring it back. The parcel accelerates towards its original level and overshoots, and reverses to return in the opposite direction, overshoots again, resulting in an oscillation. For this oscillation a typical frequency N is found, defined by

$$N^2 = -\frac{g}{\rho_*}\frac{d\rho_0}{dz}, \tag{2.1}$$

with ρ_* the average density of the incompressible fluid. This frequency is called the buoyancy or Brunt-Väisälä frequency. It is clear that the background density gradient $d\rho_0/dz$ plays an important role in this oscillation, the stronger the stratification, the faster the oscillation as a result of the stronger forces. Similar arguments can be given for a homogeneous rotating fluid where pressure and centrifugal forces ensure that radially displaced fluid parcels are brought back to their initial position.

We continue by writing the total density of the rotating stratified fluid as

$$\rho_{tot} = \rho_*(1 - g^{-1}N^2z - g^{-1}b(x,z,t)), \tag{2.2}$$

17

where buoyancy $b = -g\rho/\rho_*$ is the induced density change by the wave motion and N is taken constant (as indeed it will be in most of this thesis).

The equations of motion are found by regarding the Boussinesq approximation of the Navier-Stokes equation in a co-rotating frame and with reduced pressure p (such that the pressure balances with both the static pressure due to the background stratification and centrifugal force) expressed per unit volume,

$$\frac{\partial \mathbf{u}}{\partial t} + \mathbf{u} \cdot \nabla \mathbf{u} + \mathbf{f} \times \mathbf{u} = -\nabla p - g\hat{z} + \nu \nabla^2 \mathbf{u}. \tag{2.3}$$

Here, t is time, $f = 2\Omega$, is twice the rotation frequency and ν is the kinematic viscosity. The laws of thermodynamics, conservation of mass and incompressibility lead to

$$\frac{\partial \rho_{tot}}{\partial t} + \mathbf{u} \cdot \nabla \rho_{tot} = 0, \tag{2.4}$$

$$\nabla \cdot \mathbf{u} = 0, \tag{2.5}$$

where we neglected molecular diffusion. When we consider the linear terms, assume no variations in the y direction and, for the moment, viscosity to be zero, we find the following equations for induced velocities (u, v, w), buoyancy and reduced pressure p:

$$
\begin{aligned}
u_t - fv &= -p_x, \\
v_t + fu &= 0, \\
w_t - b &= -p_z, \\
b_t + N^2 w &= 0, \\
u_x + w_z &= 0.
\end{aligned}
\tag{2.6}
$$

The subscripts denote derivatives. These equations thus describe a rotating linear incompressible, density stratified fluid in essentially two dimensions (horizontal x and vertical z).

We rewrite these equations by introducing streamfunction ψ such that $\mathbf{u} = (-\psi_z, \psi_x)$ and, by eliminating pressure, obtain

$$
\begin{aligned}
b_t + N^2 \psi_x &= 0, \\
\nabla^2 \psi_{tt} - b_{xt} + f^2 \psi_{zz} &= 0.
\end{aligned}
\tag{2.7}
$$

Rewriting and combining these equations leads to

$$\nabla^2 \psi_{tt} + N^2 \psi_{xx} + f^2 \psi_{zz} = 0. \tag{2.8}$$

When we assume that the streamfunction is of the form $\psi(x, z, t) = \Psi(x, z)e^{i\omega t}$ we find that internal wave motions are governed by

$$\Psi_{zz} - \Lambda^2 \Psi_{xx} = 0, \tag{2.9}$$
$$\Lambda^2 = \frac{N^2 - \omega^2}{\omega^2 - f^2}$$

a spatial wave equation. This equation is the two dimensional version of the Poincaré equation (*Cartan*, 1922). This equation, with two spatial coordinates is notoriously difficult to solve for any given domain D with boundary conditions posed at ∂D. The problem can be cast as a map of the boundary of the domain onto itself, leading to a dynamical system (*Arnold and Khesin*, 1998). Recognising the similarity with the temporal wave equation ($\psi_{tt} - c^2 \psi_{xx} = 0$ where c is the wavespeed) one can assume a partially enclosed domain, since for the temporal wave equation the future cannot be prescribed. So the classical method to solve our problem assumes the vertical direction to be limited and the horizontal to be infinite (this is quite natural to assume for an oceanographer as the ocean 'is such a pitifully thin layer', to quote H. Huppert GFD '08). Upon recognising that for constant N, (2.9) can be written as

$$(\partial_z + \Lambda \partial_x)(\partial_z - \Lambda \partial_x)\Psi = 0, \tag{2.10}$$

solutions can be found along characteristic lines $c_{\pm} = x \pm \Lambda z$ (*Magaard*, 1962, 1968; *Baines*, 1973, 1974). The slope of these characteristics is thus defined solely by the forcing frequency, rotation and buoyancy frequency. The solutions along the characteristics are reminiscent of the ray tracing in the previous chapter, where the angle with the vertical is thus determined by Λ.

However, a fluid is never unbounded, see chapter 1, so we turn again to an enclosed domain. *Maas and Lam* (1995) derived a solution for Ψ in a parabolic domain. Only prescribing that $\Psi = 0$ at the boundary leaves the problem underdetermined. Prescribing also the normal derivatives at the boundary however, renders the problem ill-posed (*Rieutord et al.*, 2000). So the solution was found by restricting the prescription of the boundary conditions to so-called fundamental intervals (*Maas and Lam*, 1995). These intervals are the regions that are connected to the rest of the fluid through the webs spanned by the characteristics. An inviscid solution for the parabolic domain featured fine structures that implied strong and complex shear motion on the attractor. For a special case in the trapezoidal domain an analytic solution (*Maas*, 2009) was found having the same fine structure and featuring a self-similar spectrum. This complex structure of the solution changed appearance when a more realistic sloshing type of forcing was assumed (*Lam and Maas*, 2008). Then the motion was confined to a region around the attractor and lacked the self similar fine structure.

The very nature of the attractor is a singularity where the velocities blow up. For this reason numerical studies that solve the Poincaré equation in two-dimensional enclosed domains, introduce viscosity to keep the related fields bounded. As mentioned in the previous chapter, attractors were found for rotating shells (*Rieutord et al.*, 2001, 2002) and in tilted squares with density stratified fluids *Ogilvie* (2005); *Swart et al.* (2007).

2.3   Dispersion relation

As the Poincaré equation is difficult to solve in a bounded domain we might consider an unbounded, and therefore unrealistic, fluid domain. If we assume that $\Psi = \hat{\Psi} \exp[-i(k_x x + k_z z)]$, we find the dispersion relation

$$\omega^2 = \frac{1}{k_x^2 + k_x^2}(N^2 k_x^2 + f^2 k_z^2) = N^2 \cos^2 \theta + f^2 \sin^2 \theta. \tag{2.11}$$

This θ is the angle we have seen before in the experiments of chapter 1 and was the starting point for our ray tracing. Indeed $\tan^2 \theta = \Lambda^2$, so that for fixed N and f an increase in ω results in a smaller θ, i.e. steeper rays. Quite unusually this dispersion relation does not relate the frequency to a single wavenumber, but to all wavenumbers that obey $k_x/k_z = \pm 1/\tan(\theta)$. In any realistic fluid the existence of all wave lengths is not possible. Viscous effects play a role in dissipating the small scale waves much faster than the large scale waves, so that only a selection of waves is found to exist in the entire wavenumber spectrum.

2.4   Non-rotating, viscous internal wave beams

The regularising effect of viscosity on the wavenumber spectrum is considered next and in later chapters we will see how viscous damping controls the shape of the attractors that we observe in the laboratory. We will derive an expression for the streamfunction of a viscous beam in a non-rotating ($f = 0$), density stratified fluid (*Thomas and Stevenson*, 1972; *Tabaei and Akylas*, 2003; *Voisin*, 2003). For simplicity we choose $N = 1$ so that the dispersion relation becomes $\omega = \cos \theta$. The governing equations are

$$\begin{aligned}
u_t + p_x &= \nu \nabla^2 u, \\
w_t + p_z - b &= \nu \nabla^2 w, \\
b_t + w &= 0, \\
u_x + w_z &= 0.
\end{aligned} \tag{2.12}$$

The equations are readily rendered in terms of the streamfunction and buoyancy,

$$\begin{aligned}
b_t + \psi_x &= 0 \\
\nabla^2 \psi_t - b_x - \nu \nabla^4 \psi &= 0.
\end{aligned} \tag{2.13}$$

The dispersion relation predicts that, from a localised source, wave beams radiate out in four directions under angle θ with the vertical. We will now zoom in on one beam coming from this source. To do so we introduce a tilted coordinate system aligning with a beam propagating into the positive x, z-quadrant under angle θ with the vertical:

$$\xi = x \sin \theta + z \cos \theta, \tag{2.14}$$

$$\eta = -x \cos \theta + z \sin \theta. \tag{2.15}$$

Rewriting (2.13) then leads to

$$b_t + \sin\theta\psi_\xi - \cos\theta\psi_\eta = 0$$
$$\nabla^2\psi_t - \sin\theta b_\xi + \cos\theta b_\eta - \nu\nabla^4\psi = 0, \tag{2.16}$$

We further assume

$$\psi = [\Psi_1 + \epsilon\Psi_2 + ...]e^{i\omega t} + c.c., \qquad b = [R_1 + \epsilon R_2 + ...]e^{i\omega t} + c.c.$$

and, as the beam is dominated by motions in the narrow cross beam direction and we assumed that viscosity controls the width of the beam, we define

$$\nu = 2\epsilon, \xi = \frac{\sin\theta}{\epsilon}\chi, \tag{2.17}$$

the factors 2 and $\sin\theta$ are for analytical convenience. We order the linearised equations (2.16) in terms of ϵ and find

$$\frac{\partial\Psi_1}{\partial\eta} = iR_1,$$
$$\omega\frac{\partial\Psi_2}{\partial\eta} - i\omega R_2 = \frac{\partial\Psi_1}{\partial\chi}, \tag{2.18}$$
$$i\omega\frac{\partial^2\Psi_2}{\partial\eta^2} + \omega\frac{\partial R_2}{\partial\eta} = 2\frac{\partial^4\Psi_1}{\partial\eta^4} + \frac{\partial R_1}{\partial\chi},$$

where dispersion relation $\omega = \cos\theta$ is used. We have now found three equations for the three unknowns Ψ_1, R_1 and $\frac{\partial\Psi_2}{\partial\eta} - iR_2$. Note that we have no set of equations to solve for R_2 and Ψ_2 independently. Combining the above equations we find

$$\frac{\partial^4\Psi_1}{\partial\eta^4} = i\frac{\partial^2\Psi_1}{\partial\eta\partial\chi},$$

or

$$\frac{\partial^3\Psi_1}{\partial\eta^3} = i\frac{\partial\Psi_1}{\partial\chi} \quad (+g(\chi)). \tag{2.19}$$

Note that R_1 satisfies (2.19) with $g(\chi) = 0$. However, as R_1 is a derivative of Ψ_1, we will focus on the latter. We proceed by setting $g = 0$ and make the Ansatz that $\Psi_1 = F(\eta)G(\chi)$

$$\frac{F_{\eta\eta\eta}}{F} = i\frac{G_\chi}{G} \equiv -ik^3,$$

where k^3 is a separation constant. For a more rigourous derivation see *Moore and Saffman* (1969); *Voisin* (2003). Although k is still a general constant, it will become clear that it is a wavenumber. Then the general solution follows by the linear superposition of solutions $e^{-k^3\chi+ik\eta}$:

$$\Psi_1 = \int_{-\infty}^{\infty} A(k)e^{-k^3\chi+ik\eta}dk. \tag{2.20}$$

Because of our specific choice of the coordinate system, we are considering an internal wave beam with energy propagation in the positive χ-direction. This means that we need to choose $A(k < 0) = 0$, as phase should be propagating in the negative η-direction. As the precise shape of the source at $\xi = 0$ is unknown, commonly $A(k > 0) = a = 1$ is chosen. This corresponds to a delta function source in real space. Note that the freedom to choose a, or better $A(k > 0)$, allows us to match the theoretical velocities better with the observations. So we find

$$\psi(\chi, \eta, t) = Re(\Psi_1 e^{i\omega t}) = \int_0^{\infty} e^{-k^3\chi} \cos(k\eta + \omega t)dk. \tag{2.21}$$

The integral expression shows that, from forcing at $(\chi, \eta) = (0, 0)$ at frequency ω, a whole spectrum of waves at different wave lengths $\lambda = 2\pi/k$ arises. Wavenumber k is now measured along η and $k \equiv \sqrt{k_x^2 + k_z^2}$ from the previous section. The energy travels along the beam in the positive χ direction and phase changes in the η direction. The solution for the streamfunction, gives us the velocity fields by definition. We plot the fields rotated back to the x, z-plane, and see that the beam structure resembles that observed coming from a cylinder. Plotting the velocity arrow at any given time (figure 2.1), we note that the motion is along the beam and in opposite direction on either side of it and decaying along it. This figure is identical to figure 1.4. The complex velocity field can also be shown in terms of amplitude and phase. This shows nicely the decay of the energy and the shearing nature of the motion in the phase field. The phase lines in the middle of the beam (where the amplitude is maximal) show straight lines of constant phase.

Viscous dissipation attenuates the wavenumber spectrum in the ξ direction and dissipates the high wavenumbers, small wave lengths, much more. This means that the spectrum has a peak that shifts to the low wavenumber side of the spectrum for increasing ξ. This shift appears in real space as a broadening of the beams in the η direction. The spectrum is self-similar, that is, the qualitative shape of the spectrum does not change, only the value of k at which the spectral peak is found changes and the quantitative value of the integral (total energy), see spectra in figure 2.1d. This shift of the peak in the wavenumber spectrum due to viscous attenuation of the beam is also found in the attractor beams. This is the topic of the next chapter. In chapter 7 we will use the viscous streamfunction again to explain the observed Stokes drift on the attractor beams.

(a) (b) (c)

(d)

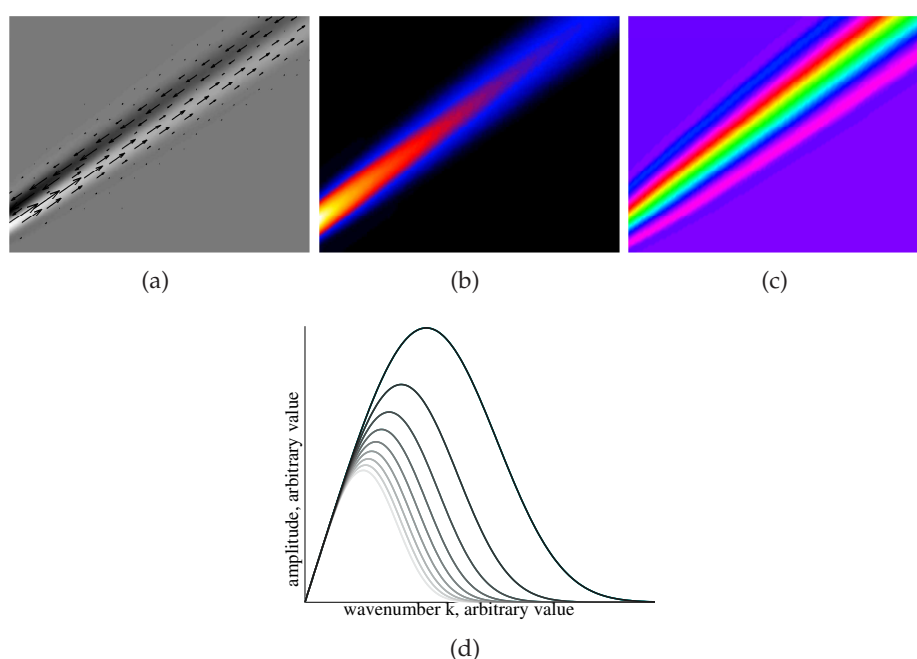Figure 2.1: Internal wave beam as described by (2.21). a) Velocity arrows and comparison with beam structure as in figure 1.3, b) energy and c) phase of wave. d) Wavenumber spectrum of the same beam for increasing χ, with decreasing value at which wavenumber the peak is found. As the spectrum is self similar the values are arbitrary.

Chapter 3

The wave number spectrum and evolution of an internal wave attractor

3.1   Introduction

Understanding the behaviour of linear internal waves in bounded geometries has relevance to oceanography, astrophysics and fluid dynamics in general. The dispersion relation describing the internal waves, $\omega = N\cos\theta$, relates the frequency ω of the internal waves to the buoyancy frequency N. The wave energy propagates with angle θ with the vertical, with the vertical opposite to the gravitational direction. However, unlike the more familiar surface waves, the dispersion relation does not restrict the wave vector $\mathbf{k} = k(\cos\theta, \sin\theta)$ other than being perpendicular to the group velocity (*Phillips*, 1977; *LeBlond and Mysak*, 1978; *Maas*, 2005). The dispersion relation predicts that reflection of the internal waves at boundaries that are neither horizontal nor vertical, leads to a focusing or defocusing of the waves. *Maas and Lam* (1995) showed that in almost all confined fluid domains wave energy focusing dominates defocusing, leading to a so called wave attractor. The experimental confirmation of such an attractor in a trapezoidal domain was presented in *Maas et al.* (1997) and re-analysed by *Lam and Maas* (2008). In this experiment a nearly two-dimensional container, filled with a linearly stratified fluid, was vertically oscillated. Displacement of dye lines was used to visualise the internal dynamics. Starting from a rest position, an attractor grew due to subharmonic parametric instability. This instability is a linear mechanism that leads to the growth of a perturbation with half the forcing frequency as a result of the modulation of the gravitational acceleration (*Benielli and Sommeria*, 1998). *Lam and Maas* (2008) revealed that the amplitude of the isopycnal displacements on the attractor had an exponential growth before reaching saturation. Contrary to the growth of a regular mode, the saturation time varied from position to position. They also proposed a causal connection between forcing of a surface seiche and the internal wave field.

Wave attractors are also found for the analogous class of inertial waves supported by homogeneous rotating fluids (*Stewartson*, 1971; *Maas*, 2005). Experimentally, inertial wave attractors have been observed and studied by *Maas* (2001) and *Manders and Maas* (2003). They considered a rotating rectangular tank with a sloping wall. From the comparison between the small tank of *Maas* (2001) and the larger tanks of *Manders and Maas* (2003), it appears that the width of the attractor branches is independent of viscosity. This led *Manders and Maas* (2004) to the conclusion that the spatial scale of the observed attractors is set by non-linear processes. However, in the theoretical work by *Rieutord et al.* (2001) and *Rieutord et al.* (2002) viscous processes were assumed to set the scale. Also *Ogilvie* (2005) considered the low-viscosity limit and provided a way of calculating the dissipation rate. In these models the dissipative spreading of the waves balances the geometric focusing due to reflections.

The purpose of this chapter is to contribute to the above discussion of what sets the attractor scale. In this context, we define the scale of the attractor as the dominant wavelength, perpendicular to the attractor branches, corresponding to the peak in the wavenumber spectrum (to be discussed later). We have conducted experiments and present the observed data mainly as spectra of the wavenumber k. We show that a balance exists between amplification by focusing at the sloping wall and dissipation at the highest wavenumbers.

3.2 Method

For the experiment we use a narrow rectangular tank with one sloping end wall at an angle of $27°$ to the vertical (see Figure 3.1). Although the tank has finite width, we refer to it as nearly two-dimensional. This is because the symmetry is broken by the slope so the wave motion will primarily depend on the along-tank and vertical coordinates, x and z respectively, and will be essentially uniform in the narrow, cross-tank (y) direction. See Table 3.1 for the dimensions of the tank. The tank is filled with a fluid with a stratification comprising a layer of depth $H = 190 \pm 2$mm, in which the density decreases linearly upwards, beneath a shallow mixed surface layer. The presence of this mixed layer does not affect the dynamics of the stratified layer and so we shall exclude it from our discussion. Filling the tank with the well known double bucket technique is not possible as the domain has a cross section that varies with height. Instead, we use two computer controlled Masterflex peristaltic pumps that enable us to fill the tank with any desired stratification. We present the findings of experiments performed in a fluid with constant buoyancy frequency $N = \sqrt{-g/\rho_* \, d\rho_0(z)/dz} = (3 \pm 0.1) \ \text{s}^{-1}$, where ρ_* is a reference density. Here, we measure the background stratification $\rho_0(z)$ by taking 10 density samples. Although our choice of N pushes the limit of the Boussinesq approximation, using smaller values of N is found to make no difference other than that it affects the quality of the visualisation.

To measure the motions in the fluid non-intrusively, we use the synthetic schlieren technique (*Dalziel et al.*, 2000). Synthetic schlieren measures the refractive index changes of a fluid resulting from density perturbations. The principle is as follows. When a light-ray propagates through the fluid, the direction of propagation of this ray will be altered by the local value of the gradient of the index of refraction. A random dot pattern on a light bank 0.5 m behind the tank and fixed in the laboratory frame is monitored through the fluid. Density perturbations alter the refractive index and hence the direction of the light and are observed as apparent movement of the dots. Unfortunately, the refractive index of the air, between the tank and the point of observation, is also altered by unavoidable temperature fluctuations in the laboratory. This leads to some 'thermal noise' contaminating the observations. To record the apparent movements of the dots, we use a Jai CV-M4+CL camera (1.3 MPixel monochrome) positioned 8 m from the tank. Using an unperturbed reference image, the perturbed position of the dots is translated into corresponding density gradient variations. For this comparison and data processing we use the DigiFlow software. As we observe the changes in the density gradient field, the stronger the undisturbed gradient field is, the more the dots appear to move. Consequently, we present results of experiments with large N. We will present the observations as components of normalised buoyancy gradient $\mathbf{b} = (b_x, b_z) \equiv \nabla\rho/(d\rho_0/dz)$, i.e. the perturbation density gradient relative to the gradient of the unperturbed background stratification, $(d\rho_0/dz)$.

Initially, we focused on internal wave generation by subharmonic parametric instability. This sort of forcing resulted in the attractor reported by *Maas et al.* (1997) and *Lam and Maas* (2008). To excite the instability, we use a vertically oscillating platform that carries the tank. However, with forcing amplitude A_e well below the theoretically predicted threshold of the parametric instability, another generation mechanism is already very effective. Owing to slight horizontal movements coming with the much stronger vertical motion, the stratified fluid in

Parameters experiment			
Forcing period	T	5.1	s
Buoyancy frequency	N	3	s^{-1}
Fluid height	H	190	mm
Dimensions tank	$h \times w \times L_{bot}$	$330 \times 101 \times 453$	mm
Angle sloping wall	α	0.47	rad
Forcing frequency	ω_e	$2\pi/T = 1.23$	s^{-1}
Forcing amplitude	A_e	120	mm
Duration forced stage		$50 \times T = 255$	s
Duration decay stage		$40 \times T = 204$	s

Table 3.1: Parameter values of the experiment, described in Section 2.

the tank starts sloshing a little, with an estimated amplitude of 0.5 mm. This barotropic motion is strong enough to generate baroclinic internal waves from its interaction with the slope. (Installing a rigid lid on the surface prevented this sloshing and effectively removed any measurable internal wave generation). The generated internal waves have a frequency ω equal to that of the excitation, i.e. $\omega = \omega_e$. The results presented in this paper are on internal waves that are generated by this barotropic motion of the fluid.

The experiment is performed as follows. After 1 period, $T = 2\pi/\omega_e$, of linearly increasing the amplitude to A_e, the platform is vertically oscillated with frequency ω_e for 49T. During this stage the camera is triggered to capture images at three fixed positions at each cycle of the oscillation. At $t = 50T$ the motion of the platform is linearly damped in two periods. Directly after the platform is at rest, from $t = 52T$ on, the camera captures 24 frames s^{-1} (fps) of the decay stage, over 40 periods.

3.3   Results

We observe an internal wave attractor with the parameters given in Table 3.1. We present the result of harmonic analysis at frequency $\omega = \omega_e$ of b_x and b_z using the very accurate time series (24 fps) between $t = 52T$ and $t = 54T$. The sloshing of the free surface does not show up in harmonic analysis. The amplitudes are shown in Figure 3.1a and b; the figures have been cropped to the boundaries of the tank and to the bottom of the mixed surface layer. The orthogonal sections over the four attractor branches, represented by the white dashed lines in Figure 3.1a, are for later use and will be referred to as S1-S4. The corresponding phases of the internal wave fields are shown in Figure 3.1c and d. The angles of the sloping wall, α, and of the internal waves, θ, are indicated in Figure 3.1c. Note that the phase of b_x is inverted upon each reflection, while that of b_z is maintained.
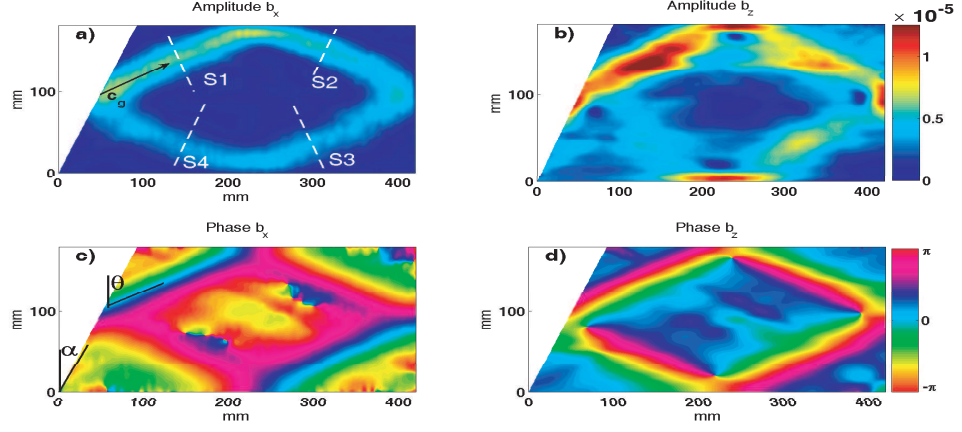
Figure 3.1: Harmonic analysis of the observations on b_x (left) and b_z (right), a) and b) show the amplitude. The black arrow in a) gives the direction of the group velocity vector $\mathbf{c_g}$ pointing in the direction of energy propagation. The white lines indicate sections S1-S4, perpendicular to the corresponding four branches of the attractor. The phase is shown in c) and d). Slope angle α and propagation angle θ are indicated in c).
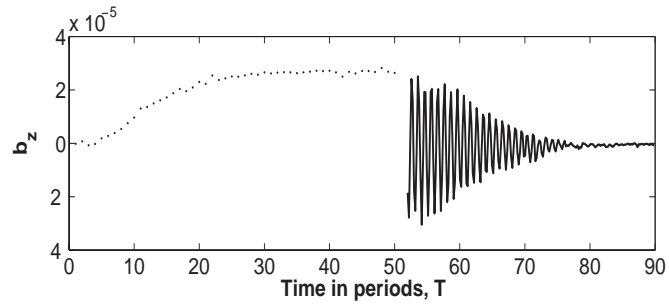
Figure 3.2: Observed growth and decay of b_z in the middle of S1. Note that the observation in the forced stage is once per period while the decay is shown in much more detail (125 obs/T).
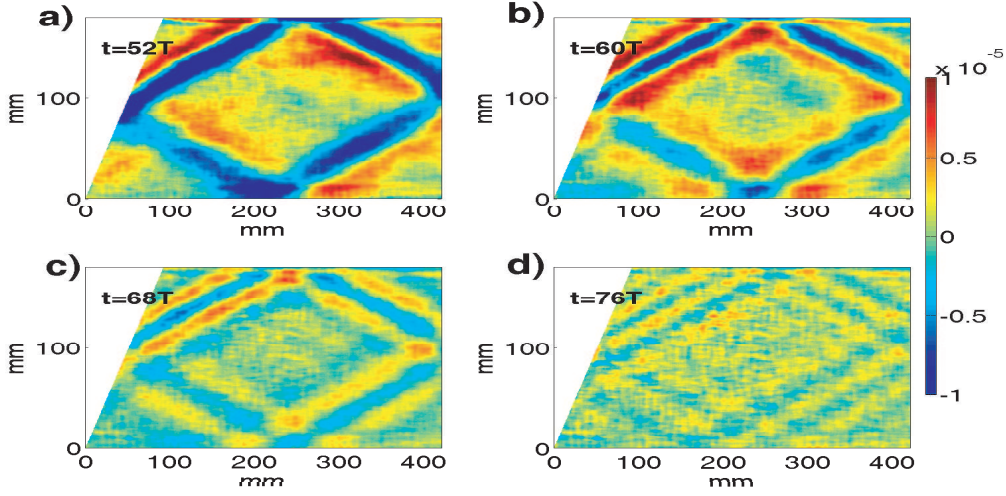
Figure 3.3: Four snapshots b_z, at a) $t = 52T$ (beginning of decay stage), b) $t = 60T$, c) $t = 68T$ and d) $t = 76T$, showing that the shorter wavelengths decay later.

The spatial structure of the perturbation and phase take the form of an internal wave attractor, as originally observed by *Maas et al.* (1997). The sloping wall focuses waves propagating in a clockwise sense. The phase propagation is perpendicular to the attractor branches, indicating that the group velocity, and thus the energy, propagates clockwise, as indicated by the black arrow. Following the energy from the sloping wall along the attractor, it is clear that the intensity of the density perturbation decreases, reaching a minimum just before the sloping wall. Also, the intensification at the reflection points is observed, being the result from (linear) superposition of the incident and reflected branches.

After starting the oscillating platform, the attractor grows from the initial undisturbed state. The growth of b_z in the middle of S1 is shown in Figure 3.2. There is clearly an initial growth stage reaching an equilibrium after $t = 25T$. Throughout the decay stage ($t > 52T$) the frequency of the attractor remains well preserved with $\omega = \omega_e \pm 0.05\,\mathrm{s}^{-1}$. The dispersion relation therefore ensures that θ is preserved, as can be seen in Figure 3.3 where four snapshots of the decay stage are presented. Rather surprisingly, these snapshots suggest that the wave length of the attractor decreases. This seem contrary to the notion that diffusive processes eliminate the short wavelengths. The snapshots confirm that the magnitude of the perturbation decays everywhere in the tank, similar to the observation in Figure 3.2.

3.3.1   Spectral analysis

The remarkable presence of several wave lengths during the decay suggests value in analysing the wavenumber spectrum. We introduce a coordinate system that aligns with the branches and the wave vector $\mathbf{k} = k(\cos\theta, \sin\theta)$ in the x, z-plane. In particular, η is the coordinate along section S1, increasing from top left to bottom right, and is given by $\eta = x\cos\theta - z\sin\theta$. The
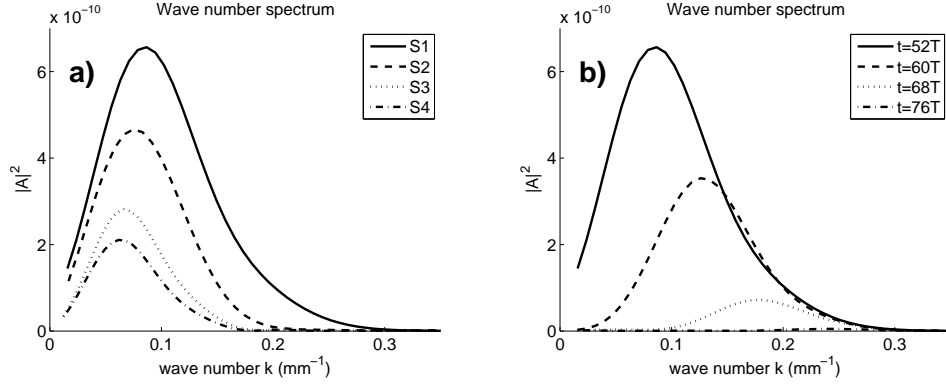
Figure 3.4: a) Viscous broadening from S1 to S4 at t=52T. b) Time evolution of the spectrum along S1 at $t = 52T, 60T, 68T$ and $70T$.

buoyancy gradient in the direction of η is $b_\eta = b_x \cos\theta - b_z \sin\theta$, and we assume that this can be written as

$$b_\eta = \int A(k)e^{i(k\eta - \omega t)}dk. \tag{3.1}$$

Note that η is redefined along S2-S4. Ideally, the complex amplitudes $A(k)$ are obtained by Fourier transform of b_η, where the amplitude fields of harmonic analysis are used to construct b_η (fields such as in Figure 3.1). However, harmonic analysis is only possible in the decay stage as the few observations in the forced stage, i.e. three per cycle, prove to be insufficient to adequately reproduce the amplitudes. Instead, for $t < 50T$, we must approximate $A(k)$ using a Fourier transform of the b_η field from the instantaneous gradient fields. Examining this approximation for $t \geq 52T$ shows that it reproduces the main qualitative features of the full spectrum. As is standard when performing Fourier analysis on non-periodic signals, we add to every section a sequence of zeros, so called zero-padding. This allows us to plot nearly continuous spectral lines (and contour plots) in Figures 3.4-3.6.

The spectra of S1-S4 from harmonic analysis, over the first period of the decay, are presented in Figure 3.4a. Comparing the spectra, we see a clear shift of the spectral peak towards low wavenumbers as we move from S1 to S4. This can also be seen in Figure 3.3a, at $t = 52T$, with a broadening of the branches going from S1 and S4. From the spectra we learn that, while following their path around the attractor, the high wavenumbers disappear and the low wavenumbers remain. This viscous broadening of the attractor branches corresponds with the decrease in dominant wavenumber.

However, as the attractor decays we observe that the low wave numbers (large wave lengths) disappear. The spectra for S1 from harmonic analysis around the same moments during the decay as in Figure 3.3 are shown in Figure 3.4b. Indeed, apart from a decrease of total amplitude, we here see a clear shift of the peak towards the high wavenumbers

Approximate spectra for S1 from instantaneous fields during growth, equilibrium and decay stages are combined in Figure 3.5. It shows in false colour the 'energy' $|A(k)|^2$ (i.e. the
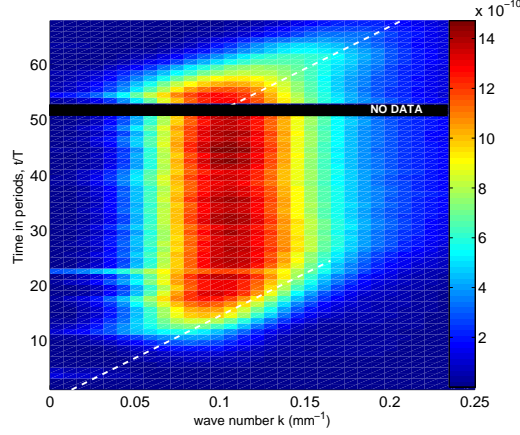
Figure 3.5: Evolution of the wavenumber spectrum along section S1 during the whole experiment. The dashed white lines indicate t_{sum}. The black band ($50 \leq t/T \leq 52$) indicates the transition from the forced stage to the decay stage.

square of the spectral amplitude of the buoyancy gradient) as a function of wavenumber (horizontal axis) and time (vertical axis). At the start of the experiment, $t = 0$, there are no waves. The spectrum grows from the lowest wave numbers towards the high wavenumbers. Thermal fluctuations in the laboratory contaminate the spectra, most notably at $t = 22T$ and $t = 42T$. By $t = 25T$ the spectrum reaches equilibrium, coinciding with the saturation of the amplitude of the density gradient perturbation in Figure 3.2. After the oscillation of the platform is stopped, $t > 52T$, we observe the decay of the spectrum. It is clear that, as time passes, the energy at low k values decays fastest, while that at high wavenumbers persists. This is in accordance with the qualitative observation of the structure in Figure 3.3. It is worth noting that high wavenumber energy exists from the time the spectrum reaches equilibrium onwards. However, the energy at high wavenumbers is overshadowed by that of the stronger low wavenumbers until the forcing is halted. Only when the high wavenumbers become dominant do they determine the scale of the attractor branch.

3.4   Simple models

In this section we present a model explaining the observed characteristics of the wavenumber spectrum in the growth and decay stage. Subsequently, the equilibrium spectrum will be addressed.

During the growth and equilibrium stages of the experiment the largest waves are driven by sloshing of the fluid in the tank. Propagation of the waves inevitably leads to reflection at the walls. Every time these waves reflect at the sloping wall in a clockwise (focusing) sense, their wavenumber increases (wave length decreases) by a factor

$$\gamma = \frac{\sin(\theta + \alpha)}{\sin(\theta - \alpha)}. \tag{3.2}$$

For the parameters given in Table 3.1 this yields focusing power $\gamma \approx 1.6$. The amplitude of the wave is amplified by the same ratio, as conservation laws demand. This results in a continuous transfer of energy towards the high wave numbers. This transfer is also dependent on group speed $c_g(k) = |\mathbf{c}_g| = N\sin\theta/k$, which decreases with increasing k. We define the different loop times, the time needed for the energy in wavenumber k to travel once around the attractor of length L_a:

$$t_{loop}(k) = \frac{L_a}{c_g(k)} = \frac{L_a k}{N\sin\theta}. \tag{3.3}$$

We also define a sequence of focused wavenumbers

$$k_n = \gamma k_{n-1} = \gamma^n k_0, \tag{3.4}$$

with $k_0 = 2\pi/H$, the wavenumber corresponding to the scale of the basin and n the number of loops around the attractor. Combining (3.3) and (3.4) we define

$$t_{sum}(k_n) = \sum_{i=0}^{n-1} t_{loop}(k_i) = \sum_{i=0}^{n-1} \frac{L_a \gamma^i k_0}{N\sin\theta} = \frac{L_a k_0}{N\sin\theta} \frac{\gamma^n - 1}{\gamma - 1}. \tag{3.5}$$

This is the time passed since the wave had wavenumber k_0. The increase in wavenumber and amplitude is not unlimited. Viscosity acts on the waves and becomes more efficient at dissipating energy at high wavenumbers. This process is the sink for the energy put into the system. A balance between generation/amplification and dissipation is reached in the equilibrium stage; this is addressed in the next section. When we stop the oscillation, and thus the energy input, the transfer of energy towards high k continues. The source for the lowest wavenumber (k_0) however, is now gone.

This ongoing transfer from low to high wavenumbers is seen in Figure 3.5. Here, we see that in the decay stage, the energy associated with the high values of k is sustained much longer at the equilibrium level than is the case at the low wavenumbers. The dashed white lines in Figure 3.5 represent t_{sum}, with $L_a = 850$ mm, starting from arbitrary times. We can see that these lines align with the peak shift in the spectrum in both growth and decay stage.

3.4.1 Simple model equilibrium spectrum

We now address the observed equilibrium spectrum. A balance is assumed between amplification of the amplitude through reflection off the slope and dissipation at the high wavenumbers. *Rieutord et al.* (2001) considered a travelling wave packet along an attractor and described its damping by viscosity as

$$A(k) = A_0 e^{-\nu k^2 t}. \tag{3.6}$$

This follows by inserting (3.1) into a diffusion equation $\partial b_\eta / \partial t = \nu \partial^2 b_\eta / \partial \eta^2$. The viscous damping is of influence over multiple wave periods, $t \gg T$, and we will model damping
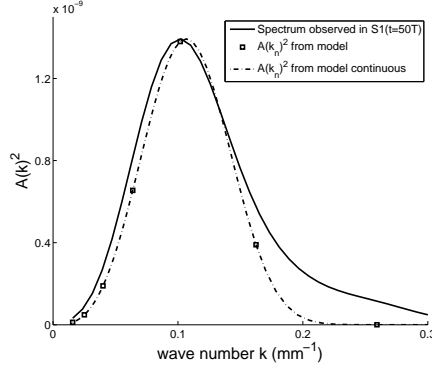
Figure 3.6: Comparison of the observed equilibrium spectrum and A_n^2 from (3.7)

between successive reflections from the slope for a given packet discretely. We do this by sampling (3.6) at each loop around the attractor. At the sloping wall the wave (k_{n-1}) is focused into a wave with higher wavenumber k_n. Upon reflection the energy flux is preserved, i.e. $F = c_g U^2/2$ is constant, where the particle motion U scales with the perturbation density (*Phillips*, 1977). However, since A refers to the amplitude of the perturbation density gradient, then $U \propto A/k$ implying $A^2 k^{-3}$ is preserved. From this we find the recursive relation $A(k_n)^2 \equiv A_n^2 = \gamma^3 A_{n-1}^2$. Combining this description of focusing with that of the dissipation in (3.6) and the time for each loop, (3.3), then leads to

$$A_n^2 = \gamma^3 \exp\left[\frac{-2\nu L_a k_n^3}{N \sin\theta}\right] A_{n-1}^2 = \gamma^{3n} \exp\left[-\Upsilon(\gamma^{3n} - 1)\right] A_0^2, \tag{3.7}$$

with $\Upsilon = [2\nu/(H^2 N)][L_a/H][(2\pi)^3/((\gamma^3 - 1)\sin\theta)]$. We calculate subsequent wave numbers, starting from k_0 and using appropriate values for our experiment ($\nu = 1$ mm^2/s and $\omega = 1.23$ s^{-1}). We find that in eight focusing reflections the largest wave length is transformed into the smallest wave length found in our observed spectrum. In Figure 3.6 we plot the observed equilibrium spectrum along S1 (solid line) and our computed A_n^2 from (3.7) (squares). The dashed line indicates the spectrum where n is treated as a continuous variable. It is clear that for the lowest wavenumbers the amplification by focusing is dominant (left side of the spectrum $\propto \gamma^{3n}$) and that dissipation mainly acts on the high wavenumbers (right side of the spectrum $\propto \exp\left[-\Upsilon(\gamma^{3n} - 1)\right]$). The observed and modelled spectra have similar behaviour and indeed show that our assumption of a balance between focusing and viscous dissipation is reasonable. We argue that the difference between observation and model on the dissipation side of the spectrum is caused by noise. Note that (3.7) fixes the structure of the spectrum but not its scale. The amplitude A_0 remains arbitrary and we have matched it to that of our experimental spectrum. While we do not know the actual A_0 for our experiments, we expect that the amplitude of the forcing will play a dominant role in determining A_0 and hence the maximum value of $A(k)$.

3.5 Discussion and conclusion

From this work it is clear that the observed structure of internal wave attractors can be explained through the linear processes of focusing and viscous diffusion. Focusing takes the energy from the relatively large basin scale, that is most strongly excited by the forcing, to smaller scales where viscous dissipation dominates, overwhelming any further focusing. In these experiments the internal waves at the basin scale were undoubtedly linear. Whilst the wave amplitude increased as the wave length decreased during the first few cycles of the attractor, this was not sufficient to generate any strong nonlinearities.

In their laboratory experiments, *Manders and Maas* (2004) observed that the attractor scaled with the tank size. From this they concluded that the scale of the attractor is independent of viscosity. Paradoxically, in the astrophysical context, *Rieutord et al.* (2001) and *Ogilvie* (2005) found that the scale of the attractor depends on viscosity. We find that the scale of the attractor is set by the spectral peak at wavenumber $k_{peak} = \gamma^{n_{peak}} k_0$. Neglecting the discrete nature of n, the value of n_{peak} is obtained when the derivative of (3.7), with respect to n vanishes, giving $n_{peak} = -\ln(\Upsilon^{1/3})/\ln(\gamma)$. Recalling that $k_0 \propto H^{-1}$, assuming that $L_a \propto H$ and using the relation $p^{\ln q/\ln p} = q$, shows that the length scale of the attractor is $k_{peak}^{-1} \propto (H\nu/N)^{1/3}$. The value of k_{peak} turns out to be strongly dependent on fluid height H when the laboratory range is considered ($200 < H < 1000$ mm, *Manders and Maas* (2004)). However, this does not mean that k_{peak} is independent of the viscosity in this geometry regime. Even at astrophysical scales, the balance between geometry, viscosity and stratification will set the scale of the attractor.

Chapter 4

Equilibrium spectrum for internal wave attractor in a trapezoidal basin

4.1   Introduction

The focusing of internal gravity waves through their reflection from sloping boundaries has far-reaching consequences for mixing in density stratified fluids. While the frequency of such reflections is preserved, simple geometric arguments dictate that the wave number cannot be preserved, except in the special cases of horizontal or vertical boundaries. This is a direct consequence of the dispersion relation,

$$\omega = N \cos \theta, \tag{4.1}$$

where ω is the wave frequency, $N^2 = -\frac{g}{\rho_*} \frac{d\rho_0}{dz}$ is the buoyancy frequency, and θ is the angle between the wave crests and the vertical (z direction). Here, g is gravity and $\rho_0 = \rho_0(z)$ is the unperturbed density stratification. The wave vector is then given by $k = k(\cos \theta, \sin \theta)$. As shown by *Maas and Lam* (1995), the focusing of waves dominates and leads to the formation of a wave attractor in most closed domains; *Maas et al.* (1997) verified this experimentally with waves excited through the parametric sub-harmonic instability of a vertically oscillated trapezoidal basin containing a linearly stratified fluid. These experiments have been reanalysed recently by *Lam and Maas* (2008), with the suggestion that the surface seiche may play an important role. The earlier experimental work on wave attractors was extended in chapter 3 using more sensitive and accurate experimental diagnostics. The existence of a harmonically generated wave attractor was presented and the equilibrium form of its spectrum was determined. Here, we extend this work further, considering both horizontal and vertical oscillations, and examining the velocity spectra.
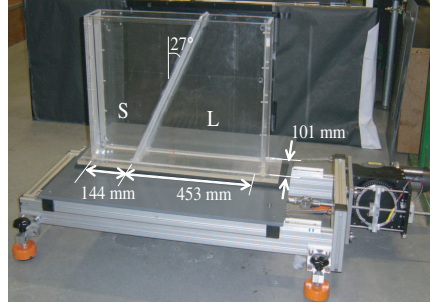
Figure 4.1: Photograph showing the trapezoidal tank on the horizontally oscillating table.

4.2   Experimental setup

A rectangular tank divided into two trapezoidal basins (see figure 4.1), filled to a depth H with a linear salt water density stratification, was placed on one of two oscillating tables. In the first series of experiments, the large (L) basin was used with $H = 200$ mm and the table was oscillated vertically with a typical amplitude of 120 mm. In the second series, the small (S) basin was used with $H = 230$ mm table was oscillated horizontally with a typical amplitude of

2 mm. The small basin (S) was also used with vertical oscillations when measuring the velocity field. In all cases a relatively strong initial stratification (typically $N \sim 3$ rad/s for basin L and $N \sim 2.1$rad/s for basin S) was used to allow accurate measurement of the internal wave field by synthetic schlieren (*Dalziel et al.*, 2000), for extremely small amplitude internal waves. We studied the initial establishment of the internal wave field after initiating the table oscillation, its steady state characteristics, and the decay of the field after the forcing was ceased. For the synthetic schlieren measurements, a 1.3 MPixel digital video camera was used to capture images of a back-lit pattern of random dots. The camera was located approximately 8m from the tank with its optical path shielded from unwanted thermal fluctuations in the laboratory by a polythene 'tent'. Complementary particle image velocimetry (PIV) measurements were obtained during the decay of the attractor. Very fine reflective flakes (Iriodin Glitter Bronze 530) were sprinkled on the surface and settled very slowly through the tank. The smallest particles (smaller than 10 m) proved to be successful tracers, despite the visibility of a given particle depending on its orientation. The image capture and analysis for both synthetic schlieren and PIV was performed using DigiFlow. Images were captured at four precise points during each period of oscillation of the table. For synthetic schlieren, a separate reference image was used for each of these points to avoid any spurious signals due to optical imperfections in the experimental setup. As the tank was not moving during the decay of the attractor, images were captured at 24 frames per second.

(a)   (b)
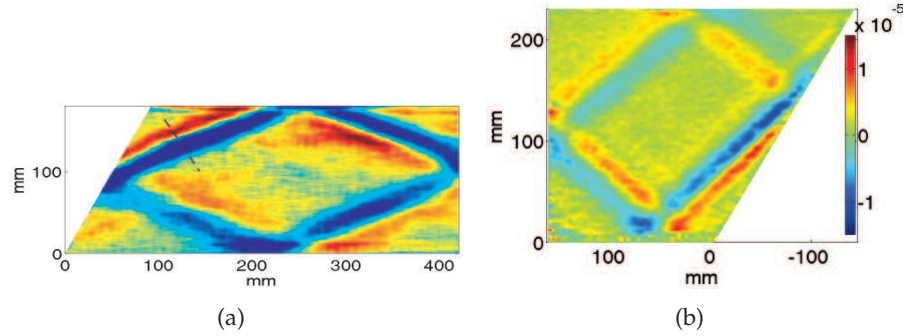
Figure 4.2: Snapshot of wave attractor showing the perturbation to the vertical density gradient. (a) Vertically oscillating table (basin L). (b) Horizontally oscillating table (basin S).

4.3 Results

The internal wave field achieves a steady state approximately 20 periods after the oscillation of the table is started. As can be seen from figure 4.2a for a vertically oscillating table, the perturbations to the density field lie dominantly on the diamond-shaped attractor first predicted by *Maas and Lam* (1995). Internal waves propagate around this attractor in a clockwise sense, undergoing amplification during their reflection from the sloping boundary. Here we visualise the vertical gradient of the density perturbation (i.e. $\partial\rho'/\partial z$), normalised by the vertical gradi-

ent of the background stratification ($d\rho_0/dz$). The waves are clearly linear with the perturbation a factor of 10^5 smaller than the background stratification.
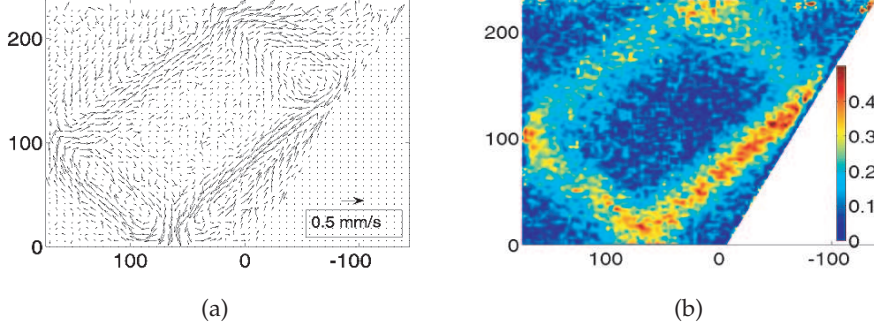
Figure 4.3: Velocity field for wave attractor. (a) Instantaneous field. (b) Root mean square amplitude.
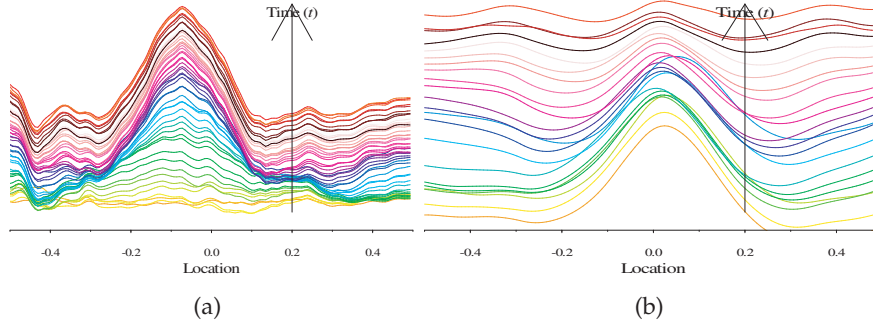
Figure 4.4: Profiles of the density perturbation across the section indicated in Figure 4.2a showing the evolution of the internal wave field. Each profile, shown once per period, is offset for clarity. (a) The initial development of the attractor. (b) The decay of the attractor after the forcing is turned off.

A time series of the density perturbation reveals the wave frequency is equal to the oscillation frequency. For the present vertically oscillating table the amplitude of the oscillation is insufficient to excite a parametric sub-harmonic forcing; we see instead the result of small imperfections in the vertical oscillation leading to the establishment of a harmonic seiche. The horizontally oscillating table also forces a harmonic seiche. In both cases the coupling of this seiche with the stratification drives the internal waves at the basin scale. Comparison of figures 4.2a, with the vertically oscillating table, and 4.2b with the horizontally oscillating table with similar experimental parameters confirm this. The surface modes are visible in the PIV measurements of the vertically oscillated table, as are the smaller length scales of the wave attractor. The velocities due to the attractor are easily recognised after harmonic analysis, as shown in figure 4.3. The initial evolution of the wave field is seen in figure 4.4a, which shows a series of profiles (at a fixed phase) of the horizontal density gradient at the dashed line indicated in

figure 4.2a. The higher wavenumber component in-creases along with the overall amplitude as the wave attractor builds up, indicating the transfer of energy from a basin-scale seiche to shorter wave lengths through the action of the attractor. Figure 4.4b shows how this then decays once the forcing is ceased, with the lower wavenumbers disappearing first as the attractor decays.

4.4 Discussion and conclusions

Chapter 3 used Fourier techniques to determine the form of the equilibrium spectrum for the density gradients. It was shown that energy injected at the basin scale (wavenumber k_0), propagates repeatedly clockwise around the attractor. Each focusing reflection from the sloping boundary transfers energy from wavenumber k_n to wavenumber $k_{n+1} = \gamma k_n = \gamma^n k0$, where $\gamma = \sin(\theta + \alpha)/\sin(\theta - \alpha)$ (here $\gamma \approx 1.6$ for basin L and 4.2 for basin S). In this chapter we extend the analysis to consider the velocity spectrum. A given packet of energy is introduced by the forcing at wavenumber $k_0 = 2\pi/H$, and through repeated reflections is taken to smaller scales. The energy flux associated with the packet is conserved during the reflection, and hence the energy density increases by a factor γ of at each reflection, a consequence of the reduction in the group velocity c_g. The packet of energy spends a period $t_{loop} = La/c_g$ at each wavenumber, where La is the distance around the attractor (which scales with H). However, in a real fluid, viscous dissipation will decrease the energy with both the dissipation rate and t_{loop} increasing with wavenumber. Incorporating the dissipation into the recurrence relation gives us the wave attractor's equilibrium energy spectrum:
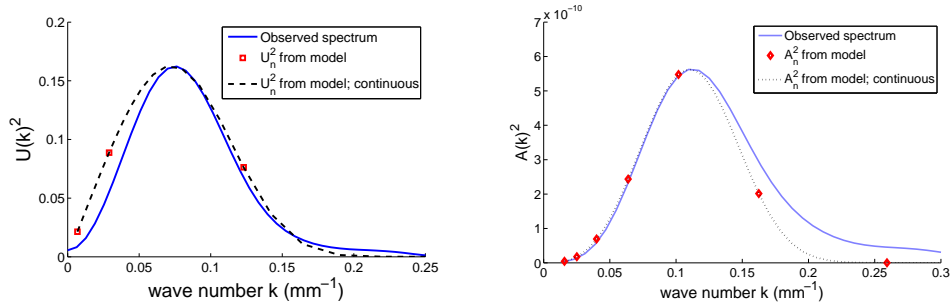
Figure 4.5: Comparison of modelled and observed equilibrium power spectra for (a) kinetic energy (U_n^2) and (b) density gradient (compare with figure 3.6).

$$U_n^2 = U_{n-1}^2 \gamma \exp\left[-\frac{2\nu L_a k_n^3}{N \sin\theta}\right] = U_0^2 \gamma^n \exp\left[-2\frac{\nu}{H^2 N}\frac{L_a}{H}\frac{(2\pi)^2}{\sin\theta}\frac{\gamma^{3n}-1}{\gamma^3-1}\right] \qquad (4.2)$$

The form of this energy spectrum differs by a factor of 2n from the power spectrum of the density gradient reported in chapter 3.

Figure 4.5a compares the observed equilibrium velocity spectrum in the vertically oscillated experiments with the recurrence relation (4.4), demonstrating close agreement in the functional

form of the spectrum. (Similar agreement was found with the model for the density gradient spectrum of the attractor in basin *L* as shown in figure 4.5b.)

We find that a horizonal oscillation of the tank gives internal wave attractors very comparable with the attractors that were vertically oscillated. In both cases a simple model is able to predict the shape of the spectrum as a balance between viscous dissipation and focussing. Whilst this model does not tie down the coupling between the forcing and the lowest wavenumber internal wave, it demonstrates clearly that the linear processes of wave amplification and viscous decay are sufficient to uniquely determine the form of the spectrum. Although in our experiments the wave amplitude and density gradients remain small, and the internal waves are linear, this may not always be the case. For sufficiently large basins, a given package of energy will undergo $p \sim ln(H^2N/v)$ reflections before viscous effects start to reduce the density gradients due to the waves. Thus we might expect to see that the density gradients found in the basin scale mode will be amplified by a factor approaching $\gamma^{3p/2} \sim (H^2N/v)^{(3/2)\ln\gamma}$. However, molecular viscosity and diffusivity are unlikely to remain the dominant dissipative mechanisms. In these large domains the wave will be amplified to a strongly nonlinear regime and hence exhibit different dynamics, and scattering from rough boundaries will modify the spectra. Lack of sufficient spatial resolution of the internal wave field in natural waters is probably the prime aspect inhibiting the observation of internal wave attractors in the field, although signs of internal wave focusing have been found on several occasions in a canyon (*Petruncio et al.*, 1997) and in small-scale lakes (*Boehrer and Stevens*, 2005; *Fricker and Nepf*, 2000).

Chapter 5

Observed scalar fields of an internal wave attractor

5.1   Introduction

Internal wave attractors can arise in stably stratified fluids in a confined domain (*Maas and Lam*, 1995) and are observed in the laboratory (*Maas et al.*, 1997). In a trapezoidal tank of uniform width with one sloping end-wall, internal waves reflect from the sloping wall into the domain and are focused towards an attractor. Repeated reflection from the sloping wall leads to an energy cascade to the higher wavenumbers (chapter 3). With a steady forcing at large scales, a balance is reached between the energy cascade and dissipation at the viscous scale, observed as a steady state internal wave attractor. The steady state internal wave amplitude can be increased by using different forcing mechanisms (chapter 4). Quite generally, stable continuously stratified fluids support internal wave beams resulting from a disturbance in the fluid (*Görtler*, 1943; *Thomas and Stevenson*, 1972; *Sutherland et al.*, 1999; *Peacock and Tabaei*, 2005; *Gostiaux et al.*, 2006). The properties of internal gravity waves in laboratory experiments have often been observed and measured using schlieren (*Mowbray and Rarity*, 1967) and more recently synthetic schlieren (*Dalziel et al.*, 2000; *Sutherland et al.*, 1999) techniques. Synthetic schlieren observations provide an integrated view and usually assume homogeneity of the fluid response in the direction of view, as if it were two-dimensional. These observations are sensitive to the gradient of the density perturbation, but it is possible to invert this to recover the perturbation density (see *Dalziel et al.* (2000) and in a simpler form in *Sutherland et al.* (1999)). However, it has become customary to present just the directly observed gradient information rather than the more natural density perturbation itself. By its very design, PIV (particle image velocimetry) leads to planar velocity measurements in the fluid. Again assuming homogeneity in one direction, the measured velocity fields can be combined in streamfunction ψ. The streamfunction relates the velocity fields, $(u, w) = (-\psi_z, \psi_x)$ (where we anticipate that in the following u will be the velocity component in the horizontal x direction and w the velocity in the vertical z direction). This streamfunction is also the field considered in the theory for internal wave attractors (*Maas and Lam*, 1995; *Maas*, 2005).

The laboratory experiments of chapter 3 were very successfully modelled in a numerical study by *Grisouard et al.* (2008) using the MIT general circulation model (*Marshall et al.*, 1997) in a two-dimensional set-up. Naturally, the calculations were done in terms of the density field, but, in order to compare with the observation from the laboratory, the gradient density fields were presented. The very strong correspondence between the results of laboratory and numerics allows for further comparison. It suggests that indeed the laboratory experiments can be assumed two-dimensional. If this is confirmed, the use of the streamfunction makes sense and wider connection can be made between theory and observations. The use of numerical simulation and laboratory experiment can then answer the open question as to what is the streamfunction of real viscous internal wave attractors.

Theoretically, the two-dimensional inviscid streamfunction for free internal waves in an enclosed domain with suitably re-scaled coordinates, can be found exactly by solving the spatial wave equation

$$\frac{\partial^2 \psi}{\partial x^2} - \frac{\partial^2 \psi}{\partial z^2} = 0, \tag{5.1}$$

with $\psi = 0$ at the arbitrarily shaped boundaries, by means of ray tracing (*Maas and Lam*, 1995).
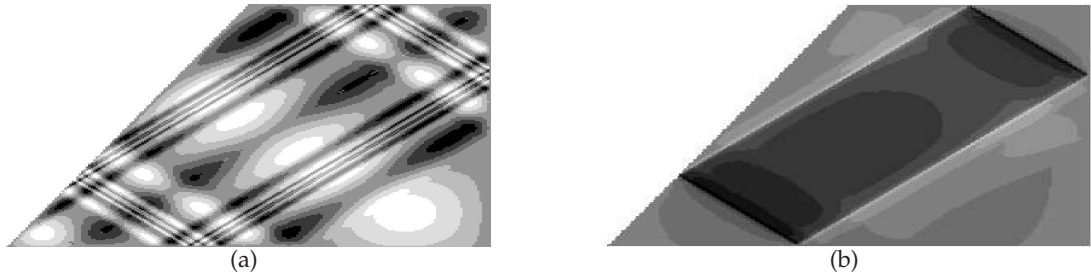
Figure 5.1: Streamfunction for inviscid internal wave attractor as found by *Maas et al.* (1997) and *Lam and Maas* (2008). a) A free wave solution, b) the forced wave solution. [Courtesy Frans-Peter Lam]

The equation can be solved by noting that an arbitrary complex function f is preserved along the characteristics $x - z$ and $x + z$. From any starting point at the surface the characteristics reflect through the domain, creating a web of connected points. Once the web is constructed, the prescription of f at the surface determines the spatial structure of $\psi(x, z)$. However, as f is preserved along the rays, there are connections between surface points. This means that the surface prescription of f should be limited to so-called fundamental intervals. This localised prescription then determines the structure of $\psi(x, z)$ in the whole domain. An example of such a streamfunction for a rectangular tank with a sloping side wall (trapezoid) was presented by *Maas et al.* (1997), see figure 5.1a. This geometrically constructed, unforced internal wave pattern is self-similar in space and has fine structures around the attractor, set only by the form of f across the fundamental intervals at the surface. The corresponding analytic solution for streamfunction recovers these fine structures and features a self-similar spectrum (*Maas*, 2009). A modified picture for the streamfunction was found (*Lam and Maas*, 2008) for a continuous forcing in the form of seiche wave at the surface. With the assumption that the imposed boundary values were not affected by values from elsewhere on the boundary, the modified picture for the streamfunction, although still inviscid, lost most of the fine structure. It became more a plateau type, that is, the streamfunction has constant values outside and inside the attractor with a sharp jump in value at the attractor, see figure 5.1b. Similar solutions for the streamfunction were found in numerical work, using a regularisation procedure for the discretised problem, based on minimisation of the energy (*Swart et al.*, 2007).

The objectives of this chapter are twofold. Building further on the successful two-dimensional numerical simulation of the laboratory experiments (*Grisouard et al.*, 2008), we now compare results from laboratory and simulation that both feature a tank scale sloshing as internal wave forcing. First we use the numerically obtained density field to verify the integration of the density gradient fields observed in the laboratory, and use this field to check if two-dimensional theory applies in the laboratory experiment. Secondly, we compare the observed streamfunction from both laboratory experiments and from numerical experiments with the prediction from two-dimensional theory for a sloshing type of forcing.

Fixed parameters				
Fluid height	H	$=$	250	mm
Length	L	$=$	453	mm
Width (Lab)	W	$=$	120	mm
Angle of sloping wall	α	$=$	0.47	rad
Buoyancy frequency	N	$=$	2.2	rad s^{-1}
Viscosity	ν	$=$	1	mm^{2}s^{-1}
Diffusivity	κ	$= 1.3 \times 10^{-3}$		mm^{2}s^{-1}
Prandtl number	$Pr = \nu/\kappa$	$=$	770	
Forcing period	T	$=$	5.12	s
Forcing frequency	$\omega_e = 2\pi/T =$		1.23	rad s^{-1}

Table 5.1: Parameters of both experiments §5.2.

5.2   Experimental setup

5.2.1   Description of laboratory experiments

For the laboratory experiments a trapezoidal tank containing a fluid with dimensions $L \times W \times H$ is used, see table 5.1. As the tank is relatively narrow, the motion was assumed to be nearly two-dimensional in previous work. The tank is filled using a pair of peristaltic pumps with density stratification that is linear in the vertical. The stratification is characterised by buoyancy frequency $N = \sqrt{-g/\rho_* \, d\rho_0/dz}$ with ρ_* the reference density of the fluid, $\rho_0(z)$ the density stratification and g the acceleration due to gravity. We use a density probe that can traverse vertically through the tank to establish N. To measure the motions of the fluid in the tank, we make use of both synthetic schlieren and PIV techniques, as described in chapter 4. For the synthetic schlieren, we have a dot pattern on a light-bank 0.5 m behind the tank fixed in the laboratory. The internal waves are forced by horizontally oscillating a platform supporting the tank with an amplitude of 2 cm at fixed frequency ω. This horizontal motion of the platform results in a weak sloshing of the water in the tank. The sloping side wall converts this barotropic sloshing into weak baroclinic internal waves that focus towards the attractor to form wave beams (chapter 3). As the tank and fluid are horizontally oscillating in front of the dot pattern, we phase lock the camera with the oscillation, capturing 32 frames evenly spaced through each forcing period. This allows us to perform the synthetic schlieren during the steady state of the experiment, with each of the 32 snapshots having its own reference frame to remove the influence of any optical imperfections in the tank. The particles for the PIV are Iriodin Glitter Bronze 530 from which we selected fine particles that slowly sink out in the fluid. The images used for the PIV are captured using the same phase-locked technique as for the synthetic schlieren. Both synthetic schlieren and PIV techniques rely on pattern matching. In the case of synthetic schlieren, the dot pattern gets distorted by density and hence refractive index changes in the fluid. The apparent displacement of the dots due to this distortion is determined by correlation with an unperturbed image. For the PIV, the particle patterns from frame to frame are tracked and represent the local Eulerian velocity field (though the particles are Lagrangian of course). The data are analyzed with the DigiFlow software (Dalziel Research Partners, Cambridge). For simplicity and to maximise the signal quality, we used separate experiments for the synthetic schlieren and PIV measurements. This was possible as the experiments proved to be highly repeatable, with differences of less than 3% even after emptying and refilling the tank. Typically,

we used a given stratification twice, first for synthetic schlieren then, after adding particles, for PIV, further reducing the difference in the conditions between two runs.

5.2.2 Description of numerical simulation

The numerical configuration is nearly the same as in *Grisouard et al.* (2008). The MIT general circulation model is used in a two-dimensional configuration to solve the nonlinear, nonhydrostatic, incompressible Boussinesq equations that govern the fluid dynamics (*Marshall et al.*, 1997). The simulations model diffusion using the ordinary Laplacian operator and are at a high enough resolution to ensure the motion is well resolved. Indeed, the spatial resolution is 0.5 mm in both vertical and horizontal directions, meaning that the width of the attractor (~ 50 mm) is resolved by about hundred points. For technical reasons regarding the way the code handles the equations, the numerical domain and the vertical density gradient are flipped in the z-direction relative to those of the experiments. The Boussinesq equations are indeed invariant under this transformation and to keep the comparison simple, the figures related to the numerical simulation will be flipped again in the z-direction.

The physical parameters are based on those used in the laboratory experiment and are listed in table 5.1. The numerical physical setting is nearly the same as in the laboratory, although some discrepancies remain. The purely two-dimensional numerics cannot take into account the dissipation that occurs in viscous shear layers at the two sidewalls in the laboratory experiment. Furthermore, the code allows us to set free-slip conditions at the bottom and (remaining) sidewalls in order to inhibit viscous layers that would be underresolved. As noticed in *Grisouard et al.* (2008), the absence of viscous effects at the walls might lead to a noticeable underestimation of the dissipation at the walls. The free surface is, contrary to the tank in the laboratory, located along the long base of the trapezium as a result of the vertical flip of the numerical domain. Another difference lies in the forcing that is of a different nature than the forcing in the laboratory one. Indeed, in the laboratory experiment the horizontal velocity of the fluid vanishes (relative to the tank) at the vertical wall, whereas for the numerical simulation we use an open boundary condition in the form of an oscillating current (u_b, w_b) at the vertical wall, reproducing a mode-1 internal wave :

$$u_b(t,z) = \frac{A\sqrt{N^2 - \omega_e^2}}{N} \sin(\omega_e t) \cos \frac{\pi z}{H}$$
$$w_b(t,z) = -\frac{A\omega_e}{N} \cos(\omega_e t) \sin \frac{\pi z}{H}$$

The amplitude of the mode-one wave, $A = 0.4$ mms^{-1}, is chosen so that the maximal velocity within the attractor field is in close agreement with the experimental one, which is the order of 10 mms^{-1}. A linear equation of state is used and thermal expansion coefficient is chosen such that the stratification is linear in temperature, and thus described by constant N. Thermal diffusivity κ is set to the value for the salt diffusion in the laboratory and we assume perfect insulation at the boundaries.

5.2.3   New method of representing experimental data

In most previous work the results of the synthetic schlieren imaging are presented in terms of the gradient perturbation buoyancy fields (*Yick et al.*, 2006; *Dalziel et al.*, 2007), $(b_x, b_z) = -g/\rho_* \nabla \rho$, as these are directly found from the distortions of the dot pattern by density perturbation ρ. Here, we introduce the integrated field

$$b = \nabla^{-1}(b_x, b_z). \tag{5.2}$$

Although we expect $b = \nabla^{-1}(b_x, b_z)$, direct integration is complicated by noise in the experimental measurements of the irrotational ∇b field, leading to an additional rotational part. We thus choose to integrate $b = (-g/\rho_*)\rho$ through a least squares procedure that minimises the energy contained in the rotational part. In particular, we note that the least squares solution for b on a regular two-dimensional grid with an irregular boundary, for each point in the domain or on the boundary, corresponds to taking the mean of the solutions calculated from the (up to four) immediately neighbouring points at which the solution exists. The structure of this problem then leads itself to a simple iterative solution, convergence of which is greatly enhanced by formulating in a multigrid framework. Only a single arbitrary constant of integration is required, here selected so that the spatial mean of b vanishes. We note in passing that setting $b = 0$ outside the domain and then using the regular procedure (e.g. using library function intgrad2 [John D'Errico, Mathworks]) for integrating the gradient in a rectangular domain leads to a slightly larger error, but provides a good alternative. The main problem points are found to be the sloping wall and the reflection points at the walls and surface. However, the difference fields, $b_{x,z} - \nabla(\nabla^{-1}(b_x, b_z))$ are at most 5% in the reflection points and much smaller elsewhere. We can use the same multigrid least squares iteration procedure to determine the streamfunction from

$$\psi = \nabla^{-1}(w, -u), \tag{5.3}$$

effectively minimising the energy of the non-solenoidal part of the measured (u, w).

Two-dimensional linear internal wave theory relates the buoyancy b with the vertical velocity. This is readily understood since, in the absence of diffusion, the density surfaces move up and down with the vertical velocity. The relation,

$$b = -i \frac{N^2}{\omega} \psi_x, \tag{5.4}$$

allows for another check on the integration. In the numerical simulation this relation is fully recovered, as expected from the two-dimensional code. In the laboratory experiment it provides both a check whether our integration of the buoyancy field works, and a validation of our assumption that we measure an essentially two-dimensional field. This assumption underlies most of the previous work on attractors in narrow tanks (*Maas et al.*, 1997) and chapters 3, 4 and 7.

5.3 Results

For the parameters used in the laboratory, the density gradient fields reveal a simple, essentially rectangular attractor with a shape very similar to that presented earlier in this thesis. From the PIV observations, we find the accompanying velocity fields. The forcing is somewhat stronger than that used in chapter 3 and by *Grisouard et al.* (2008), giving shear velocities in the attractor branches that are an order of magnitude larger, i.e. 10 mms^{-1}. The velocity fields in the laboratory are poorly resolved in places, due to the combination of low seeding densities (particularly under the sloping boundary), and the transport of PIV-tracers by the internal wave beams (chapter 7).

We observe the growth of an attractor in about twenty periods, featuring the generation of low-wavenumber internal wave beams from the sloping wall and the subsequent focussing, linear wavenumber cascade, towards the attractor. The wavenumber spectrum achieves a steady state once the high-wavenumber side of the spectrum reaches the dissipation length-scale. From this steady state we obtain the perturbation gradient density fields and velocity fields. The experiments were forced during 50 periods.

We calculate the density perturbation field by integrating the gradient fields measured by synthetic schlieren and then perform harmonic analysis on the integrated fields over the last twenty periods. The resulting perturbation density field is compared with the harmonic analysis of the perturbation density from the numerical simulation. From the harmonic analysis we obtain a real and an imaginary part that are combined to one complex field, so that we can plot both the amplitude and phase of this complex field. Amplitude and phase show the imprint of the attractor, visible in figure 5.2. The amplitude field reveals a decay in the clockwise direction of the branches (the internal wave beams) from the sloping wall. Compared with the numerical simulation, the cross-sections of the attractor branches are wider in the experiment but the values are comparable. The same difference in structure is observed in the phase, but again, the values are close.

Figure 5.3 uses relation 5.4 to compare the buoyancy field from the integrated synthetic schlieren data and the vertical velocity component from the PIV. As the synthetic schlieren and PIV measurements are performed separately, we leave out the phase part (the *-i* in equation 5.4), instead we compare absolute values. The structure of both fields is very similar, apart from the region under the slope where we can not measure the velocity. Where both measurements exist, the values differ by less than 5%.

As for the density, from harmonic analysis we obtain real and imaginary components for vertical and horizontal velocity fields. These are integrated to provide the complex amplitude of the streamfunction (and can be combined to the complex streamfunction field). We do this for both numerical simulation and laboratory experiment and the show real part in figure 5.4. The observed streamfunctions are very similar and reveal that a realistic streamfunction field is of simple shape. The numerical simulation results in somewhat lower values due to the more confined structure of the velocity field.
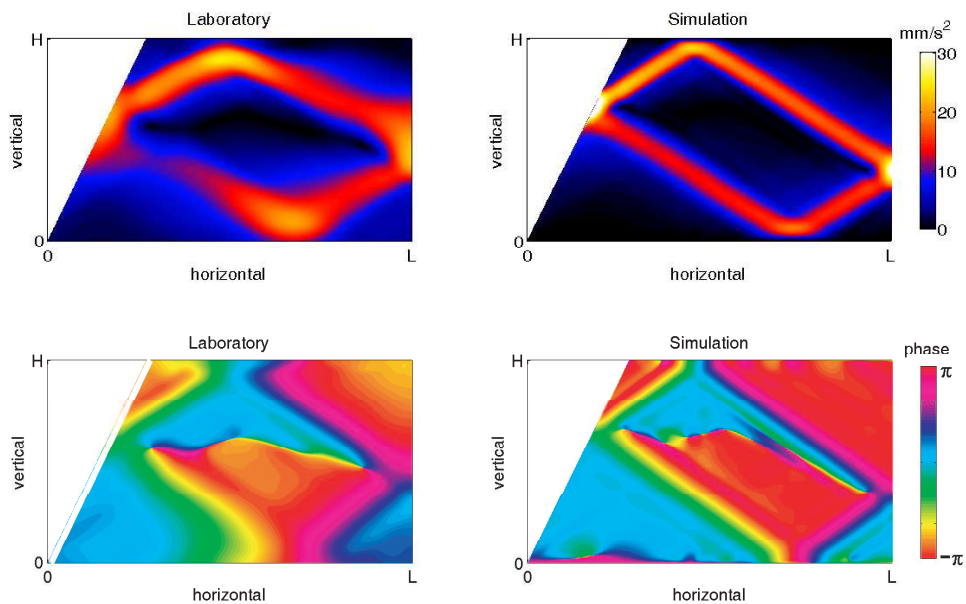
Figure 5.2: The amplitude and phase of the buoyancy after harmonic analysis. Laboratory on the left and numerical model on the right.
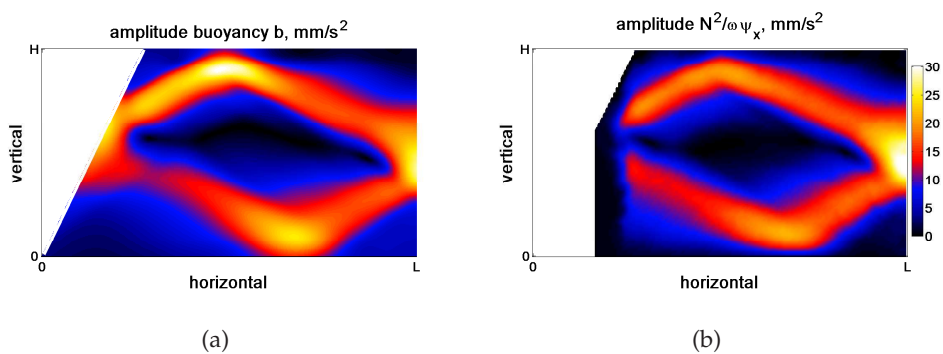

Figure 5.3: Comparison between observed buoyancy field amplitude and vertical velocity field via left-hand side and right-hand side in equation 5.4.
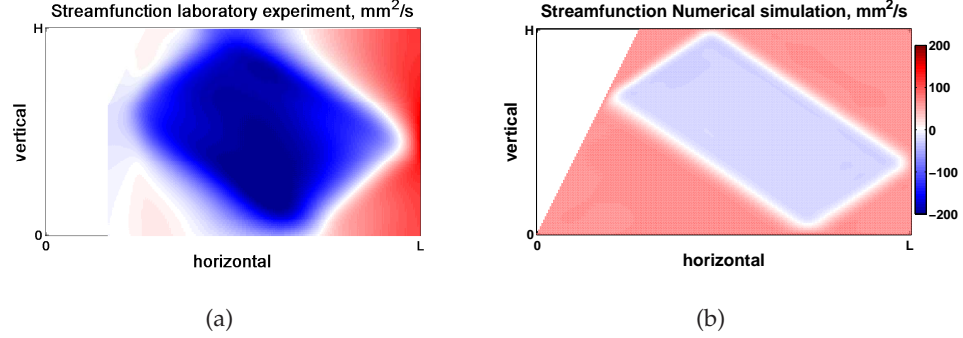
Figure 5.4: Streamfunction for experiment and numerical simulation.

5.4 Discussion and summary

The remarkable visual similarity between gradient density fields in the laboratory and from the numerical simulation was reported previously (*Grisouard et al.*, 2008). However, now we conclude not only that they look similar, but also that they correspond quantitatively. This is remarkable since there remain some distinct differences between the numerical simulation and the laboratory experiment. The first difference is in the forcing that is adjusted in the numerical simulation such that the peak velocities correspond to the peak velocities observed in the laboratory experiment. This does not mean the streamfunction values will match, only that the peak gradients in the streamfunction will match. In particular, given the difference in spatial structure, the range of streamfunction values will be greater for the experiments, as is indeed the case. The differences in spatial structure found between the two suggest that in the laboratory viscous dissipation plays a stronger role, especially at the higher wavenumbers. As the dissipation from the front and back wall is likely to affect only the low wavenumbers, it seems that the boundary layers where reflections occur are important in the laboratory experiment. The use of the streamfunction is only possible in a two-dimensional description of the flow. In our comparison we recognise that the numerical simulation is two-dimensional and that the laboratory is not. This may explain some further differences in the spatial structure of the streamfunction. However, the accurate recovery of the relation between observed buoyancy and vertical velocity reveals that the laboratory experiments are well described by two-dimensional theory (figure 5.3). The streamfunction fields are the plateau type of solution, very comparable to the solutions found for a sloshing forcing at the surface. It appears that viscosity smoothes the solution. This is true at least in the smaller laboratory scale where the linear energy cascade of the basin scale waves approaches the viscous scales after a small number of loops (chapter 3). The form of the streamfunction for much larger scale flows (e.g. astrophysical flows) remains an open question (*Ogilvie*, 2005).

In summary, we presented a new way of working with observations as typically found in laboratory experiments on stratified fluids. The integration of the observed/reconstructed perturbation density gradient fields reveals a physically more readily understood scalarfield, namely the perturbation density field. Comparison with a two-dimensional numerical simula-

tion, and with two-dimensional internal wave theory, reveals that the narrow three-dimensional tank can be considered effectively to be two-dimensional. This effective two-dimensionality also suggests that the description in terms of streamfunction is useful, so the velocity fields are integrated using the same least squares approach to the integration as for the perturbation gradient density fields. Although the streamfunction might arguably be a less physical scalarfield than the perturbation density field, it is the field considered by most theoretical work. We conclude that the streamfunction for a real internal wave attractor in a viscous fluid is of plateau/simple type.

Chapter 6

Robustness of internal wave attractors to perturbations

6.1 Introduction

Stably and continuously stratified fluids support oblique internal wave beams, resulting from a disturbance of the fluid (*Görtler*, 1943; *Mowbray and Rarity*, 1967; *Sutherland et al.*, 1999) (*Peacock and Tabaei*, 2005; *Gostiaux et al.*, 2006). The dispersion relation describing these waves, $\omega = N \cos\theta$, relates the frequency ω to the angle of energy propagation θ relative to the vertical z. The buoyancy frequency $N = (-g\rho_*^{-1} d\rho_0/dz)^{1/2}$ is a measure for the background density stratification $\rho_* + \rho_0(z)$, where ρ_* is the average density of the fluid, $\rho_0(z)$ the vertically varying density and g gravity. The dispersion relation does not depend on the wavelength. In fact, a disturbance with a single frequency normally results in a spectrum of wavelengths (*Thomas and Stevenson*, 1972). At sloping boundaries, the angle θ is preserved so focussing and defocussing can occur (*Dauxois and Young*, 1999) where the wavelength and amplitude of the reflected wave differ from that of the incident one. In a confined domain, focussing dominates (*Maas and Lam*, 1995) and internal wave attractors (IWAs) can arise. Such IWAs have been observed in the laboratory in a narrow trapezoidal tank, filled with a stable, linearly stratified fluid (*Maas et al.*, 1997). The focussing reflection from the sloping wall leads to an energy cascade towards higher wavenumbers (chapter 3), eventually reaching a balance between forcing at the larger scale and dissipation at the viscous scale, observed as a steady state IWA. The clear steady state IWA can be forced by subjecting the fluid to a small horizontal oscillation (chapter 4). The fluid response in terms of an IWA is a fundamental property of almost any periodically forced continuously stratified fluids in an enclosed domain. However, previous observations have been restricted to uniformly stratified fluids in a simple trapezoidal tank with smooth boundaries, lacking any mechanism for scattering of internal waves. Moreover, the forcing frequencies historically used were chosen such that only the simplest of all attractors was found. A natural question then is whether IWAs are also found when perturbations to this simple domain shape or to the linear stratifications are made, or when the forcing frequency is varied.

Studies of reflection of 2D internal wave beams from topography or sharp density jumps have revealed that scattering of the beam structure occurs (*Nye*, 2009; *Gerkema*, 2001). Given the dispersion relation, a significant part of scattering of internal wave beams from topography consists in fact of focussing and defocussing. This can be easily seen by inviscid ray tracing (*Longuet-Higgins*, 1969a) (the same ray tracing that can be used to find the attractor). For subcritical reflection (beam angle steeper than the angle of the topography) from a sawtooth topography, recent experiments (*Nye*, 2009) show that there occurs some back-reflection of the waves, defined as the change of sign of both horizontal and vertical wavenumbers. This is not captured by ray tracing, which predicts only forward reflection (the change of sign of only one component of the wavenumber vector *Longuet-Higgins* (1969a)). Partial reflection can occur when a wave beam propagates through a changing density gradient (*Nault and Sutherland*, 2007; *Marthur and Peacock*, 2009). In that situation, it is also possible that the internal waves are trapped in parts of the fluid. Given that IWAs consist of multiple reflections and many wave scales, the above effects will play an important role when studying the implication of rough topography or non-uniform density gradients on IWAs.

In this chapter we will study the existence of more complicated IWAs in essentially two-dimensional domains, and employ ray tracing to predict the shape and location of the IWA (*Maas and Lam*, 1995). Our starting point is the attractor presented in chapter 5. This will act

as default experiment to which perturbations will be made. First, we vary the frequency and show that the fluid response with strong internal wave motion depends on the complexity of the IWA that can be formed. Second, we use a non-uniform stratification and show that the attractor now consists of curved rays, albeit reached only after going through an interesting transient phase. Then, we perturb one of the side walls with a variety of regular corrugations and find that the small scale focussing from these corrugations complicates the attractor shape but does not suppress the attractor. Finally, we show that attractors, as predicted by ray tracing (*Maas and Lam*, 1995), also arise in a parabolic domain.

6.2 Experimental set-up

In the idealised laboratory set-up, we use a narrow tank with a single sloping wall, making an angle α with the vertical. The tank has dimensions $L \times W \times H$, see table 6.1, and is the one also used in the previous chapters. We fill this tank using two computer-controlled peristaltic pumps feeding in fluids of different densities to produce the desired stable stratification. In this study we use both a linear density stratification and a stratification that is characterised by a steeper gradient in the middle. For the final experiment we use a parabolic channel of width W and filled with a linearly stratified fluid of height H.

To measure the motions of the fluid in the tank, we use synthetic schlieren (*Dalziel et al.*, 2000), employing a fixed dot pattern on a light-bank 0.5 m behind the tank. When viewed through the tank, any change in density gradient $\nabla \rho'(x, z, t)$ in the fluid, results in apparent movement of the dots, due to changes in the refractive index. Synthetic schlieren relies on the correlation of these apparent displacements of the dots and compares them to an unperturbed image. The data are analysed with the DigiFlow software (Dalziel Research Partners, Cambridge). We use a density probe that can traverse through the tank to measure the unperturbed stratification and hence N. The internal waves are forced by horizontally oscillating a platform supporting the tank, with an amplitude of 0.03 m at an adjustable frequency. We phase lock the camera with the oscillation, capturing 16 frames evenly spaced through each forcing period. This enables us to perform synthetic schlieren during the steady state of the experiment, with each of the 16 snapshots having its own reference frame. We will present phase and amplitude of the horizontal component of the perturbation buoyancy gradient $b_x = -g\rho_*^{-1}\partial\rho'/\partial x$. We run the experiments for 50 oscillation periods and present most of the data after harmonic analysis (HA) at the forcing frequency from the last 20 periods in the steady state. In all experiments we find that the forcing frequency is the only significant frequency. The experiment in the parabolic channel is presented upon HA at the forcing frequency of the first period after we stopped the forcing (120 snapshots per period). Experimental parameters for this experiment are found in table 6.2.

For the experiments with the corrugated side walls we had 90° 'sawtooth' corrugations of varying lengthscale, with parameters given in table 6.1. The corrugations were attached to the vertical side wall of the tank. After placement of the wall in the emptied tank, the tank was refilled with a fluid having a linear stratification.

Fixed parameters			
Length	L	453	mm
Width	W	120	mm
Angle of sloping wall	α	0.47	rad

Default experiment			
Fluid height	H	260	mm
Stratification	N	2.5	rad s^{-1}
Forcing frequency	ω	$2\pi/5$	rad s^{-1}

Frequency scan			
Fluid height	H	300	mm
Stratification	N	2.15	rad s^{-1}
Forcing frequency	ω		
I		$2\pi/5.14$	rad s^{-1}
II		$2\pi/4.80$	rad s^{-1}
III		$2\pi/4.28$	rad s^{-1}
IV		$2\pi/3.86$	rad s^{-1}
V		$2\pi/3.68$	rad s^{-1}
VI		$2\pi/3.52$	rad s^{-1}

Non-uniform stratification			
Fluid height	H	290	mm
perturbation height	h	50	mm
Stratification basic	N_0	1.8	rad s^{-1}
Stratification perturbation	N_1	2.1	rad s^{-1}
Forcing frequency	ω		
NU-I		$2\pi/4.5$	rad s^{-1}
NU-II		$2\pi/4.7$	rad s^{-1}
NU-III		$2\pi/4.9$	rad s^{-1}

Corrugated wall			
Fluid height	H	260	mm
Stratification	N	2.5	rads^{-1}
Forcing frequency	ω	$2\pi/5$	rads^{-1}
Corrugation wall	peak angle (degrees)	nr peaks	
P-II	45	20	
P-III	45	7	
P-IV	45	3	

Table 6.1: Parameters for experiments

6.3 Results

6.3.1 Default experiment

For a fluid with a linear density stratification, N is constant. This means that for a given forcing frequency the wave angle θ is fixed. Therefore, in an enclosed two-dimensional domain, the path followed by internal waves and their reflections can be found by means of a simple iterative procedure. For smooth walls, analytic expressions can be found coupling subsequent reflection points at the walls (*Maas and Lam*, 1995; *Maas*, 2005). However, such expressions become unwieldy and unnecessary when complicated domain shapes are considered, such as domains with sawtooth side walls. The iterative procedure, however, can be simply described for constant N. Start with a point at the surface of the tank and 'shoot' a ray into the domain at angle θ to the vertical. Find the location of intersection with the wall. The direction that the reflected wave takes is along the only other ray inside the fluid domain that passes through that point at an angle θ to the vertical. If, at the reflection point, the wall is steeper than the ray, then the vertical direction of propagation is maintained. If the wall is less steep, then the direction of vertical propagation is reversed. This determines the new direction of the ray and the procedure is repeated at the next reflection. The rays are followed for 1000 iterations, creating webs. An example is given in figure 6.1a, where the rays are followed from two points at the surface, the squares coloured red and blue. Both the red and blue webs converge to the black rectangle, the IWA.

Figures 6.1b,c demonstrate that this attractor is indeed found in our default experiment and is very similar to the one described in previous chapters. From the very gentle sloshing of the fluid in the tank, large scale internal waves are seen to focus onto the attractor. The focussing continues until the smallest wavelengths reach the viscous scale. This process takes about 25 periods. After its initial establishment, the attractor is in steady state. The observations from the last 20 oscillation periods in this steady state, sampling 16 frames per period, are presented after HA in amplitude (figure 6.1b) and phase (figure 6.1c) plots. The amplitude plot shows the usual decay of the wave amplitude in the beams due to viscous attenuation as we follow the attractor in the clockwise direction, starting from the sloping wall. The shearing nature of the motion in the beams and the cross-beam phase propagation become visible by the rapid change in phase across the beams.

6.3.2 Frequency scan

We vary the frequency in the series of experiments indicated in table 6.1. The experiments are performed one after another, with sufficient time between each experiment to allow the waves to dissipate. By varying the wave angle, i.e. frequency, in the ray tracing we find various attractors. The resulting IWA, comprising only the converged rays, are shown in the left-hand column of figure 6.2. Clearly, when the frequency changes the IWA shape changes, and the experiments reveal clear differences in response of the fluid depending on the forcing frequency. Over continuous frequency intervals, the number of boundary reflections is fixed and, when the number of reflections is small, the IWA has a relatively simple shape. We will denote these simple IWA by the number of reflections at the top and at the vertical side wall respectively.
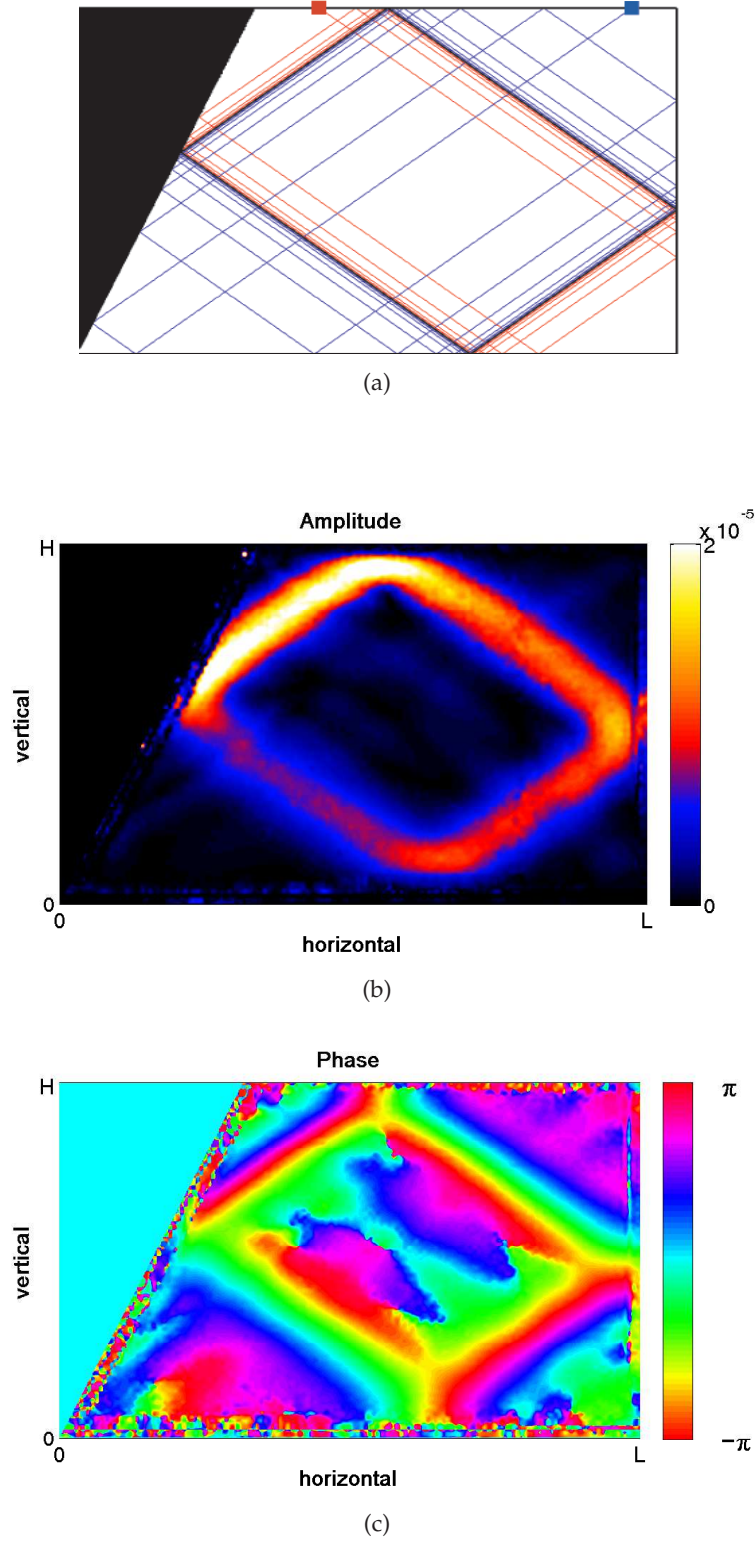
(a)

(b)

(c)

Figure 6.1: Example of ray tracing for the default parameter values. Harmonic amplitude (s^{-2}) and phase from observations of b_x. Axes and definition of colours will be the same in the following plots.

This means that the IWA in the example of figure 6.1 is a 1-1 IWA while the one at the bottom of figure 6.2 is a 2-1 IWA.

The central column of figure 6.2 shows the amplitude of the corresponding experimental IWA, while the right-hand column shows the phase. The colour scheme for these two columns is identical to that used in figure 6.1. The first experiment (I) has a frequency that corresponds to a frequency a bit below the value of the boundary of the frequency interval for a 1-1 IWA. Although the response is much less pronounced than that of the default IWA, and ray tracing does not suggest a simple structure, HA still reveals a weak signal. This signal does have a clear phase signature that reflects aspects of the ray tracing. During the next two experiments (II&III), the frequencies are in the 1-1 attractor interval and show a clear amplitude and phase structure comparable to the ray tracing. In the subsequent frequency regimes (IV&V), we find very complex attractors that consist of many loops through the domain. The experiments reveal a weaker response of the fluid. Note however, that the amplitude and phase again bear traces of the structure from the ray tracing, especially near local zones of denser webs. In the 2-1 attractor frequency domain (VI), we find again a clear response of the fluid.

6.3.3 Non-uniform stratification

The tank is filled with a fluid characterised by a region of higher N towards the centre of the tank. The measured profile of the density is shown to the right of figure 6.3. We approximate this stratification by $N^2(z) = N_0^2 + N_1^2\text{sech}^2((z - H/2)/h)$ that we will use for the ray tracing. The ray tracing leads to attractors, figure 6.3; though the rays are curved they can be computed exactly. For details on this ray tracing, see the Appendix. We perform three experiments with different forcing frequencies, varied in the 1-1 attractor frequency interval for the fluid with a linear stratification N_1 (fluid height H), given in Table 6.1.

It is worth describing how the fluid reaches a steady state wave field in these non-uniform stratifications. When the oscillation starts, we observe a strong response in the middle of the tank, with beams that reflect within this more strongly stratified region, reminiscent of wave beam trapping (*Marthur and Peacock*, 2009). Initially, internal waves radiating from the sloping side wall have length scales comparable to h, the height of the strongly stratified middle of the stratification. For these larger scale waves, the region is only partially transmissive (*Nault and Sutherland*, 2007); scattering takes place. This is not covered by standard geometrical ray tracing which invokes WKB theory (*Lighthill*, 1978), requiring wave scales much smaller than h. However, within about 3 periods of oscillation, wave beams are seen in the whole tank with reflections reaching the sloping wall again. Once the waves get focussed their length scale decreases so that the transmissivity of the middle region becomes larger and WKB theory becomes more applicable. From that moment on, the focussing towards the attractor proceeds and reaches steady state after about 25 periods.

The patterns of the waves found in the steady state are easily identified as an IWA, especially in the phase of the HA in figure 6.3. Due to the varying stratification, the wave beams are curved and compare well with the ray tracing. Faint patterns in the background give the impression there is another attractor visible, that we do not find from ray tracing for the given stratifications. Given the phase and thus direction of energy propagation in these beams, we conclude that partial reflection from the strongly stratified region is the source of these struc-
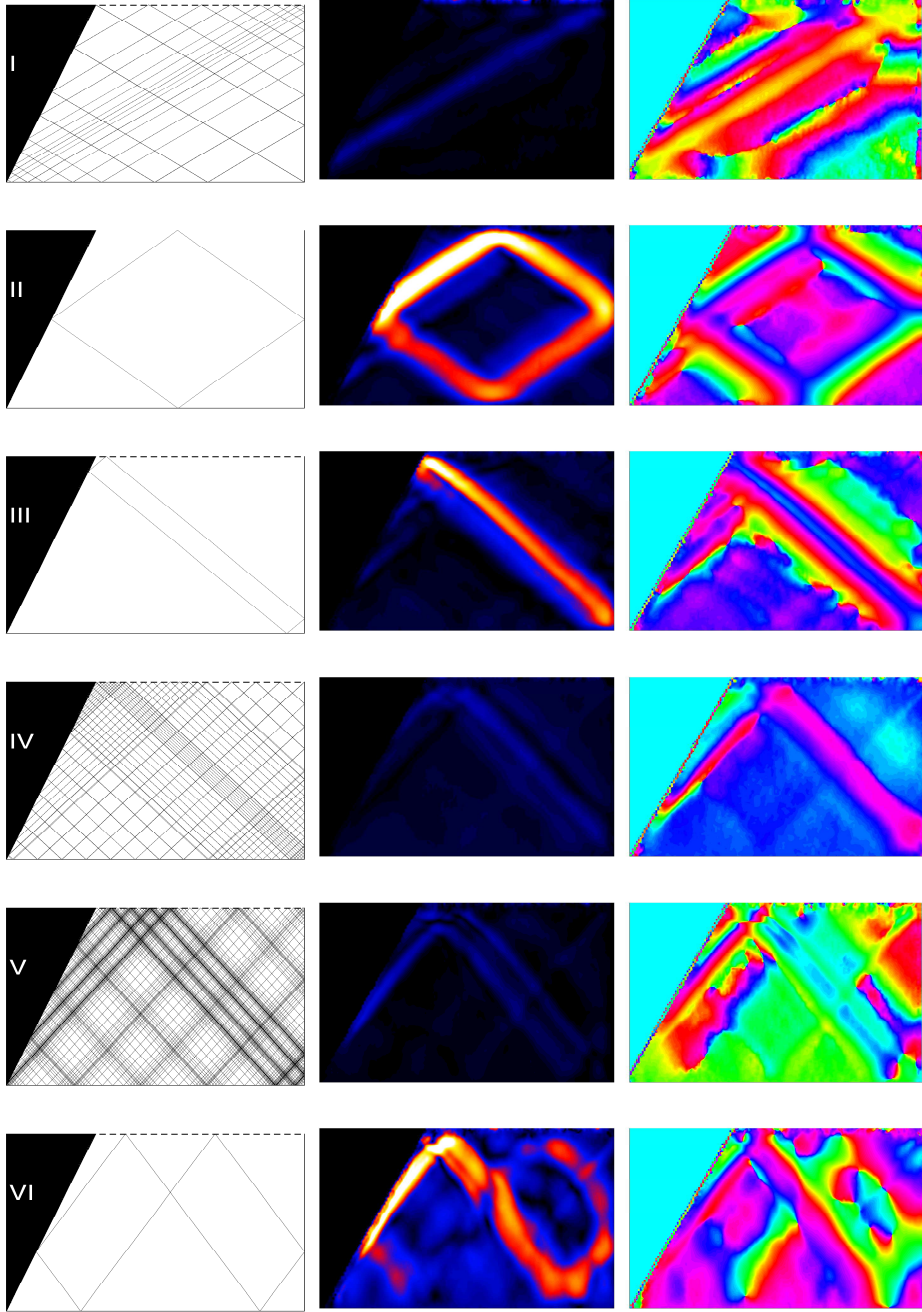
Figure 6.2: IWA spatial structure predicted by ray tracing for varying forcing frequency (left panel). Observations of the observed steady state patterns in terms of harmonic amplitude (middle panel) and phase (right panel). Labels I-VI in the ray tracing plots, refer to experimental condition in Table 6.1. For colour and axes properties see figure 6.1.
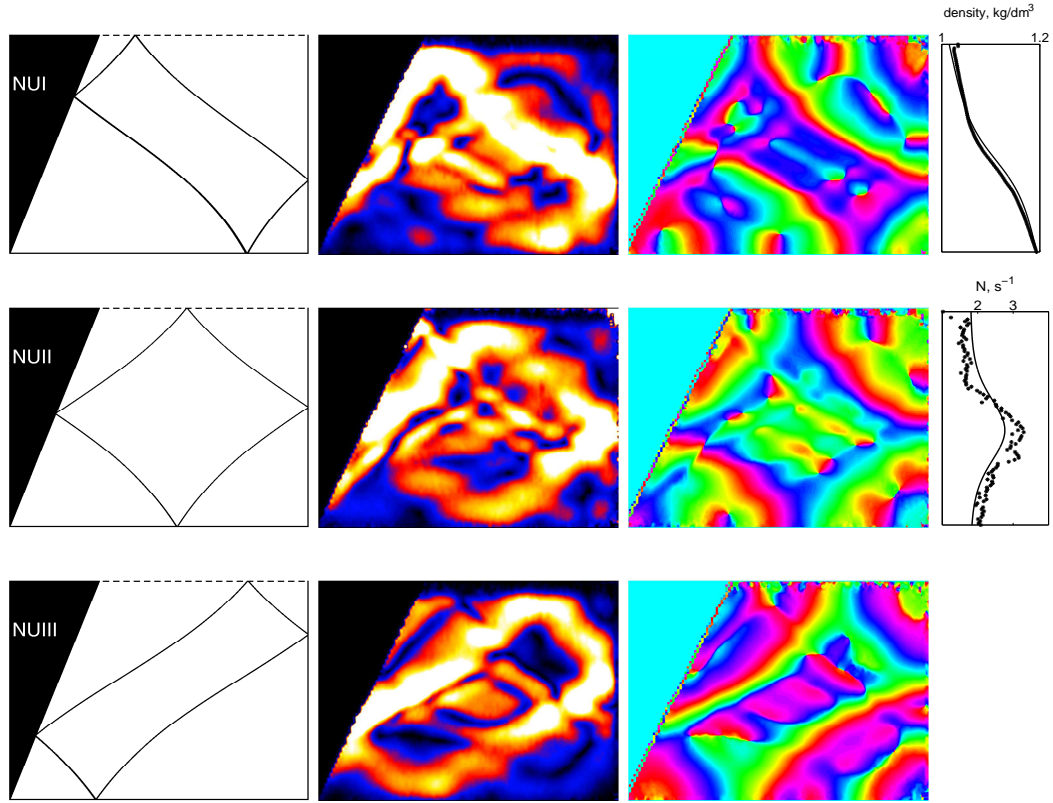
Figure 6.3: As in Figure 6.2, but for experiments with non-uniform stratification, for three different frequencies in the 1-1 attractor window. On the right, the measured density profile and $N(z)$, the lines show the approximation used for the ray tracing.

tures.

6.3.4 Corrugated wall

To understand ray tracing for a domain with a sawtooth side wall, we start with the smooth side wall and 1-1 attractor. Then we vary the number of peaks on the wall, see left-hand column of figure 6.4. For these domains, the focussing of internal wave energy takes place at both the sloping wall as well as at the corrugations. The wave focussing of the corrugated side wall is visualised by plotting an incoming bundle of rays, the blue lines, that are focussed after reflection, the red lines. As the topography is subcritical we find no backward reflection from the ray tracing. Continuing the ray tracing leads to attractors very similar to the ones found in the domains without perturbation on the side wall, shown by the black lines in figure 6.3. It turns out that due to the corrugations the original IWA splits in two. In fact, there is a third attractor (not shown) in the defocussing (counter-clockwise) direction of the sloping wall. However, the effect of the sloping wall is that most of the rays end up in the focussing

direction of the sloping wall and that the focusing power in the counter clockwise direction is significantly less. The third IWA exists due to the combination of a defocusing reflection at the sloping wall and an only slightly stronger focusing one at the corrugations. The position of this third attractor is between the two attractors in the focussing direction. The positions of the attractors are determined by domain and frequency as before. The separation is due to the peaks that are nearest to the attractor in the unperturbed case. Note that the ray tracing for the corrugated walls in figure 6.4 shows two 1-1 attractors and not a 2-2 attractor.

The experiment *PI* with the smallest perturbations, the only one having a slightly larger fluid height than the default depth $H_{PI} = H + 40$mm, reveals an IWA very comparable to the default case. The initial transients coming from the perturbation on the side wall do not influence the IWA build-up. However, there are thin layers of mixed fluid between corrugation peaks that slowly spread out horizontally during the experiment and change the stratification in the very long term. In the relatively short time of the experiment, it seems that the only effect of the perturbation is that the attractor branches are thinner: experimentally the multiple attractors, found by ray tracing, are not distinguishable.

In experiment *PII* the internal wave pattern changes compared to the default experiment. However, the pattern in steady state is still recognised as a pair of distorted IWAs. The focussing of the corrugation visually breaks the beam structure of the branches. This sort of focussing is also seen in the ray tracing for the corrugation, and is very similar with the observations. In both experiments *PII* and *PIII*, the reflection at the corrugation is found at those locations where the attractor branch reflects in the unperturbed situation, indicating the importance of the focussing of the sloping wall.

The reflections from the side wall are further investigated using the Hilbert transform (HT) on the HA fields (*Mercier et al.*, 2008). With the HT we can identify the directional component of the IWA branches and can separate incoming from reflected waves, indicated by the white arrows in figure 6.5a. From the ray tracing we found that all rays should be reflected forward. However, this was not found in laboratory experiments on subcritical reflections due to boundary layer and non-linear processes *Nye* (2009), and could potentially lead to the formation of the 'third' attractor in the counter-clockwise direction. Considering the waves in experiment *PII*, part of the wave energy is indeed back-reflected in the counter-clockwise direction, indicated by the white ellipses. That these reflections bear the imprint of the corrugations is most clearly seen in the phase plots, see region indicated by ellipses in figure 6.5b. The imprint is seen in the two upper branches of the attractor, but is not seen after reflection from the slope, which is defocussing in the counter clockwise direction. In the forward (clockwise) reflection, the imprint of the corrugation is clearly seen as a result of the focussing at the corrugations (lower left panels). The dominant direction of propagation remains clockwise.

6.4   Parabolic channel

As a last (finite amplitude) perturbation to the domain, we consider a quasi-two-dimensional parabolic channel specified in table 6.2. For this domain, the ray tracing was investigated in
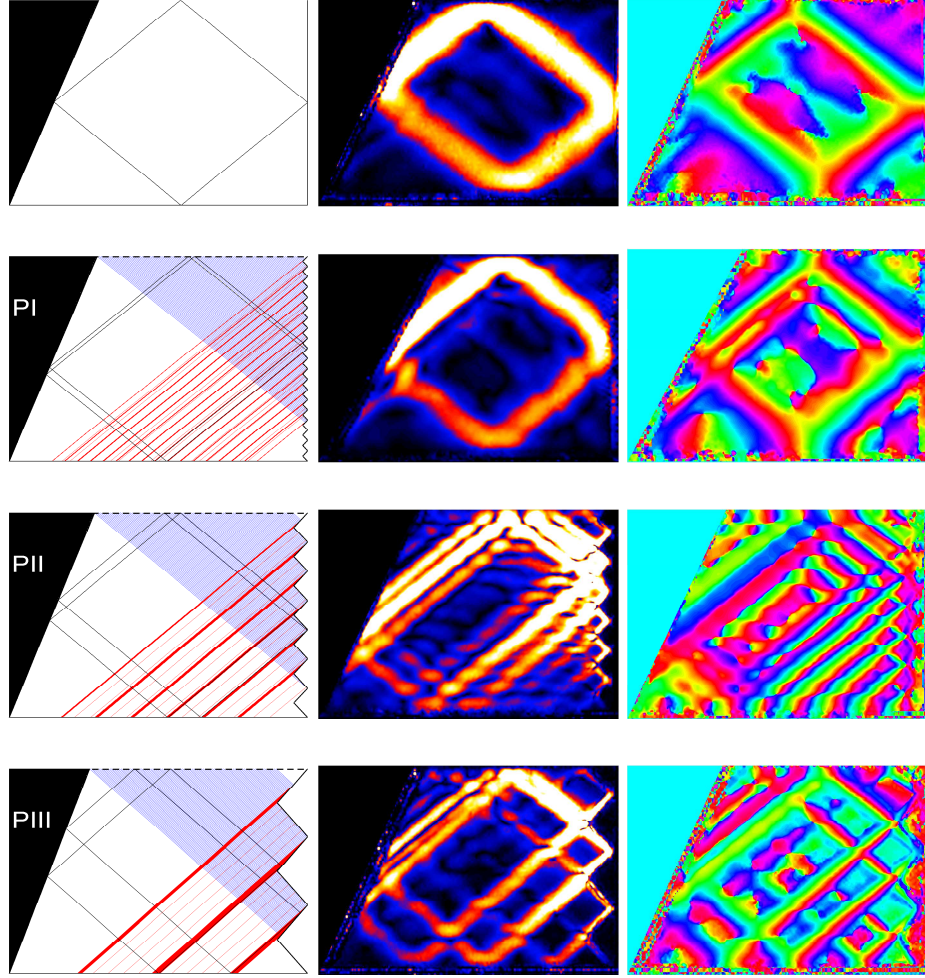
Figure 6.4: As Figure 6.2, but now for experiments with corrugated side wall with decreasing number of corrugations from *PI* to *PIII*. Raytracing for approximations of the experiments showing the break up of incoming rays (blue lines) by the topography after one reflection (red lines) and subsequent focussing onto the attractors (black lines). Observations of harmonic amplitude and phase resemble these patterns.

(*Maas and Lam*, 1995) and numerical studies of the response of a fluid in parabolic domains resulted in attractors, both in two-dimensions (*Münnich*, 1993) as well as in three-dimensional channels (*Drijfhout and Maas*, 2008). We focus on the frequency that leads to the simplest attractor as presented by the ray tracing in figure 6.6a. This IWA is presented after HA of the initial periods of the unforced decay, where we have a high sampling rate.

We observe a clear IWA structure in both amplitude and phase at the forcing frequency, figure 6.6b,c. Since this attractor is a balance between defocussing and focussing, the amplitude of the internal waves, upon focussing reflections high-up at the slopes, is much stronger than the amplitude in the interior. The phase pattern, however, is a clear indication of the continuation

(a)   (b)

Figure 6.5:   Hilbert transform of experiment PII for a) amplitude and b) phase, arrows indicate the direction of propagation. Part of the wave energy is back-reflected in the counter-clockwise direction, indicated by the ellipses. For colour and axis properties see figure 6.1.
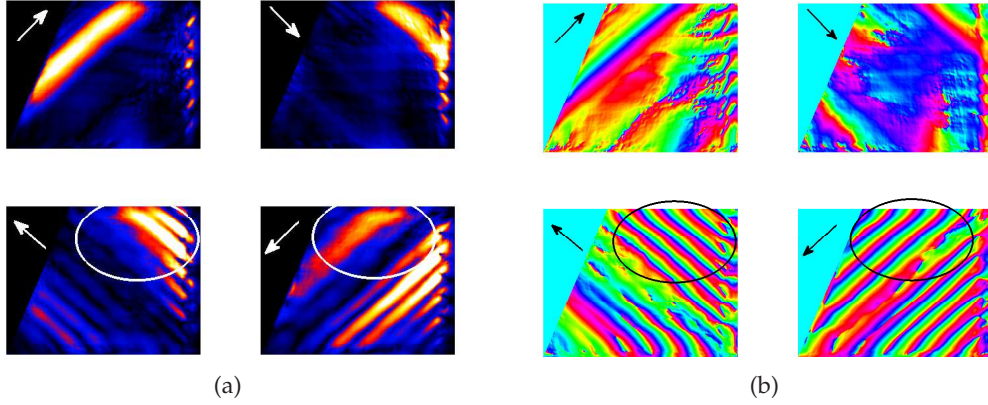
Parabolic channel

Fluid height	H	260	mm
Width	W	120	mm
Half length at surface	R	280	mm
Stratification	N	2.5	rad·s^{-1}
Forcing frequency	ω	$2\pi/5$	rad·s^{-1}

Table 6.2: Parameters for experiment in parabolic channel

of the energy on an IWA.

6.5   Discussion and Conclusion

In the simple domains in which IWAs have been observed in previous work, ray tracing was always used as a tool to find the attractor location. The present observations have shown that the use of ray tracing in distorted domains can still predict the position of the attractor. Changing the forcing frequency leads to a change in shape of the attractor and sometimes the fluid seems not to respond to the forcing. However, even when the ray tracing shows a very complicated attractor, we find that some traces remain in the phase of the HA.

The values of the parameters used for the ray tracing are representative for the experiments performed. However, especially for situations where the attractors consist of complicated webs, the results from ray tracing are very sensitive to small variations in frequency or stratification. Given the uncertainties in the observations, typically in the order of a few percent, the ray tracing gives an approximate idea of the attractor. Ray tracing can be modified to predict wavenumber spectra (chapter 3), but only for relatively simply attractors where there is good spatial separation between branches. Such modified ray tracing assumes a balance between focusing and viscous dissipation over the length of the attractor. Given the complicated

(a)

(b)

(c)
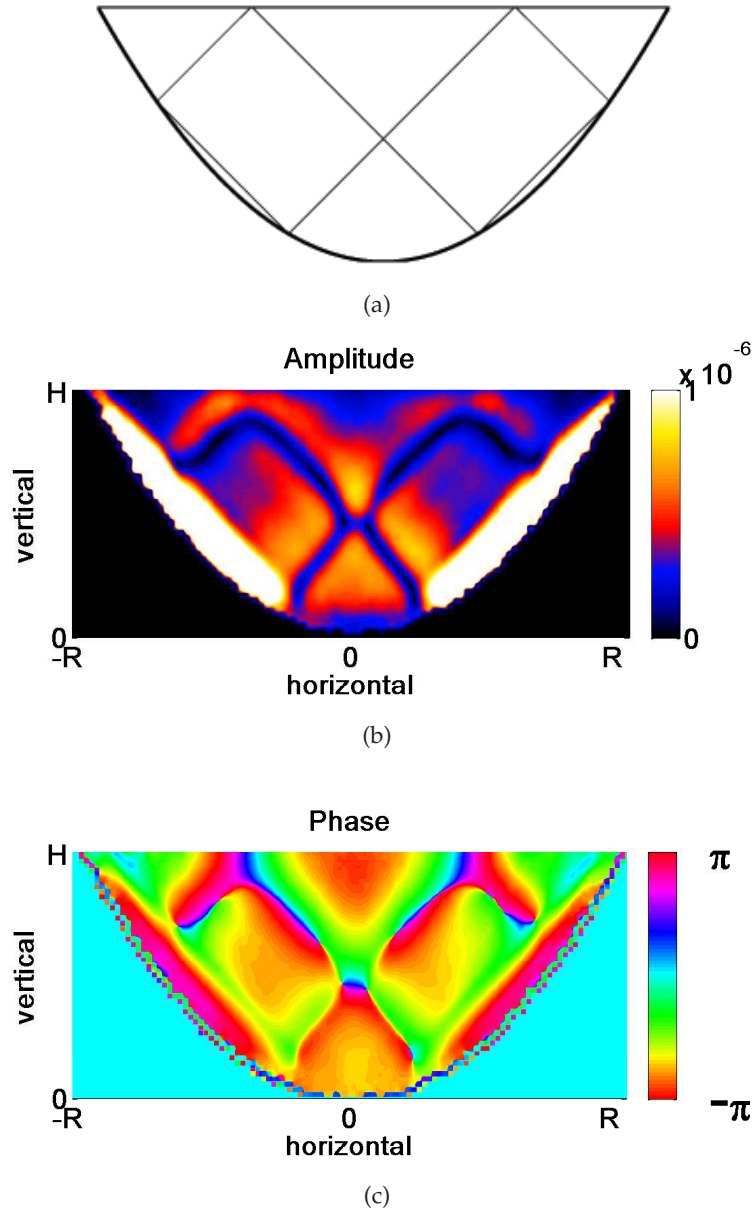
Figure 6.6: a) Ray tracing, b) amplitude and c) phase for experiment with parabolic channel.

path of the rays for experiments I, IV and V, it is surprising to find that wave patterns are observed that overcome viscous damping. It is clear that the simpler the attractor, the stronger the internal response of the fluid.

A similar strong internal response of the fluid is observed when a simple attractor can be formed in domains to which perturbations in stratification or domain shape are made. All IWAs initially grow by the ongoing focussing of large scale waves at the sloping wall starting

from the weak sloshing of the water in the whole tank. Most notably, this is of importance when the stratification is non-uniform. In this situation, the large scale waves go through the middle layer and reflect from it. Still, the change in stratification cannot prevent the focussing at the sloping wall and eventually the waves can penetrate through the middle layer and the attractor is formed.

The main effect of the topography can be seen as adding another set of focussing reflections. This means that the transfer to the viscous wave length takes fewer reflections and input energy is dissipated faster. However, when the size of the topography is close to this viscous scale (experiment P1), the effect on this dissipation is limited. The focussing on larger sized topography is found only at locations where ray tracing predicts the attractor(s). This indicates that the focussing and counter-clockwise back-reflections are a result of the IWA formation and not the source of internal wave energy. Spectral analysis, not presented here, indeed reveals that the reflection from the corrugation follows the growth of the waves focussed by the sloping wall. More than one attractor is formed, but the topography limits growth both in spectral shape and amplitude.

We conclude that the occurrence of wave attractors has to be considered whenever internal waves are found in stratified fluids. The fundamental response of the confined stratified fluids studied in this paper has to be described in terms of internal wave attractors. These attractors are robust. Their appearance does not depend on the geometrical setting being perfect (e.g. non-uniform stratification or domain). This conclusion has implications for stratified fluids in geophysical settings. The attractor in the parabolic channel bears strong resemblance with the attractor found by a numerical simulation of an internal tide generated in a parabolic channel (*Drijfhout and Maas*, 2008). It also resembles the streamfunction patterns found by numerical simulations of a lake with a roughly parabolic shape (*Münnich*, 1996). In terms of the shape of the attractor, the main parameter controlling the possibility of detecting an attractor is the frequency, such that the shape of the attractor can be determined by ray tracing in a two-dimensional setting. In the last chapter of this thesis we will study fully three-dimensional domains in order to find the limitations of the semi two-dimensional approach.

6.6 Appendix

Raytracing in non-uniform stratification
Ray tracing in a uniform stratification has been used before to predict internal wave patterns, *Maas and Lam* (1995). For a depth dependent stratification $N(z)$, ray tracing is still possible as long as the wave length is much smaller than the scale over which the buoyancy frequency changes (*Baines*, 1973; *Lighthill*, 1978). The starting point remains the spatial Poincaré equation for the (spatial part of the) streamfunction

$$(\partial_{xx} - c^2(z)\partial_{zz})\Psi = 0, \tag{6.1}$$

now, neglecting rotation, with $c^2(z) = \frac{\omega^2}{N(z)^2 - \omega^2}$. This is

$$(\partial_x - c(z)\partial_z)(\partial_x + c(z)\partial_z)\Psi = 0, \tag{6.2}$$

assuming that $cc_z\Psi_z$ is much smaller than $c^2\Psi_{zz}$. This assumption in fact demands that the waves are smaller than the typical length scale over which the stratification changes, a small wave or WKB limit. The characteristics (rays) are curved lines along which Ψ =constant, defined by

$$(\partial_x \pm c(z)\partial_z)\Psi = 0 \equiv \frac{d}{dx}\Psi(x, z(x)), \tag{6.3}$$

when we interpret the changing stratification as a modification of the coordinates $\frac{dz}{dx} \equiv \pm c(z)$. When we insert the approximation of our non-uniform stratification, section 6.3.3, we find

$$\pm dx = \int \sqrt{\frac{N_0^2}{\omega^2} - 1 + \frac{N_1^2}{\omega^2}\text{sech}^2\left(\frac{z - H/2}{h}\right)}dz. \tag{6.4}$$

By introducing $z = H/2 + hz'$ and $x = \sqrt{N_0^2/\omega^2 - 1}hx'$ we can rewrite this as

$$\pm dx' = \int \sqrt{1 + n^2\text{sech}^2(z')}dz', \tag{6.5}$$

where $n^2 = N_1^2/(N_0^2 - \omega^2)$. This can be integrated to find the characteristics

$$\pm x' + \xi = n\arctan\left(\frac{n\sinh(z')}{\sqrt{n^2 + \cosh^2(z')}}\right) + \text{arcsinh}\left(\frac{\sinh(z')}{\sqrt{n^2 + 1}}\right). \tag{6.6}$$

These characteristics, labeled by integration constant ξ, describe the curved rays and the ray tracing procedure is straightforward. Starting from a point at the boundary, only two possible directions remain, the inward going ones. Choosing a direction leaves one path,

Chapter 7

Tracer transport by internal wave beams

7.1   Introduction and theory

Tracer transport in deep ocean basins has been studied in order to assess vertical diffusivity, and enhanced transport near rough topography has been found (*Ledwell et al.*, 2000). Internal waves have recently gained much attention as they provide a sink for the surface tide and, subsequently, a potential source of energy for such tracer transport in the deep ocean. The internal tides, generated by tidal flow over a change in depth in the stratified environment, are often found in the shape of confined beams (*Baines*, 1974; *Pingree et al.*, 1986; *Gerkema et al.*, 2004). These confined beams have been studied extensively in the laboratory (*Peacock and Tabaei*, 2005; *Gostiaux and Dauxois*, 2007; *Echeverri et al.*, 2009). While it is well known that the subsequent interaction of these wave beams with topography, sheared currents, or changes in stratification can lead to localised mixing, remote from the energy source, it is an open question whether the confined nature of the wave beams themselves enhances transport. Spatially uniform internal waves with some weak modulation are known to feature mainly horizontal Stokes drift (*Bretherton*, 1969). Such horizontal drift of modal internal waves near a slope results in a readjustment of isopycnals to balance the drift (*Wunsch*, 1971). Vertical drift is found for internal waves when compressible effects are considered (*Coy et al.*, 1986). Here, we would like to address the question of whether confined internal wave beams also have a Stokes drift, especially in the vertical direction. We calculate the Stokes drift of viscous internal wave beams, consider particle displacements produced by a theoretical internal wave beam and compare those to laboratory observations.

The first order approximation of the Eulerian velocity field of a steady state linear, single frequency ω internal wave beam in a stratified fluid can be found from two-dimensional viscous internal wave theory (*Thomas and Stevenson*, 1972; *Hurley and Keady*, 1997; *Tabaei and Akylas*, 2003; *Voisin*, 2003). Buoyancy frequency $N = (-g\rho_*^{-1} d\rho_0/d\hat{z})^{1/2}$ characterises the stratified fluid with constant reference density ρ_* and stable stratification $\rho(\hat{z})$. The density gradient aligns with the acceleration due to gravity $\mathbf{g} = -g\mathbf{e}_{\hat{z}}$ along the vertical unit vector $\mathbf{e}_{\hat{z}}$. The buoyancy frequency is here assumed constant and for waves of fixed frequency ω, leads to wave propagation under angle $\theta = \pm \arccos(\omega/N)$ with $\mathbf{e}_{\hat{z}}$. In an infinite domain, with a tilted right-handed (x, z) coordinate system $((\xi, \eta)$ in previous chapters) that is directed along and perpendicular to the beam respectively, the streamfunction of the wave field can be written as

$$\psi(x, z, t) = \int_0^\infty Q_0(k) e^{-\beta k^3 x} \cos(kz + \omega t) dk, \qquad (7.1)$$

where t is time. This represents the far-field of one of the four beams radiating from a source at the origin. The shape of the source determines $Q_0(k)$ and typical length scale L. The energy propagates away along the beam in the positive x-direction and phases propagates in the negative z-direction. The streamfunction is an integral over all wavenumbers k and scaled kinematic viscosity $\beta = \nu/N \cos\theta \ll L^2$ preferentially attenuates the higher wavenumbers. Using this Eulerian streamfunction we continue to find the Stokes drift and the Lagrangian motion in the field away from the source. *Longuet-Higgins* (1969b) and *Wunsch* (1971) show that the Stokes drift $\mathbf{u}_s$ is to first order given by

$$\mathbf{u}_s(\mathbf{x}, t) = \int_0^t \mathbf{u}(\mathbf{x}, t') dt' \cdot \nabla \mathbf{u}(\mathbf{x}, t). \tag{7.2}$$

In terms of the streamfunction ψ, defined as $\mathbf{u} = (-\psi_z, \psi_x)$, we find in tilted coordinates that

$$u_s = \int_0^t \psi_z dt' \psi_{zx} - \int_0^t \psi_x dt' \psi_{zz}, \tag{7.3}$$

$$w_s = -\int_0^t \psi_z dt' \psi_{xx} + \int_0^t \psi_x dt' \psi_{zx}. \tag{7.4}$$

We will be interested in the period-averaged Stokes drift and, as the Eulerian velocity is periodic and therefore has a zero mean, this Stokes drift is identical to the Lagrangian drift.

$$< \mathbf{u}_L > = < \mathbf{u}_s > \equiv \frac{\omega}{2\pi} \int_0^{\frac{2\pi}{\omega}} \mathbf{u}_s dt. \tag{7.5}$$

Combining the above reveals that, in general, the calculation of the Stokes drift involves complicated multiplications of the integrals over wavenumber k. We find it illustrative to regard first the simplest version of the wave beam; a decaying plane wave with amplitude Ψ_0 and particular wavenumber $k = 2\pi/L$,

$$\psi = \Psi_0 e^{-\beta k^3 x} \cos(kz + \omega t). \tag{7.6}$$

From this expression we find that the drift along the beam is zero but that a small but constant cross-beam drift exists

$$
\begin{aligned}
< u_s > = \quad & \frac{\omega \Psi_0^2}{2\pi} \int_0^{\frac{2\pi}{\omega}} \frac{k}{\omega} e^{-\beta k^3 x} \left[\cos(kz + \omega t) - \cos(kz) \right] \beta k^4 e^{-\beta k^3 x} \sin(kz + \omega t) \\
& - \frac{\beta k^3}{\omega} e^{-\beta k^3 x} \left[\sin(kz + \omega t) - \sin(kz) \right] k^2 e^{-\beta k^3 x} \cos(kz + \omega t) dt \\
= \quad & 0, \\
< w_s > = \quad & \frac{\omega \Psi_0^2}{2\pi} \int_0^{\frac{2\pi}{\omega}} -\frac{k}{\omega} e^{-\beta k^3 x} \left[\cos(kz + \omega t) - \cos(kz) \right] \beta^2 k^6 e^{-\beta k^3 x} \cos(kz + \omega t) \\
& - \frac{\beta k^3}{\omega} e^{-\beta k^3 x} \left[\sin(kz + \omega t) - \sin(kz) \right] \beta k^4 e^{-\beta k^3 x} \sin(kz + \omega t) dt \\
= \quad & -\frac{\beta^2 k^7 \Psi_0^2}{\omega} e^{-2\beta k^3 x}.
\end{aligned}
$$

The direction of the cross-beam drift is in the direction of the phase propagation, the negative z direction. Introducing two wavenumbers k and m, we also find net drift in the along beam direction:

$$
\begin{aligned}
< u_s > = \quad & \frac{\beta \Psi_0^2}{2\omega} km(k - m)(k^2 + m^2) e^{-\beta(k^3 + m^3)x} \sin((k - m)z), \\
< w_s > = \quad & -\frac{\beta^2 \Psi_0^2}{\omega} \left[(k^7 e^{-2\beta k^3 x} + m^7 e^{-2\beta m^3 x}) + c(k, m) e^{-\beta(k^3 + m^3)x} \cos((k - m)z) \right],
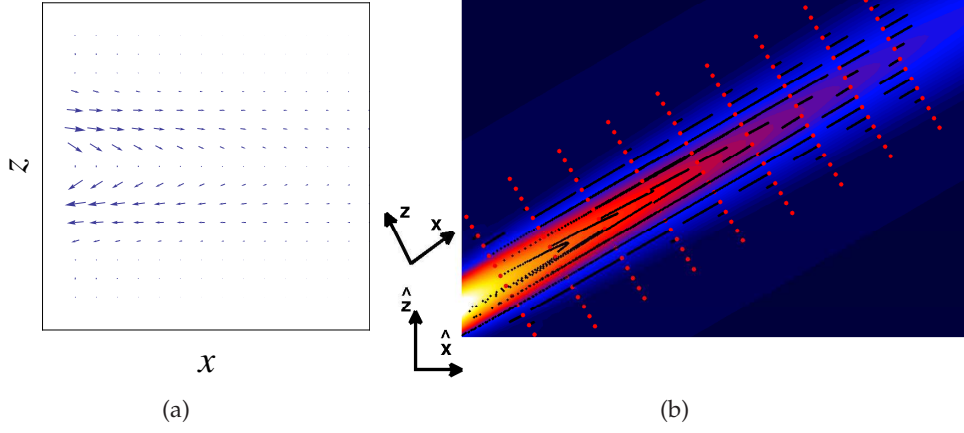\end{aligned}
$$

Figure 7.1: a) Calculated Stokes drift for a wave with five wavenumber components. b) Poincaré plot of particle positions in an inclined internal wave beam in which phase propagates downward to the right and energy upwards to the right. Starting from initial positions (red dots), the kinematic equations are integrated over 50 periods and particle positions are plotted once per period. The colour indicates the energy with values defined in figure 2.

where

$$c(k,m) = \frac{1}{2}km(k^5 + k^3m^2 + k^2m^3 + m^5).$$

The Stokes drift along the beam is stronger as $< u_s >$ is an order of $1/k^2\beta$ larger than $< w_s >$. The drift is in opposite direction on the two sides of the beam. The drift in the along-beam direction is a result of wavenumber interaction, whereas the drift in the cross-beam direction is a result of the viscous attenuation along the beam. A confined beam consists of a continuous spectrum of wavenumbers, so we also calculated the Stokes drift for more than two interacting wavenumbers using Mathematica with beams containing up to 5 wavenumbers. The more wavenumbers used, the more the structure of the drift is found to be confined to a beam as the velocities driving the transport are also more and more confined to a beam. The drift field $< \mathbf{u}_s >$ for a wave with five interacting wavenumbers is shown in figure 7.1a.

In order to find the Stokes drift of a beam, having a full spectrum of wavenumbers, we consider the Lagrangian trajectories in a beam. Instead of finding an explicit expression for $\mathbf{u}_s$, we infer from these trajectories what the Stokes drift must have been as the Eulerian mean is zero. The Lagrangian trajectories of our zero-mean streamfunction are obtained by numerical integration of the kinematic equations, $dx/dt = -\partial\psi/\partial z$ and $dz/dt = \partial\psi/\partial x$. In these equations the streamfunction acts as a nonintegrable Hamiltonian, since the time dependence in (7.1) is nonseparable, a mathematical structure known to lead to net drift (*Ottino*, 1989). The integration of (7.1), is represented by the Poincaré plot in un-tilted coordinates $(\hat{x}, \hat{z})$ in figure 7.1b. It shows that trajectories mainly run parallel to the beam, but in opposite directions on

either side of its axis. In addition, there is a small cross-beam component that makes the trajectories loop (in this case to the lower side of the beam), meaning that even particles starting on the upper side of the beam will eventually drift towards the source in the negative x-direction. The trajectories reveal a drift very similar to our calculated Stokes drift. Having the vertical $\hat{z}$-axis aligned with the stratification, we see that the Stokes drift of internal wave beams has a clear cross-isopycnal component. This is unexpected as stratification naturally prohibits net vertical motions. Two remarks should be made. First, the Stokes drift generally presents an initial behaviour of the flow. The result of this drift can prompt adjusting flows. Secondly, while the expression for the streamfunction is good to first order, we use it to study long term effects at higher order. It is therefore anticipated that other, higher order effects might also be important, notably a buoyancy flux induced mean flow (*Ou and Maas*, 1986), neglected in the present formulation. This might explain differences comparing our predictions with observed particle transport by internal wave beams in laboratory experiments.

7.2 Laboratory experiment

We want to compare the drift over many periods for a steady state internal wave beam with observations on the drift of particles in internal wave beams in the laboratory. In the confined laboratory setting, the requirement that the internal wave beam should be steady state, and be so for many periods, meets with some practical problems. Very soon after the start of an experiment, internal waves result in boundary reflections and fill the whole fluid domain, obscuring the beam structure (*Mowbray and Rarity*, 1967; *Gostiaux et al.*, 2006). Therefore, we here use the fact that, for a uniformly stratified fluid, the internal wave inclination to the vertical is maintained upon reflection from a sloping wall, so that all energy can be focussed onto an 'internal wave attractor' (IWA) (*Maas and Lam*, 1995; *Maas et al.*, 1997; *Ogilvie*, 2005) and chapter 3. This is a unique periodic orbit whose location is defined by wave frequency, stratification and geometric shape of the tank (*Maas and Lam*, 1995). We force the waves by subjecting a tank, containing a linearly stratified fluid, to a small-amplitude, horizontal oscillation and thus create a very stable IWA (chapter 4). The IWA is characterised by four clear beams (figure 7.2), each beam exhibiting the typical shear oscillation at the forcing frequency and a wavenumber spectrum similar to that of wavebeams from an oscillating source (chapter 3). In the present experiments the waves are always small-amplitude and far from breaking. The energy propagates in clockwise direction and phase propagates perpendicular to the beams. By seeding the fluid at the surface with very slowly settling particles (illuminated in a thin slice in the middle of tank), we initially observe a curtain of particles with no particles under the sloping wall (figure 7.3a). The seeding of the particles is at such low concentration that the density of the fluid is not affected. Hence the Boycott effect (*Peacock et al.*, 2005) can be neglected. A steady state IWA is reached within about 20 oscillation periods after the tank is set into motion. By the end of the experiment, after 150 periods of steady state oscillation, the initial particle pattern is displaced over many wave excursions and is molded into the shape of the IWA, figure 7.3b. We find that particles are only displaced when they are in the vicinity of the wave attractor beams. In particular, internal waves drive a transport towards the beams of the attractor.

Using standard particle image velocimetry (PIV) at fixed positions from 32 images per pe-
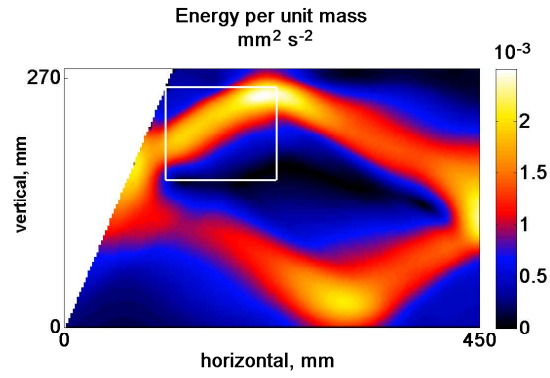
Figure 7.2: Steady state spatial distribution of potential energy of the buoyancy perturbation. The energy is concentrated around the IWA. The white rectangle indicates the region plotted in figure 7.4.
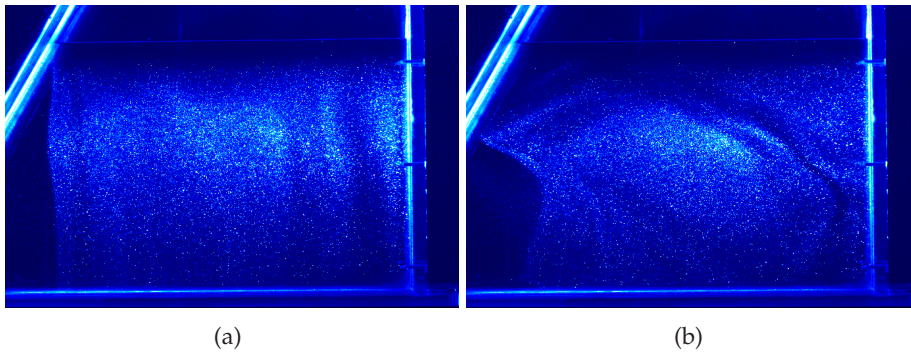

Figure 7.3: Particle distributions at a) beginning and b) end of the experiment in a vertical plane. The attractor shape becomes visible in the redistributed tracer particles.
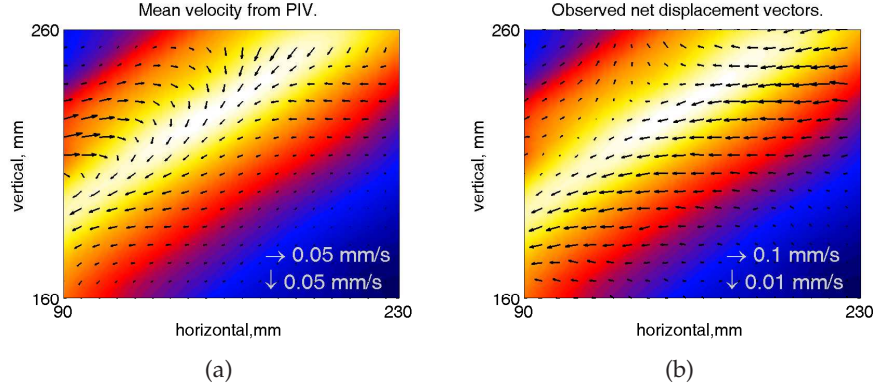
Figure 7.4: a) Average drift from PIV, in the upper left beam of figure 7.2. b) The observed average displacement of particle patterns, corrected for constant settling. The average displacement reveals a vertical drift in the centre of the beam that is an order of magnitude smaller than the horizontal drift (note the difference in scale of the velocity vectors indicated in the lower right corner). The background colourfield indicates the energy of the oscillating velocity field, with values defined in figure 7.2.

riod, the Eulerian velocity field in the vertical $(\hat{x}, \hat{z})$-plane is obtained. Averaging the oscillating field over 100 periods we find an average velocity field, figure 7.4a, that qualitatively resembles the calculated drift in figure 7.1a. Given that PIV is a hybrid Eulerian-Lagrangian technique, the existence of this average does not necessarily represent the particle drift. However, we are also able to access the directly measured net drift, obtained by following particle patterns between images that are separated by an integer number of periods. We obtain the drift for all 32 stages of the period and average over 100 periods of steady state oscillation. We correct this net motion for the slow, horizontally-uniform settling that occurs also in regions without wave motion. Doing so, this effectively gives us the motion of equivalent particles that are neutrally buoyant at their starting position. The net velocity arrows, figure 7.4b, display an essentially horizontal motion from both sides into the beam. We observe a vertical drift when we multiply the vertical velocities by a factor 10. The velocity structure shows that vertical drift, across density surfaces, still exists in the directly measured drift, though an order of magnitude weaker than the horizontal velocities. The theoretically predicted Stokes drift thus gives us a vertical drift that is too large compared to that observed for neutrally buoyant particles.

7.3 Motion of neutrally buoyant particles

To explain the difference in the vertical component of the drift, we assume that our fine particles have no inertia. Then, the only forces at work on a particle of radius R_p are drag **D** and buoyancy **B**, described by

$$\mathbf{D} = 6\pi \nu \rho_* R_p (\hat{\mathbf{v}}(\hat{x}, \hat{z}, t) - \frac{d\hat{\mathbf{x}}}{dt}), \qquad (7.7)$$

$$\mathbf{B} = \frac{4}{3}\pi R_p^3 \mathbf{g} \triangle \rho \approx \frac{4}{3}\pi R_p^3 \mathbf{g} \left(\rho_0(0) + \hat{z} d\rho_0/d\hat{z} - \rho_p \right) = -\frac{4}{3}\pi R_p^3 N^2 \rho_* \hat{z} \mathbf{e}_{\hat{z}}. \qquad (7.8)$$

Here $\Delta\rho$ is the difference between the fluid's unperturbed density, $\rho_0(\hat{z})$ at level $\hat{z}$ to which the particle is displaced vertically, and the unchanged particle density, ρ_p, which is taken identical to the average background density field, $\rho_0(0)$, at its equilibrium position $z = 0$.

Inertialess particle motion is thus governed by $\mathbf{D} + \mathbf{B} = 0$. Neglecting buoyancy, we recover the classical kinematic relationship, $d\hat{\mathbf{x}}/dt = \hat{\mathbf{v}}(\hat{x}, \hat{z}, t)$, but including $\mathbf{B}$, we find

$$\frac{d\hat{x}}{dt} = \hat{u}(\hat{x}, \hat{z}, t), \qquad (7.9)$$

$$\frac{d\hat{z}}{dt} + \hat{z}/\tau = \hat{w}(\hat{x}, \hat{z}, t), \qquad (7.10)$$

where the restoring time is $\tau = 9\nu/2(NR_p)^2$. For typical experimental values $\tau = 5$s, about the same as the forcing frequency. This shows that while during an oscillation the suppressing effect is not felt -indeed the particles make a clear vertical excursion- the net vertical migration over a period is suppressed by buoyancy. We may now compute our Lagrangian trajectories again from integrating the above equations using our expression for ψ, similar to what we did for figure 7.1b. Such integrations reveal indeed that the vertical drift is largely suppressed, but the suppression depends on the actual value of τ. What remains is a strong horizontal drift from both sides into the beam and a weak vertical drift inside the beam, as we observed on the IWA.

The observed net flow of particles also indicates that fluid is transported towards the attractor and, for the upper left branch, is transported downwards in the middle of the beam. Over long time, synthetic schlieren (*Dalziel et al.*, 2000) observations of the steady state buoyancy field indeed reveal a net density perturbation growing near the attractor. This growing perturbation is narrower than the full width of the beams, but wider than the smallest wave length observed. The pressure gradients resulting from the influx could result in either a flow in the cross-tank direction (normal to the light sheet), or in a steady return flow that matches the inflow. This latter case would be similar to the undertow near the beach, returning the water transported by the Stokes' drift accompanying incident surface waves. In the PIV data (online movie) we observe some particle motion into/out of the light sheet, this indicates velocities driving particles in the cross-view direction towards the front and end walls of the tank.

7.4   Summary and conclusion

In summary, we find net horizontal convergence of particles on internal wave beams and a vertical flux (located at the centre of the beam) in a strongly stratified fluid. The drift for our beam without viscosity is zero, as in that case all motions are perfectly rectilinear. Viscosity breaks this perfect motion, resulting in the drift. This does not mean however, that viscosity is the

only candidate to cause drift, in fact any weak mechanism that disturbs the rectilinear motions in the idealised inviscid beam is sufficient, e.g. a horizontally uniform background sloshing. In reality there will always be a such a mechanism. Averaging the oscillatory velocity field, as observed on the IWA, reveals a clear net drift. The vertical drift from the actual particle motion is an order of magnitude smaller than the horizontal drift velocity (figure 7.4b). This is not predicted by the analytical calculations of the Stokes drift. The explanation for this reduction in the vertical drift is found by considering the dynamics of neutrally buoyant particles.

The fact that drift is caused by internal wave beams may be of great relevance to the ocean (where the typical horizontal and vertical motions are also an order of magnitude apart), as it provides an enhanced vertical transport in internal wave beams, relative to the background watercolumn, even for weak linear waves. For very slowly settling particles we find enhanced or reduced sedimentation rates along the beam, depending on the energy propagation direction relative to the direction of gravity. We note that in the upper and lower left beams of the IWA, vertical transport and settling are in the same direction. In the two beams on the right side of the tank, however, vertical transport and settling act in opposite directions, and hence we observe *reduced* sedimentation in these two beams. This means that, internal wave beams affect the lifetime and transport rates of nutrients or sediments. This complements the picture of isopycnal transport of nutrients and sediment by internal interfacial waves (*Sandstrom and Elliott*, 1984; *Heathershaw et al.*, 1987; *Lennert-Cody and Franks*, 1999).

The role of diffusion remains an open question. When tracer diffusion is taken into account, vertical exchange of tracer properties could be amplified, as a result of locally higher concentrations combined with the vertical shear motion in the beam. Even weak diffusion can become effective when tracer gradients are amplified by the horizontal transport. This process could explain observations on enhanced mixing near topography (*Ledwell et al.*, 2000). We also need to distinguish passive from dynamical tracers. When considering a passive tracer (such as relatively low concentrations of nutrients or sediment) its vertical displacement will not affect the state of the fluid itself. However, vertical migration of a dynamically active tracer, such as the fluid's density that determines the state of the fluid, might lead to locally altered (horizontal) density and pressure gradients. This may modify the internal wave paths and may alter the mean circulation. The modelling of this self-consistent transport (*del Castillo-Negrete*, 2000) holds interesting non-linear behaviour.

Finally, there is a close analogy of internal gravity wave attractors with inertial wave attractors (*Rieutord et al.*, 2001; *Maas*, 2001; *Manders and Maas*, 2003). Our findings therefore suggest that in rotating stars strong transport of chemicals along attractors (*Dintrans et al.*, 1999; *Gerkema et al.*, 2008) might take place.

Chapter 8

Internal wave patterns in a paraboloid

8.1   Introduction

Stably stratified fluids support internal waves that travel under an angle with respect to gravity (*Görtler*, 1943). This angle is determined solely by the frequency of the forcing and the background stratification (*LeBlond and Mysak*, 1978). In a uniformly stratified fluid, a periodic disturbance causes the wave energy to radiate out in an internal wave cone. In an essentially two-dimensional (2D) setting, or in a cross-sectional view, this cone is reduced to the well known St Andrew's cross (*Mowbray and Rarity*, 1967) that led to the concept of internal wave beams (*Thomas and Stevenson*, 1972; *Tabaei and Akylas*, 2003). In quasi two-dimensional laboratory set-ups, these internal wave beams were observed as generated by oscillating cylinders or slopes converting surface waves into internal waves (*Mowbray and Rarity*, 1967; *Sutherland et al.*, 1999; *Baines*, 1974; *Gostiaux et al.*, 2006; *Echeverri et al.*, 2009). In the two-dimensional setting, the dispersion relation predicts that upon reflection at sloping walls, focussing or defocussing of the wave energy of these beams will occur (*Dauxois and Young*, 1999; *Mercier et al.*, 2008). In enclosed domains focussing dominates and leads to the formation of internal wave attractors (*Maas and Lam*, 1995). This theory has been verified in experimental studies, again using a quasi 2D laboratory set-up (*Maas et al.* (1997) and previous chapters).

All these laboratory experiments were in reality three-dimensional (3D), but domain and source were chosen such that the waves were essentially uniform in the transverse direction. Most studies employed schlieren methods and PIV (Particle Image Velocimetry), assuming the 2D structure valid up to first order (chapter 5). One of the canonical papers on internal waves (*Mowbray and Rarity*, 1967) was in fact observing the internal wave cone from an oscillating stick but the schlieren method used could not resolve this fully three-dimensional wave field. The observations seem to be in a plane. Up till now, only preliminary experimental work on the 3D observation of axisymmetric internal wave structures from oscillating and falling spheres has been presented (*Onu et al.*, 2003; *Yick et al.*, 2006), but no rigourous experiments have been performed on the full, non-axisymmetric 3D internal wave field structure.

Meanwhile, from the theoretical and numerical side, internal wave focussing has been considered in three dimensions (*Maas*, 2005; *Bühler and Muller*, 2007; *Drijfhout and Maas*, 2008). Especially the full three-dimensional structure of the internal wave field may lead to patterns that are not axisymmetric. Such patterns cannot be observed by standard schlieren techniques but have to be reconstructed using tomography. Predicting the patterns set by a simple disturbance in a three-dimensional enclosed domain is a mathematical difficulty and wave fields have so far only been approached by ray tracing from a point source *Maas* (2005). However, as ray tracing does not take phase and interference processes into account, it remains uncertain if 3D domains actually allow for attractors.

Although the full tomographic reconstruction of internal wave patterns in an enclosed stratified fluid has not been considered before, the general problem of tomographic reconstruction of density distributions from deflection and schlieren data has been studied before. The 3D density distributions have been reconstructed for a supersonic jet (*Faris and Byer*, 1988), the temperature field in gas-flows (*Agrawal et al.*, 1998) and the concentration field around a growing crystal (*Srivastava et al.*, 2005). In all these experiments the reconstruction is based on beam deflection by a density perturbation, the principle also underlying synthetic schlieren (*Dalziel et al.*, 2000) (sometimes known as Background Oriented Schlieren (BOS) (*Richard and Raffel*, 2001)). In

this chapter, we present the use of tomographic synthetic schlieren (*Goldhahn and Seume*, 2007) to reconstruct the 3D internal wave patterns from an oscillating sphere positioned eccentrically in a paraboloidal domain with a linearly stratified fluid.

Parabolic tank	Height		300	mm
	Radius	R	300	mm
	Distance camera	L	8500	mm
Fluid surface	Height	H	290	mm
	Radius		295	mm
	Buoyancy frequency	N	2.2	rad·s^{-1}
Forcing				
	Radius sphere		40	mm
	Radial position sphere		0.55R	
	Amplitude vertical oscillation		10	mm
	Exp 1: Period	T	5.3	s
	Exp 2: Period	$T_{attractor}$	4.3	s

Table 8.1: Parameters of experiment.

8.2 Experimental set-up

8.2.1 Synthetic schlieren

For the experiments we use a paraboloidal tank of depth 300 mm and radius $r = 300$ mm at the top. The tank is filled with a fluid which has a linear density gradient $\rho_0(z)$ in the vertical z to fluid height H. The stratification is characterised by buoyancy frequency $N = (-g\rho_*^{-1} \, d\rho_0/dz)^{1/2}$, with g the acceleration due to gravity and ρ_* the constant reference density of water. This is achieved with the use of two, computer controlled, Masterflex peristaltic pumps. The paraboloidal tank is mounted in a larger square tank which is filled with water to compensate for the distortions of the paraboloidal tank containing the stratified fluid. The distortions are most dramatic at the bottom, where the stratified fluid has its highest density. Optically, the optimal situation would be to have the same density stratification in both tanks, however, this would potentially lead to internal wave patterns in both tanks, a far from optimal situation. For these reasons, we fill the outer tank with fluid having the highest density of the stratification in the paraboloidal tank. In this way, we can observe a random dot pattern behind the two tanks on a light bank. This enables us to use synthetic schlieren (*Dalziel et al.*, 2000) to measure the internal wave motion in the inner (paraboloidal) tank. Synthetic schlieren relies on the apparent distortion of this background dot pattern due to refractive index changes resulting from density perturbations ρ when looking through the tank.

The use of synthetic schlieren for a three-dimensional density perturbation needs extra attention. Previously, *Scase and Dalziel* (2006) studied full three-dimensional internal wave patterns in an integrative manner. Although they were not able to resolve the three-dimensional
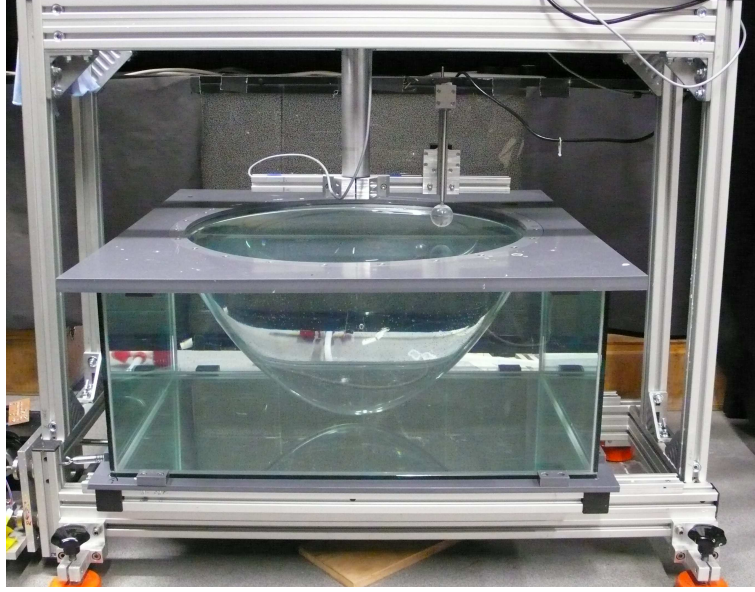
Figure 8.1: Photo of the experimental set-up. The paraboloidal tank is visible in the centre of the larger rectangular outer tank. The oscillating sphere, that can be lowered into the fluid, is located above the tank to the right of the centre, and the dot pattern on the light bank is behind the tank.

structure of the field, they were able to compare observation with a breadth-averaged (along the line of sight) result from a three-dimensional theoretical prediction. We follow their approach to find the dot-displacement vector Γ by tracing light rays through a medium with refractive index $n(x, y, z)$ over width W (the fluid) and distance B to the dot pattern. For simplicity in this discussion we shall ignore the refractive index interfaces between media, although note that necessary corrections (*Dalziel et al.*, 2007) are included in the computation employed for the results. The linearised optics, assuming small deflections to the path of light, give

$$\frac{d^2\Gamma}{dx^2} = \frac{\nabla_{(y,z)}n}{n_*},$$
(8.1)

where $\nabla_{(y,z)} = \left(\frac{\partial}{\partial y}, \frac{\partial}{\partial z}\right)$. The coordinates are the optical axis of the camera x, horizontal y and the vertical z. The origin of the coordinates is in the centre of the tank and n_* is the reference value of the refractive index. The displacements are found by integration by parts (see Appendix I for details),

$$\Gamma = \frac{\nabla_{(y,z)}}{n_*}\left[(B + \frac{1}{2}W)W < n > + \int_{-W/2}^{W/2} xn dx\right],$$
(8.2)

where $< n >= W^{-1}\int_{-W/2}^{W/2} n dx$, the average refraction through the tank. This equation shows that the sensitivity of synthetic schlieren is increased by increasing the distance to the dot pattern (B) (*Dalziel et al.*, 2000). For essentially two-dimensional perturbations of thin experiments

$(B >> W)$, $\int_{-W/2}^{W/2} x n dx$ is negligible. For a not-so-thin experiment, the sensitivity of the observations will depend on the location of the perturbations in the tank, the closer to the camera, the more sensitive. However. the 'thin experiment' approximation remains valid for any B, W whenever n is symmetric about $x = 0$.

To good approximation there is a linear relation between the refractive index and the density ρ, such that

$$\nabla_{(y,z)} n = \beta \frac{n_*}{\rho_*} \nabla_{(y,z)} \rho, \tag{8.3}$$

with $\beta \approx 0.184$ (*Weast*, 1981). This means that by measuring the apparent displacement vector Γ we can find the changes in the perturbation density gradient field

$$\Gamma = \beta \frac{\nabla_{(y,z)}}{\rho_*} \left[(B + \frac{1}{2}W)W < \rho > + \int_{-W/2}^{W/2} x\rho dx \right]. \tag{8.4}$$

Under the 'thin experiment' approximation, the displacements are obtained as gradient components of the density field, $\nabla_{(y,z)} < \rho >$. However, the tomographic reconstruction will be presented in terms of the buoyancy perturbation fields

$$b(y, z) = \frac{g}{\rho_*} \nabla_{(y,z)}^{-1} (< \rho - \rho_0 >_y, < \rho - \rho_0 >_z), \tag{8.5}$$

after integration of the gradient fields (chapter 5).

To record the apparent displacement of the dots, we use a Jai CV-M4+CL camera (1.3 MPixel monochrome). In order to minimise the parallax, the camera is positioned at distance L from the tank and is protected from disturbances in the air by a tent covering most of this optical path. Using an unperturbed reference image, the perturbed position of the dots is translated into corresponding density changes. For this comparison and data processing the DigiFlow software (Dalziel Research Partners, Cambridge) is used.

8.2.2 Tomographic reconstruction

In this section the general principles of tomography are explained; see the Appendix II for further details. For the tomographic reconstruction of the 3D internal wave field, we need to observe the experiment from many different view angles. Here we will restrict ourselves to angles of rotation ϕ about the vertical axis. For any view angle the ray deflection is measured parallel to the x'-axis, the line of sight. This indicates the introduction of the orthogonal coordinates $x' = x \cos \phi + y \sin \phi$, $y' = -x \sin \phi + y \cos \phi$, rotated at view angle ϕ from the original coordinates in the x, y plane. The original y, z at $\phi = 0$ is the plane spanned by symmetry axis and the oscillator position. This means that the projections p, i.e. the observations with synthetic schlieren, are

$$p(y'(\phi), z) = \int_{-\infty}^{\infty} b(x'(\phi), y'(\phi), z) dx', \tag{8.6}$$

where $b(x, y, z) = 0$ outside the paraboloidal tank. The reconstruction will be by means of the inverse Radon transformation or convolution-backprojection (CBP) algorithm (*Faris and Byer*,

1988; *Kak and Slaney*, 1988), see Appendix for details. At every level z the reconstruction becomes

$$b(x, y) = \int_0^{2\pi} [p(\eta) * k(\eta)]_{y'(\phi)} d\phi, \tag{8.7}$$

with $k(\eta) = \int_0^\infty Y' e^{2\pi i Y' \eta} dY'$ and convolution $[a(\eta) * b(\eta)]_\tau = \int_{-\infty}^\infty a(\eta) b(\eta - \tau) d\eta$. The transformation has become standard in all sorts of tomography and is implemented in Matlab in the image analysis toolbox as the function *iradon.m*. The function offers a routine to invert the projections, and provides simple ways of applying filters.

8.2.3   Forcing of the waves

Using the symmetry of the paraboloidal tank, the requirement of many view angles is identical to observing from the same angle but rotating the oscillating sphere under an angle ϕ about the axis of the tank. This latter, more convenient arrangement is achieved by installing a hub, holding an arm, above the centre of the tank. The arm can be rotated about the hub. The vertical oscillator mounted on the arm, drives the sphere of diameter $a = 40$ mm at a surface position $r = 0.55R$. When at rest, the sphere is above the fluid at viewangle ϕ. Before the oscillation, the sphere is lowered into the fluid, such that it is just below the surface; after the oscillation it is brought back to its original position above the fluid. For the tomographic reconstruction, views on the same plane, i.e. view angles ϕ and $\phi + 180$, are in theory identical. This means that only the view angles between 0 and 180 with a certain interval are needed to reconstruct the internal wave pattern. However, we anticipate a small effect of $\int_{-W/2}^{W/2} x\rho dx$ and perform experiments with the source on both sides of $x = 0$. We view angles in regions $[0, 180)$ and $[180 + \delta\phi/2, 360 + \delta\phi/2)$ with a $\delta\phi$ degrees interval. Under the 'thin experiment' approximation, this is identical to a $\delta\phi/2$ resolved spatial pattern in a $0 - 180$ region.

A typical experiment is as follows. In a given stratification we take a reference image before the sphere is lowered into the fluid, just below the surface. This is followed by oscillating the sphere at a given off-centred position with radius r and given angle $\phi = 0$ for 30 periods T at frequency $\omega \equiv 2\pi/T$, capturing 32 frames per oscillation. When finished, the sphere is brought out of the fluid again and the angle is increased by $\phi + 92$. Then, the system is allowed to settle for 2 minutes, typically twice the time needed for the internal waves to dissipate in the fluid. After this pause, the process is repeated from taking the reference onward. The following view angles are $\phi + 182$ and $\phi + 270$, after which the arm is returned to the initial ϕ and the whole loop is repeated for $\phi = \phi + \delta\phi$, until the views are overlapping. In the present paper $\delta\phi = 4°$ giving 90 views of the experiment.

8.3   Results

We present data from an experiment with forcing frequency ω. Although set-up and typical modus operandi are explained in the previous sections, we will highlight some of the crucial steps in this (time consuming) routine. Running the experiment for all angles with interval $\delta\phi = 4°$ takes about 11 hours. We verify that the stratification remains constant throughout the

experiment. Only at the surface, a shallow mixed layer is found, but its maximum depth is less than 15 mm. We analyse the last three periods of the oscillation of all separate experiments and perform harmonic analysis (HA) at the forcing frequency. This results in a complex integrated buoyancy field $p(y', z)$ for every angle ϕ, of which the real part is shown in figure 8.2 for some values of ϕ. The common picture arises with a source from where the internal waves radiate under the typical angle θ, a half version of the familiar 2D St. Andrew's cross (*Görtler*, 1943; *Mowbray and Rarity*, 1967). From all view angles, the beams reflect from the walls and weaken in amplitude further away from the source. The patterns seen are different per view angle ϕ, but all feature the reflection into the surface corners where the waves weaken due to defocussing. Notice that, although the data from different angles reveal different patterns, the waves always have the same angle with the vertical in the synthetic schlieren data.
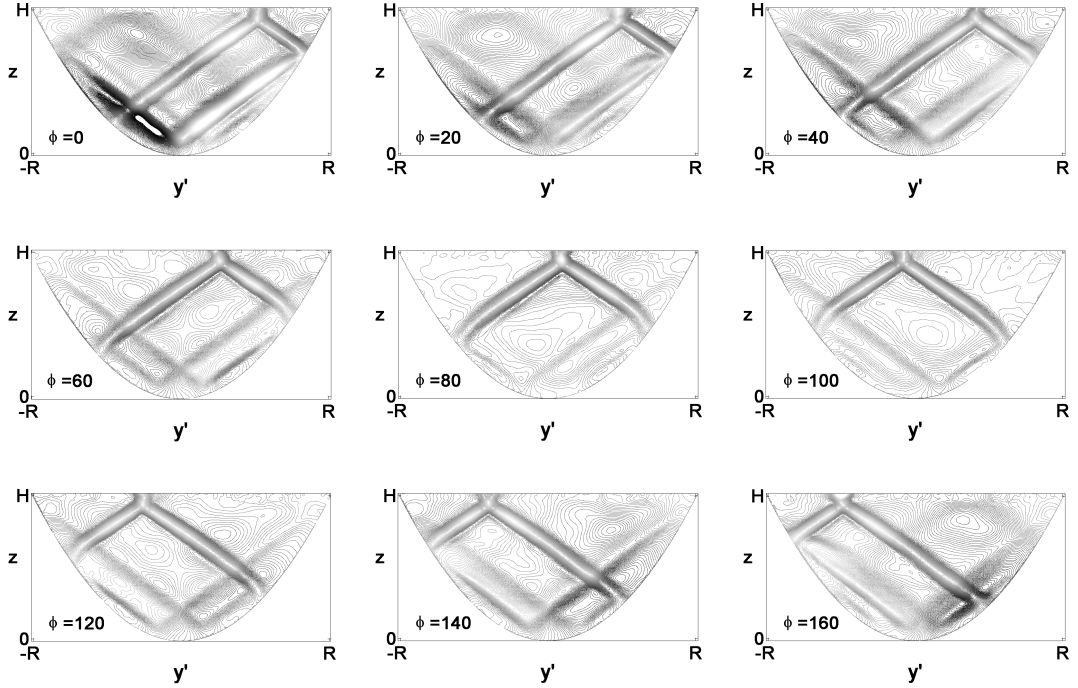
Figure 8.2: Selection of projections after harmonic analysis at the forcing frequency of experiment I. The contour lines are colour-coded, values defined defined in colourbar.

Using these projections $p(y', z)$ we perform the tomographic reconstruction for every level z following (8.7). As an example, we show the reconstruction of $b(x, y, z = H/2)$. First, we obtain all projections $p(y', \phi)$, figure 8.3a, and reconstruct $b(x, y, z = H/2)$, figure 8.3b. Clearly seen in the reconstruction is part of an internal wave ring on the left. Note that this example presents only the reconstruction of the real part of the complex projections. The reconstruction is naturally done for both real and imaginary part and combined again to form the complex $b(x, y, z = H/2)$. This means that also temporal (phase) information can be found from the

reconstruction.

The next step in the analysis is then to build the full three-dimensional field using the highest angular resolution. The spatial patterns in the paraboloidal tank are most easily appreciated when plotting some slices of the real component of the reconstruction, figure 8.4. It is seen that the internal wave ring (actually, the cone), grows wider and wider in the downward direction, and that the reflections from the walls distort the circular shape. To understand this picture we add rays coming from a point source at a location approximately at the position of the sphere in the experiment, figure 8.4b. We plot the first five reflections, and note that the rays and reconstruction coincide closely, at least globally. Local convergence of rays leads to a higher response of the fluid seen in the amplitude plot, and the rays connect regions of equal phase, figure 8.4c,d.

Here we have elected to reconstruct the 3D buoyancy field $b(x, y, z)$. Until recently, most synthetic schlieren data were presented in terms of the vertical component of the gradient field, as this comes naturally from the observations (chapter 5). However, we feel it is more desirable to work with the buoyancy field obtained upon integration of $b_{y'}$ and b_z. We tried the reconstruction of $b_{y'}(x, y, z)$ and $b_z(x, y, z)$ but found that due to the symmetries in the observations, the reconstruction of $b_{y'}(x, y, z)$ is not possible. Since our oscillation is in the vertical, the $b_{y'}$ is antisymmetric with respect to the source, this leads to an inconsistency when viewing the field from the other side ($\phi = 180°$) and means a naïve reconstruction is zero. However, reconstruction of $b_z(x, y, z)$, related to the perturbation in N, is possible. In cases where the interest of the data is in the fine structure of the internal wave field this may be the preferred field, due to the highlighting of fine scales as result of the derivative.

(a)   (b)
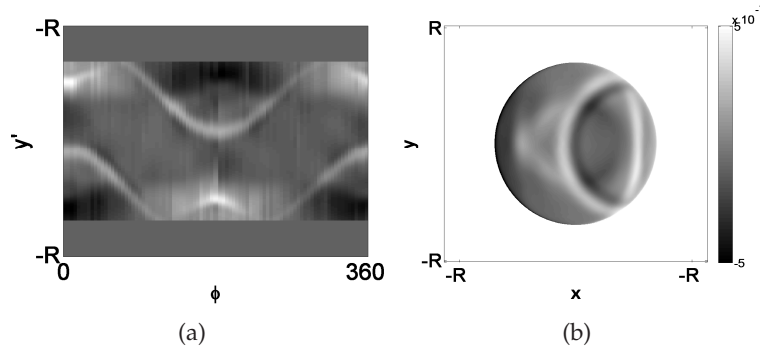
Figure 8.3: a) Projection $p(y'(\phi), z = H/2)$ and b) reconstruction of $b(x, y, z = H/2)$ with angular resolution 4 degrees.

8.4   Observations of a 3D Attractor

By following the first few reflections of some rays, we obtain a fair approximation of the wave structure. Following the rays for some more reflections leads, for some frequencies, to attractors *Maas* (2005). We select such a frequency, $\omega_{attractor}$, for experiment 2 and leave all other

Figure 8.4: Sliceplot of $b(x, y, z)$. a) Real part of HA, b) real part of HA including rays from point at surface for 5 reflections, c) amplitude and d) phase from HA.

settings as in the previous experiment. Again, upon inspection of the snapshots of the observations after harmonic analysis, figure 8.5, we find the half St. Andrews cross. Compared to Experiment I, the main difference is that there seems to be a background patter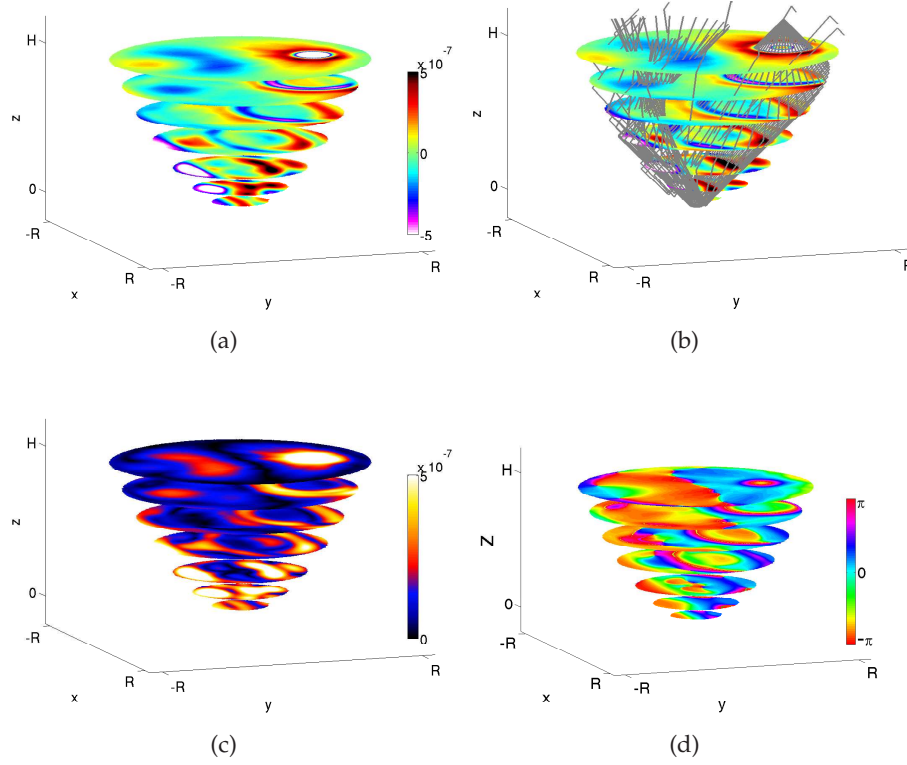n, persistent in all views, corresponding with the attractor path we find from ray tracing and experiments in a parabolic channel (chapter 6). This pattern is particularly visible in the all projections of the planes perpendicular to the source, $\phi = 80 - 100$, and in the planes aligning with the source, $\phi = 0 - 20$ (most of them not shown in figure 8.5). We then proceed, as in the previous experiment, to reconstruct the 3D density disturbance and compare it with ray tracing from a cone at the surface.

In the 3D reconstruction, figure 8.6a, the main signal shows the structure as found from the first 6 reflections (gray rays) of the incoming internal wave cone. Again the internal wave cone is deformed by reflection from the walls leading to energy focussing near the wall opposite to the oscillating sphere. The region of focussing of the rays corresponds with the region of strong internal wave motion, the black and white region in figure 8.6a. There remain some regions, however, where there is a dominant signal that has no ray convergence in the first reflection, indicated by the two arrows. These regions correspond to the region where attractors are found

after about 30 reflections of the rays, indicated by the red rays indicating reflections 30-50 in figure 8.6b. Note that the ray tracing leads to a convergence of rays on attractors near the vertical plane perpendicular to the vertical plane of the forcing and the middle of the tank.
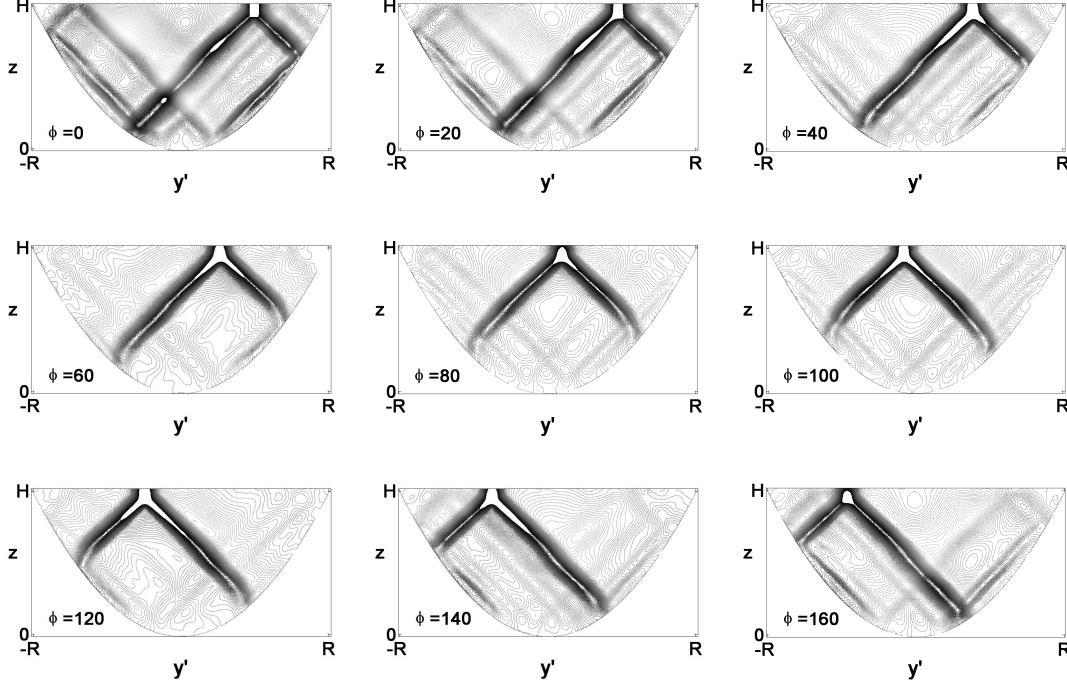

Figure 8.5: Same as 8.2 but with forcing frequency $\omega_{attractor}$.

8.5 Sensitivity of results

The reconstructions in previous sections were done with rather high angular resolution, $\delta\phi = 4°$. To investigate the sensitivity of the reconstruction to the angular resolution $\delta\phi$, the reconstruction is also performed with a subset of the projections. The reconstructions for $\delta\phi = 12, 24°$ show that, with relatively limited views, a rough idea of the field can still be reconstructed, though the reconstruction loses sensitivity as the views overlap less, figures 8.7b,c.

In order to check if the 'thin experiment' approximation is still valid for our not-so-thin experiment, we could compare observations with the source in front and back ($\phi = 90$ and $\phi = 270$) of the tank, as for a 'thin experiment' these would be identical. However, we did not capture these overlapping views (see section 8.2.3). Instead, we choose to perform the reconstruction again, exploiting the symmetry of our experiment in a different way. Knowing the symmetry of our wavefield about $x = 0$ we perform a new reconstuction by simply converting all $\phi > 180 \rightarrow \phi' = \phi - 180$. We compare this 'thin experiment' reconstruction with the reconstruction as presented in previous sections, along the x-axis, $b(x, 0, H/2)$ see figure
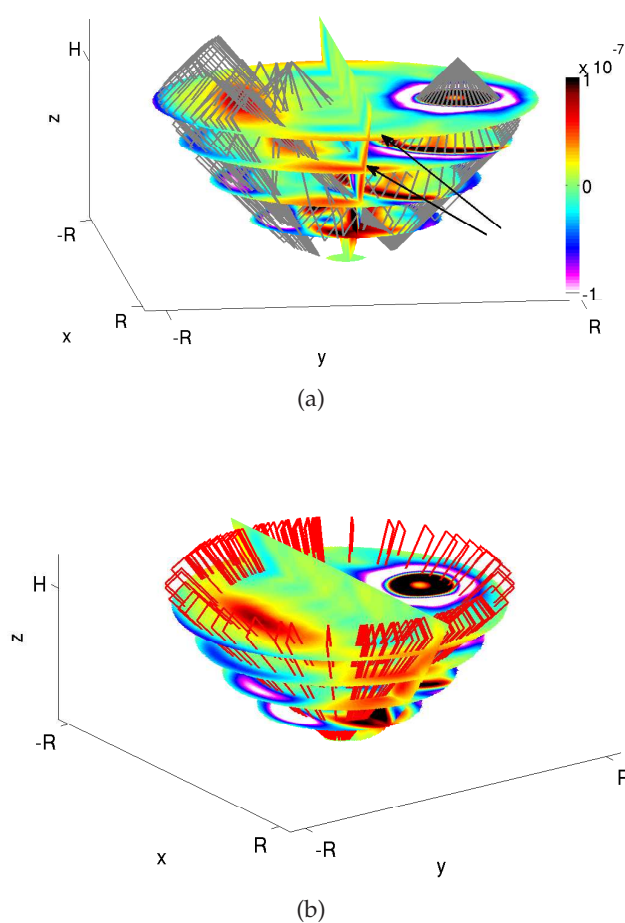
Figure 8.6: Comparison of reconstructed buoyancy perturbation with ray tracing showing a) the first six reflections (gray rays) and b) after 30-50 reflections (red rays). The arrows in a) indicate motion associated with the attractors found in b).
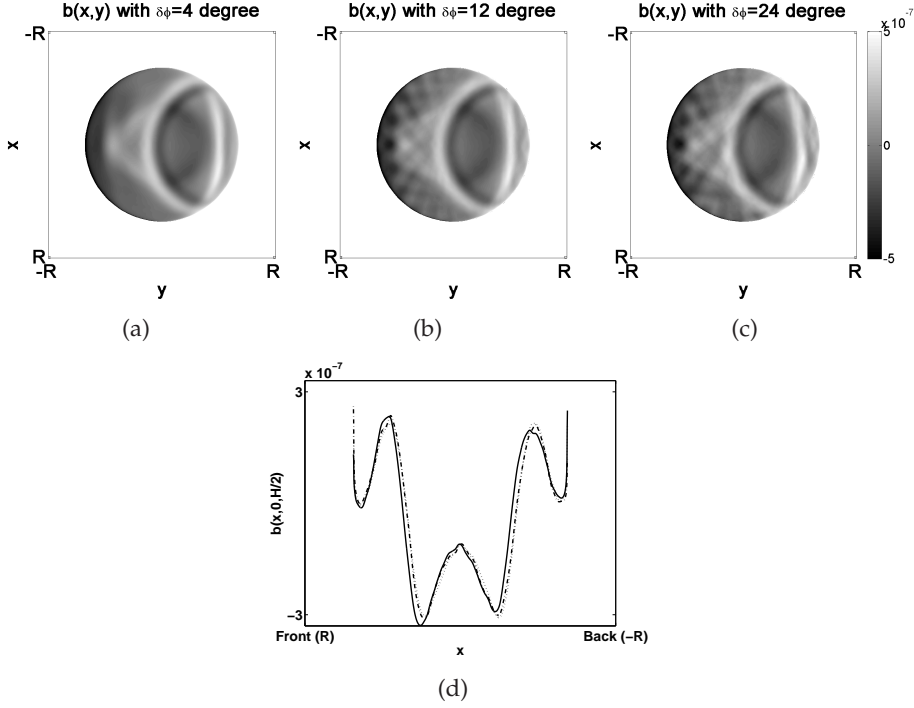
Figure 8.7: Reconstruction of $b(x, y, z = H/2)$ with angular resolution a) 4 degrees, b) 12 degrees and c) 24 degrees. d) Reconstruction $b(x, y = 0, z = H/2)$ as in previous sections (solid line), for the thin experiment (dash-dot line) and the centred experiment (dotted line).

8.7. The solid line gives the reconstruction as in previous sections, the dotted line gives the reconstruction under the thin experiment assumption. As expected, the original reconstruction had a different value of b in front and back of the tank, due to the sensitivity change. This difference is largely removed in the new reconstruction. Both reconstructions are equal along y. However, the differences are small and do not change the qualitative shape.

Using the symmetry once more, we can also average observations from ϕ and $180 - \phi$, by horizontally flipping one of the two. This means we can remove any error related to the tank not being perfectly normal with the line of sight. In doing so we find that this 'centred' reconstruction is not very different from the thin experiment reconstruction. This indicates the alignment of the camera is not of major importance for the reconstruction, though it may be optimised by ensuring that the middle of the tank is in the middle of the view.

8.6   Discussion and conclusion

The three-dimensional internal wave field from a spherical oscillator in a paraboloidal domain was successfully reconstructed using tomographic synthetic schlieren. The data were not captured instantaneously but rather in a succession of separate experiments exploiting the sym-

metries of the domain. This could be done as the stratification was very stable and experiments prove highly repeatable, even over many hours.

The reconstruction of the full 3D internal wave field from the oscillating sphere at the surface compares well with ray tracing the internal wave cone from a point source at the same position. At points where rays converge, the observed wave energy peaks. However, the fact that the ray tracing works well may also come as a surprise since information about amplitude and phase, and the effect of viscosity, cannot be found by means of this technique. Clearly visible in the observations is the decay of the amplitude of the internal wave cone as it radiates outwards, and phase structure discontinuities where many reflecting waves come together. However, the ray tracing does predict convergence of wave energy onto attractors, for specific forcing frequencies, at locations that in the observations also reveal strong wave motion.

In addition to considering the stationary internal wave field, the initial development of the internal wave field is accessible. Unfortunately, the presentation of the evolution of 3D data proves very difficult to present in a 2D environment, and is beyond the scope of this paper. However, one may also look into the dynamics of growth and saturation of the patterns, as has been done for the 2D internal wave attractor (chapter 3).

As demonstrated by *Maas* (2005), the distribution of attractors is dependent on the location of the source. For a centred source the attractors are equally spread out over all vertical planes according to the ray tracing. In our case, we have chosen for the situation where most of the attractors end up near the vertical plane that is perpendicular to the vertical plane through the source and the centre. Ideally, whole parameter regimes should be scanned to see if the ray tracing remains a reliable predictor of the internal wave patterns. However, the amount of data per experiment and long iterative procedures make it rather cumbersome to scan whole parameter regimes. Although this is merely a time- and cpu-consuming issue, it might help if optimized schemes for limited angle data sets could be implemented. The field of tomographic inversions is a very active and new methods are likely to bring new possibilities.

In conclusion, we have presented experiments in which we were able to reconstruct the 3D internal wave field in a paraboloidal tank with an off-centred oscillating sphere at the surface. In addition to showing the principle of tomography to work, we have demonstrated that ray tracing is a useful tool in the prediction of the internal wave patterns. In a second experiment we confirmed that the internal wave patterns in 3D converge onto internal wave attractors.

8.7 Appendix

Appendix I
Equation (8.2) is derived from

$$\frac{d^2\Gamma}{ds^2} = \frac{\nabla_{(y,z)}}{n_*}n, \tag{8.8}$$

where s is the along view coordinate and $s = 0$ at the front of the tank. We ray trace light through the refractive perturbations in the tank, $s = [0, -W]$ and to the dots pattern behind the tank, $s = [-W, -W - B]$. This means that apparent displacement vector

$$\Gamma = \int_0^{-B-W} \int_0^s \frac{d^2\Gamma}{ds'^2}ds'ds \equiv \frac{\nabla_{(y,z)}}{n_*}\int_0^{-B-W}\int_0^s nds'ds. \tag{8.9}$$

Between the tank and the dot pattern the rays are straight (no refraction; $n = 0$), so that the integral can be split

$$\boldsymbol{\Gamma} = \frac{\nabla_{(y,z)}}{n_*} \left[\int_0^{-W} \int_0^s nds'ds + \int_{-W}^{-B-W} \int_0^{-W} nds'ds \right].$$ (8.10)

Integrating by parts leads to

$$\boldsymbol{\Gamma} = \frac{\nabla_{(y,z)}}{n_*} \left[\left[s\int_0^s nds' \right]_0^{-W} - \int_0^{-W} s'nds' - B\int_0^{-W} nds' \right],$$ (8.11)

which, since $s = x - W/2$, leads to

$$\boldsymbol{\Gamma} = \frac{\nabla_{(y,z)}}{n_*} \left[(B + \frac{1}{2}W)W < n > + \int_{-W/2}^{W/2} xndx' \right],$$ (8.12)

equation (8.2), where $< n >= W^{-1} \int_{-W/2}^{W/2} ndx$, the line of sight average of n.

Appendix II

For completeness, we summarize here the 'standard' approach to tomographic reconstruction (*Faris and Byer*, 1988). The starting point for the reconstruction is a slice considered at $z = z_0$ and the measured projection obtained upon integrating the deflection fields resulting from a general refraction function $f(x, y, z)$. In the new coordinates x', y', both functions of ϕ, the x'-axis is chosen to be parallel with the rays in that projection. This means that the projection $p(y')$ can be written as

$$p(y') = \int_{-\infty}^{\infty} f(x', y')dx',$$ (8.13)

where the interest is in obtaining the as yet unknown function $f(x, y)$ from the observed projection $p(y')$. In order to find the inverse, a Fourier transform of the projection is performed

$$P(Y') \equiv \mathbb{F}_{Y'}(p(y')) = \int_{-\infty}^{\infty} p(y')e^{-2\pi \iota Y'y'}dy',$$ (8.14)

where the capital letters denote functions and coordinates in the wavenumber domain. Substituting for $p(y')$, expression (8.13), gives

$$P(Y') = \int_{-\infty}^{\infty} \int_{-\infty}^{\infty} f(x', y')dx'e^{-2\pi \iota Y'y'}dy'.$$ (8.15)

This expression can be rewritten in the un-rotated coordinates x, y using the relations $x' = x\cos\phi + y\sin\phi$ and $y' = -x\sin\phi + y\cos\phi$:

$$P(Y', \phi) = \int_{-\infty}^{\infty} \int_{-\infty}^{\infty} f(x, y)e^{-2\pi \iota Y'(-x\sin\phi + y\cos\phi)}dxdy$$ (8.16)

The integral is recognised as the 2-D Fourier transform in wavenumbers ($k = -Y'\sin\phi, l = Y'\cos\phi$)

$$P(Y', \phi) = \mathbb{F}_{k,l}(f(x, y)).$$ (8.17)

Note that the left-hand side is not expressed in variables k, l but in polar wavenumber coordinates Y', ϕ. Nevertheless, expressing the inverse Fourier transform in coordinates Y', ϕ it is possible to find $f(x, y)$. This inverse is

$$f(x,y) = \mathbb{F}_{k,l}^{-1}(P(Y',\phi)) = \int_0^{2\pi} \int_0^{\infty} Y'P(Y',\phi)e^{2\pi\iota Y'(-x\sin\phi + y\cos\phi)}dY'd\phi. \qquad (8.18)$$

Here the Y' is the Jacobian from the coordinate transformation. This result shows that, from the projections, the original function $f(x,y)$ can be found. With

$$k(\eta) = \int_{-\infty}^{\infty} Y'e^{2\pi\iota Y'\eta}dY', \qquad (8.19)$$

equation (8.18) can be written as a convolution

$$f(x,y) = \int_0^{2\pi} [p(\eta) * k(\eta)]_{y'(\phi)}d\phi, \qquad (8.20)$$

where the definition of convolution $[a(\eta) * b(\eta)]_\tau = \int_{-\infty}^{\infty} a(\eta)b(\eta - \tau)d\eta$ is used. This explains the name of the algorithm, convolution back-projection. The reconstruction can be written differently when realistic measurements, with limited spatial resolution, are considered. Then the maximum value of Y' is the Nyquist wavenumber $1/(2\Delta y')$, and a filter can be applied to cut off the higher wavenumbers.

Bibliography

Agrawal, A. K., N. K. Butuk, S. R. Gollihalli, and D. Griffin (1998), Three-dimensional rainbow schlieren tomography of a tempearture field in gas flows, *Applied Optics*, *37*, 479–485.

Arnold, V. I., and B. A. Khesin (1998), *Topological methods in hydrodynamics*, Springer-Verlag New York, Inc.

Baines, P. G. (1973), The generation of internal tides by flat-bump topography, *Deep-Sea Research*, *20*, 179–205.

Baines, P. G. (1974), The generation of internal tides over steep continental slopes, *Philosophical Transactions of the Royal Society*, *277A*, 27–58.

Benielli, D., and J. Sommeria (1998), Excitation and breaking of internal gravity waves by parametric instability, *Journal of Fluid Mechanics*, *374*, 117–144.

Boehrer, B., and C. Stevens (2005), Ray waves in a pit lake, *Geophysical Research Letters*, *24*, art. L24,608.

Bretherton, F. P. (1969), On the mean motion induced by internal gravity waves, *Journal of Fluid Mechanics*, *36*, 785–803.

Bühler, O., and C. Muller (2007), Instability and focusing of internal tides in the deep ocean, *Journal of Fluid Mechanics*, *588*, 1–28.

Cartan, M. E. (1922), Sur les petites oscillations d'une masse de fluide, *Bulletin des Sciences Mathématique*, *46*, 317–369.

Cole, S. T., D. L. Rudnick, B. A. Hodges, and J. P. Martin (2009), Observations of tidal internal wave beams at Kauai Channel, Hawaii., *Journal of Physical Oceanography*, *39*, 421–436.

Coy, L., D. C. Fritts, and J. Weinstock (1986), The stokes drift due to vertically propagating internal gravity waves in a compressible atmosphere, *Journal of the Atmospheric Sciences*, *43*, 2636–2643.

Dalziel, S. B., G. O. Hughes, and B. R. Sutherland (2000), Whole field density measurements by 'synthetic schlieren', *Experiments in Fluids*, *28*, 322–335.

Dalziel, S. B., M. Carr, K. J. Sveen, and P. A. Davies (2007), Simultaneous synthetic schlieren and piv measurements for internal solitary waves, *Measurement Science and Technology*, *18*, 533–547.

Dauxois, T., and W. R. Young (1999), Near critical reflection of internal waves, *Journal of Fluid Mechanics*, *390*, 271–295.

del Castillo-Negrete, D. (2000), Self-consistent chaotic transport in fluids and plasmas, *Chaos*, *10*, 75–88.

Dintrans, B., M. Rieutord, and L. Valdettaro (1999), Gravito-inertial waves in a rotating stratified sphere or spherical shell, *Journal of Fluid Mechanics*, *398*, 271–297.

Drijfhout, S., and L. R. M. Maas (2008), Impact of channel geometry and rotation on the trapping of internal tides, *Journal of Physical Oceanography*, *37*, 2740–2763.

Echeverri, P., M. R. Flynn, C. B. Winters, and T. Peacock (2009), Low-mode internal tide generation by topography: An experimental and numerical investigation, *Journal of Fluid Mechanics*, *636*, 91108.

Ermanyuk, E. V., and N. V. Gavrilov (2008), On internal waves generated by large-amplitude circular and rectilinear oscillations of a circular cylinder in a uniformly stratified fluid, *Journal of Fluid Mechanics*, *613*(-1), 329–356.

Faris, G. W., and R. L. Byer (1988), Three-dimensional beam-deflection optical tomography of a supersonic jet, *Applied Optics*, *27*, 5202–5212.

Fricker, P., and H. Nepf (2000), Bathymetry, stratification and internal seiche structure, *Journal of Geophysical Research*, *105*, 414,237–14,251.

Gerkema, T. (2001), Internal and interfacial tides: Beam scattering and local generation of solitary waves, *Journal of Marine Research*, *59*, 227255.

Gerkema, T., F.-P. A. Lam, and L. R. M. Maas (2004), Internal tides in the Bay of Biscay: conversion rates and seasonal effects, *Deep Sea Research II*, *51*, 2995–3008.

Gerkema, T., J. T. F. Zimmerman, L. R. M. Maas, and H. van Haren (2008), Geophysical and astrophysical fluid dynamics beyond the traditional approximation, *Reviews of Geophysics*, *46*, 1–33.

Goldhahn, E., and J. Seume (2007), The background oriented schlieren technique: sensitivity, accuracy, resolution and application to a three-dimensional denisty field, *Experiments in Fluids*, *43*, 241–249.

Gordon, D., and T. N. Stevenson (1972), Viscous effects in a vertically propagating internal wave, *Journal of Fluid Mechanics*, *56*, 629–639.

Görtler, H. (1943), Über eine Schwingungserscheinung in Flüssigkeiten mit stabiler Dichteschichtung, *Zeitschrift für Angewandte Mathematik und Mechanik*, *23*, 65–71.

Gostiaux, L., and T. Dauxois (2007), Laboratory experiments on the generation of internal tidal beams over steep slopes, *Physics of Fluids*, *19*(2), 028,102.

Gostiaux, L., T. Dauxois, H. Didelle, J. Sommeria, and S. Viboud (2006), Quantitative laboratory observations of internal wave reflection on ascending slopes, *Physics of Fluids*, *18*.

Grisouard, N., C. Staquet, and I. Pairaud (2008), Numerical simulation of a two-dimensional internal wave attractor, *Journal of Fluid Mechanics*, *614*, 1–14.

Harlander, U., and L. R. M. Maas (2007a), Two alternatives for solving hyperbolic boundary value problems of Geophysical Fluid Dynamics, *Journal of Fluid Mechanics*, *588*, 331351.

Harlander, U., and L. R. M. Maas (2007b), Internal boundary layers in a well-mixed equatorial atmosphere/ocean, *Dynamics of Atmospheres and Oceans*, *44*, 1–28.

Heathershaw, A. D., A. L. New, and P. D. Edwards (1987), Internal tides and sediment transport at the shelf break in the Celtic Sea, *Continental Shelf Research*, *7*, 485–517.

Hurley, D., and G. Keady (1997), The generation of internal waves by vibrating elliptic cylinders. part 2. approximate viscous solution, *Journal of Fluid Mechanics*, *351*, 119.

Hurley, D. G. (1969), The emission of internal waves by vibrating cylinders, *Journal of Fluid Mechanics*, *36*, 657–672.

Kak, A. C., and M. Slaney (1988), *Principles of Computerized Tomographic Imaging.*, IEEE Inc., New York: IEEE Press.

Lam, F.-P. A., and L. R. M. Maas (2008), Internal wave focusing revisited; a reanalysis and new theoretical links, *Fluid Dynamics Research*, *40*, 95–122.

Lam, F.-P. A., L. R. M. Maas, and T. Gerkema (2004), Spatial structure of tidal and residual currents as observed over the shelf break in the Bay of Biscay, *Deep Sea Research I*, *51*, 1075–1096.

LeBlond, P. H., and L. A. Mysak (1978), *Waves in the Ocean*, Elsevier Oceanography Series.

Ledwell, J. R., E. T. Montgomery, K. L. Polzin, L. C. St. Laurent, R. Schmitt, and J. M. Toole (2000), Evidence for enhanced mixing over rough topography in the abyssal ocean, *Nature, 403*, 179–182.

Lennert-Cody, C. E., and P. J. S. Franks (1999), Plankton patchiness in high-frequency internal waves, *Marine Ecology Progress series*, *186*, 59–66.

Lighthill, J. (1978), *Waves in Fluids*, Cambridge University Press.

Longuet-Higgins, M. S. (1969a), On the reflexion of wave characteristics from rough surfaces, *Journal of Fluid Mechanics*, *37*, 231–250.

Longuet-Higgins, M. S. (1969b), On the transport of mass by time-varying ocean currents, *Deep Sea Research*, *16*, 431–447.

Maas, L. R. M. (2001), Wave focussing and ensuing mean flow due to symmetry breaking in rotating fluids, *Journal of Fluid Mechanics*, *437*, 13–28.

Maas, L. R. M. (2005), Wave attractors: linear yet nonlinear, *International Journal of Bifurcation Chaos*, *15*, 2757–2782.

Maas, L. R. M. (2009), Exact analytic self-similar solution of a wave attractor field, *Physica D*, *238*, 502–505.

Maas, L. R. M., and U. Harlander (2007), Equatorial wave attractors and inertial oscillations, *Journal of Fluid Mechanics*, *570*, 47–67.

Maas, L. R. M., and F.-P. A. Lam (1995), Geometric focusing of internal waves, *Journal of Fluid Mechanics*, *300*, 1–41.

Maas, L. R. M., D. Benielli, J. Sommeria, and F.-P. A. Lam (1997), Observation of an internal wave attractor in a confined stably-stratified fluid, *Nature*, *388*, 557–561.

Magaard, L. (1962), Zur Berechnung interner Wellen in Meeresräumen mit nicht-ebenen Böden bei einer speziellen Dichteverteilung., *Kieler Meeresforschungen*, *18*, 161183.

Magaard, L. (1968), Ein Beitrag zur Theorie der internen Wellen als Störungen geostrophischer Strömungen. , *Deutsche Hydrographische Zeitschrift*, *21*, 241278.

Manders, A. M. M., and L. R. M. Maas (2003), Observations of inertial waves in a rectangular basin with one sloping boundary, *Journal of Fluid Mechanics*, *493*, 59–88.

Manders, A. M. M., and L. R. M. Maas (2004), On the three-dimensional structure of the inertial wave field in a rectangular basin with one sloping boundary, *Fluid Dynamics Research*, *35*, 1–21.

Marshall, J., A. Adcroft, C. Hill, L. Perelman, and C. Heisey (1997), A finite-volume, incompressible Navier-Stokes model for studies of the ocean on parallel computers, *Journal of Geophysical Research*, *102*, 5753–5766.

Marthur, M., and T. Peacock (2009), Internal wave beam propagation in nonuniform stratifications, *Journal of Fluid Mechanics*, *submitted*.

Mercier, M. J., N. B. Garnier, and T. Dauxois (2008), Reflection and diffraction of internal waves analyzed with the hilbert transform, *Physics of Fluids*, *20*, 086,601.

Moore, D. W., and P. G. Saffman (1969), The structure of free vertical shear layers in a rotating fluid and the motion produced by a slowly rising body, *Philosophical Transactions of the Royal Society of London. Series A*, *264*, 597–634.

Mowbray, D. E., and B. S. H. Rarity (1967), A theoretical and experimental investigation of te phase configuration of internal waves of small amplitude in a density stratified liquid, *Journal of Fluid Mechanics*, *28*, 1–16.

Munk, W., and C. Wunsch (1998), Abyssal recipes II: energetics of tidal and wind mixing, *Deep Sea Research I*, *45*, 1977–2010.

Münnich, M. (1993), On the influence of bottom topography on the vertical structure of internal seiches, Ph.D. thesis, ETH, Zürich.

Münnich, M. (1996), The influence of bottom topography on internal seiches in stratified media, *Dynamics of Atmospheres and Oceans*, 23, 257–266.

Nault, J. T., and B. R. Sutherland (2007), Internal wave transmission in nonuniform flows, *Physics of Fluids*, *19*, 016,601.

Nye, A. (2009), Scattering of internal gravity waves, Ph.D. thesis, Cambridge University.

Ogilvie, G. I. (2005), Wave attractors and the asymptotic dissipation rate of tidal disturbances, *Journal of Fluid Mechanics*, *543*, 19–44.

Ogilvie, G. I., and D. N. C. Lin (2004), Tidal dissipation in rotating giant planets, *The Astrophysical Journal*, *610*, 477–509.

Onu, K., M. R. Flynn, and B. R. Sutherland (2003), Schlieren measurement of axisymmetric internal wave amplitudes, *Experiments in Fluids*, *35*, 24–31.

Ottino, J. M. (1989), *The kinematics of mixing: stretching, chaos, and transport*, Cambridge University Press.

Ou, H. W., and L. R. M. Maas (1986), Tidal induced buoyancy flux and mean transverse circulation, *Continental Shelf Research*, *5*, 611–628.

Peacock, T., and A. Tabaei (2005), Visualization of nonlinear effects in reflecting internal wave beams, *Physics of Fluids*, *17*(6), 061,702.

Peacock, T., F. Blanchette, and J. W. M. Bush (2005), The stratified Boycott effect, *Journal of Fluid Mechanics*, *529*, 33–49.

Petruncio, E., L. Rosenfeld, and J. Paduan (1997), Observations of the internal tide in Monterey Canyon, *Journal of Physical Oceanography*, *28*, 1873–1903.

Phillips, O. M. (1977), *The Dynamics of the Upper Ocean, 2nd ed.*, Cambridge University Press.

Pingree, R., and A. New (1991), Abyssal penetration and bottom reflection of internal tidal energy in the Bay of Biscay, *Journal of Physical Oceanography*, p. 2839.

Pingree, R. D., G. T. Mardell, and A. L. New (1986), Propagation of internal tides from the upper slopes of the Bay of Biscay, *Nature*, *321*, 154–158.

Richard, H., and M. Raffel (2001), Principle and applications of the background oriented schlieren (bos) method, *Measurement Science and Technology*, *12*, 15761585.

Rieutord, M., B. Georgeot, and L. Valdettaro (2000), Wave attractors in rotating fluids: a paradigm for ill-posed Cauchy problems, *Physical Review Letters*, *85*, 4277–4280.

Rieutord, M., L. Valdettaro, and B. Georgeot (2001), Inertial waves in a rotating spherical shell: attractors and asymptotic spectrum, *Journal of Fluid Mechanics*, *435*, 103–144.

Rieutord, M., L. Valdettaro, and B. Georgeot (2002), Analysis of singular inertial modes in a spherical shell: the slender toroidal shell model, *Journal of Fluid Mechanics*, *463*, 345–360.

Sandstrom, H., and J. A. Elliott (1984), Internal tide and solitons on the Scotian Shelf: A nutrient pump at work, *Journal of Geophysical Research*, *89*, 64156426.

Scase, M. M., and S. B. Dalziel (2006), Internal wave fields generated by a translating body in a stratified fluid: an experimental comparison, *Journal of Fluid Mechanics*, *564*, 305–331.

Shine, A., and D. S. Martin (1988), Loch ness habitats observed by sonar and underwater television, *Scottish Naturalist*, *100*, 111–199.

Srivastava, A., K. Muralidhar, and P. K. Panigrahi (2005), Reconstruction of the concentration field around a growing KDP crystal with Schlieren tomography, *Applied optics*, *44*, 5381–5392.

Stewartson, K. (1971), On trapped oscillations of a rotating fluid in a thin spherical shell, *Tellus, XXII (6)*, 506–510.

Sutherland, B. R., G. O. Hughes, S. B. Dalziel, and P. F. Linden (1999), Visualisation and measurement of internal gravity waves by 'synthetic schlieren', part i: Vertically oscillating cylinder, *Journal of Fluid Mechanics*, *390*, 93–126.

Swart, A., G. L. Sleijpen, L. R. M. Maas, and J. Brandts (2007), Numerical solution of the two-dimensional Poincare equation, *Journal of Computational and Applied Mathematics*, *200 (1)*, 317–341.

Tabaei, A., and T. R. Akylas (2003), Nonlinear internal gravity wave beams, *Journal of Fluid Mechanics*, *482*, 141–161.

Thomas, N. H., and T. N. Stevenson (1972), A similarity solution for viscous internal waves, *Journal of Fluid Mechanics*, *54, part 3*, 495–506.

Thompson, R. E., and W. S. Huggett (1980), M_2 Baroclinic tides in Johnstone Strait, British Columbia, *Journal of Physical Oceanography*, *10*, 1509–1539.

Thorpe, S. A. (1968), On standing internal gravity waves of finite amplitude, *Journal of Fluid Mechanics*, *32*, 489–528.

Voisin, B. (2003), Limit states of internal wave beams, *Journal of Fluid Mechanics*, *496*, 243–293.

Weast, R. C. (1981), *Handbook of Chemistry and Physics*, CRC. Press.

Whitham, G. B. (1974), *Linear and nonlinear waves*, Wiley, New York.

Wunsch, C. (1971), Note on some Reynolds stress effects of internal waves on slopes, *Deep Sea Research*, *71*, 583–591.

Yick, K., R. Stocker, and T. Peacock (2006), Microscale synthetic schlieren, *Experiments in Fluids*, *42*, 41–48.

Nederlandse samenvatting

In een vloeistof waarin de dichtheid toeneemt met de diepte, kunnen golven onder het oppervlakte worden gevonden, de zogenaamde interne golven. In dit proefschrift wordt beschreven hoe deze golven zich gedragen in een afgesloten domein. Het lijkt voor de hand te liggen om een vloeistof in een afgesloten domein te beschouwen, aangezien een vloeistof zelf geen vorm heeft en daardoor altijd een omhullende container nodig heeft. In de literatuur betreffende interne golven is dit echter niet gebruikelijk, theoretisch werkt men liever met een half open (oneindige) tank. De reden hiervoor is dat in een afgesloten tank opeenvolgende golfreflecties in erg complexe golfpatronen kunnen resulteren. Deze interne golfpatronen zijn het onderwerp van dit proefschrift.

Een simpel voorbeeld van een interne golf in een dichtheidsgelaagde vloeistof, is de golf die kan bestaan op het oppervlak tussen bijvoorbeeld olie en water. Deze interne golven lijken sterk op de golven aan het oppervlakte van een vloeistof, dat wil zeggen op het grensvlak tussen lucht en vloeistof. Het verschil in dichtheid tussen de olie en het water bepaalt hoe sterk de terugdrijvende krachten zullen zijn. Deze krachten zullen bepalen hoe groot de uitwijkingen zullen zijn voor een gegeven verstoring en welke periodes de golven zullen hebben. Wanneer, in plaats van grensvlakken, de dichtheid geleidelijk verandert, lijken de interne golven niet meer op oppervlakte golven. Het dichtheidsprofiel zorgt ervoor dat elke verstoring van een waterpakketje in de verticaal een terugdrijvende kracht richting het oorspronkelijk dichtheidsniveau zal ondervinden. Het pakketje zal door traagheidseffecten aan dit niveau voorbijschieten en een omgekeerde beweging gaan maken, een trilling. De energie van een locale forcering zal door de afwezigheid van grensvlakken niet meer lokaal blijven. Zolang de vloeistof de forcering kan volgen, zal de energie zich langs schuine banen in de vloeistof voortplanten. De hoek die de banen maken met de verticaal wordt bepaald door de frequentie van de forcering en mate van dichtheidsverandering, de stratificatie. Deze hoek verandert niet bij reflecties aan schuine wanden en leidt tot focussering of defocussering van de energie. In bijna alle afgesloten domeinen blijkt dat de focussering de defocussering overheerst waardoor alle energie uiteindelijk op zogenaamde golfaantrekkers uitkomt. Een aantrekker is dus het pad waar, ongeacht de beginrichting of locatie, alle 'rays' op uitkomen. Door het volgen van de schuine paden in afgesloten domeinen, genaamd 'ray tracing', kunnen we zien welke aantrekkers zich vormen. Afhankelijk van de vorm van de container, stratificatie en forceringsfrequentie kunnen deze aantrekkers simpel of ingewikkeld van vorm zijn.

Een motivatie om interne golven te bestuderen komt uit de oceanografie, de oceaan is een dichtheidsgelaagde vloeistof waarin interne golven worden gevonden. De oceanen zijn gestratificeerd in zout en temperatuur als gevolg van vele geofysische processen zoals verdamp-

ing van water, koeling, menging met zoet water, enzovoort, die een rol spelen op verschillende plaatsen in de wereld. Over een tijdbestek van miljoenen jaren hebben deze processen een oceaan opgeleverd met, onder een doorgemengde laag aan het oppervlakte, een met de diepte geleidelijk toenemende dichtheid. In de diepere gedeeltes van de oceaan worden interne golven opgewekt door interactie van het getij en bodemtopografie. Voornamelijk in de buurt van continentale hellingen en onderwater bergen, worden sterke interne golfbewegingen waargenomen. Deze bewegingen zijn erg gelocaliseerd van structuur. Deze beweging bevindt zich in de diepste gedeeltes van de oceaan, juist daar waar ons begrip van de locale menging en stromingen beperkt is. Vandaar dat in de afgelopen jaren interne golven veel aandacht gekregen hebben van de oceanografische gemeenschap, ze zouden een verklaring kunnen bieden voor de onverwacht grote menging in de diepzee. In de meeste modellen spelen de randen van de oceaan een beperkte rol, of beter, men zorgt ervoor dat ze geen rol kunnen spelen. In dit proefschrift wordt beschreven hoe fundamenteel de vorming van aantrekkers is wanneer interne golven worden gevonden in een afgesloten, gelaagde vloeistof. Deze aantrekkers manifesteren zich als de locaties waar, na vele reflecties, alle golfenergie zich ophoopt. Het gegeven dat aantrekkers zo fundamenteel zijn, zou kunnen suggereren dat aantrekkers een belangrijke rol spelen in de oceaan. Maar die conclusie is een te grote stap aan de hand van dit proefschrift. De experimenten gepresenteerd in dit proefschrift zijn gedaan in kleine tanks die niet de complexiteit van een oceaan kunnen benaderen. Daarnaast zijn onze huidige metingen in de oceaan niet goed genoeg om de golfdynamica tot op de kleine schaal te kunnen oplossen. Er zijn echter ook veel meren en fjorden met een verrassend simpele topografie en waarin dichtheidsverschillen een belangrijke rol spelen. Op deze locaties zouden aantrekkers beter te bestuderen zijn en makkelijker waar te nemen. Naast de aantrekkers, bestuderen we in dit proefschrift ook het deeltjestransport veroorzaakt door interne golfbundels. Dit transport zou een verklaring kunnen geven voor gemeten concentratieverdelingen in de buurt van onderwater bergen, waar interne golven een belangrijke rol spelen.

In dit proefschrift worden de interne golven en aantrekkers bestudeerd in het laboratorium. Door het schudden van een simpele trapezoidale tank, gevuld met een gelaagde vloeistof, kunnen we kijken naar de interne golfpatronen die ontstaan. De dichtheidsprofielen hebben een geleidelijke verandering, een continue stratificatie. Het blijkt dat een kleine beweging van de gehele vloeistof genoeg is om op specifieke plaatsen erg sterke interne golven te krijgen. De uitwijkingen van de golven worden groter en groter totdat een bepaalde waarde wordt bereikt. We vinden in hoofdstuk 3 dat er een balans tot stand komt tussen de focussering van de lange golven aan de schuine wand en de demping van de korte golven door interne wrijving. Dit verklaard ook waarom er juist korte golven te zien zijn als de forcering van de tank is gestopt. Immers, de focussering bij reflectie aan de schuine wand maakt de lange golven kleiner en kleiner. We meten dit in zowel de dichtheidsvelden als de snelheidsvelden, hoofdstuk 4.

Alle beschouwingen over aantrekkers in gestratificeerde vloeistoffen worden gegeven in een tweedimensionale formulering, en de experimenten zijn natuurlijk in drie dimensies. In hoofdstuk 5 vergelijken we daarom de metingen van experimenten in het laboratorium met de uitkomsten van een tweedimensionale numerieke simulatie. We vinden dat hoewel het experiment goed beschreven kan worden in twee dimensies, de numerieke simulatie de demping van de golven onderschat. Vermoedelijk zijn in het laboratorium voornamelijk de grenslagen aan de randen van de tank hiervoor verantwoordelijk. Omdat de tweedimensionale theorie

vaak wordt gepresenteerd in termen van de stroomfunctie, bepalen we ook wat de stroomfunctie is voor onze experimenten. Het blijkt dat deze stroomfunctie veel van de voorspelde fijnstructuur mist als gevolg van visceuze demping, die in de theorie vaak wordt weggelaten. We concluderen desondanks dat de twee dimensionale beschrijving in onze nauwe tank een adequate beschrijving is.

In de eerste hoofdstukken kijken we enkel naar de simpelste aantrekkers in een tank met gladde wanden en een uniform dichtheidsprofiel. In hoofdstuk 6 verstoren we die perfecte setting van de experimenten door de gelaagdheid, frequentie of vorm van de wanden te variëren. Hoewel de veranderingen belangrijk zijn, blijkt dat de aantrekkers verrassend persistent zijn. Bij variatie van de frequentie, vinden we soms zwakke golfpatronen en soms sterke golfpatronen, die steeds overeenkomen met de voorspelling aan de hand van 'ray tracing'. De amplitudes zijn in deze gevallen zwakker maar de patronen die de golven vertonen zijn duidelijk aantrekkers. Wanneer de stratificatie een niet-uniform profiel heeft zijn de golfbanen gekromd, maar dit maakt niet dat de aantrekker verdwijnt. De interne golfpatronen vertonen vergelijkbaar gedrag als in een uniform gestratificeerde vloeistof. Het aanbrengen van een zaagtand patroon op een zijwand breekt weliswaar de coherente structuur ten dele, maar kan niet verhinderen dat de aantrekkers nog steeds bestaan. Tenslotte presenteren we een aantrekker in een parabolisch kanaal.

Zoals al eerder vermeld, bestuderen we transport door interne golfbundels. Dit transport is beschreven in hoofdstuk 7. Gedurende een langer voortgezet experiment zien we deeltjespatronen, gebruikt om de snelheidsvelden te meten, een netto verplaatsing ondergaan. De deeltjes worden door de golven horizontaal naar het midden van de bundel getransporteerd. In het midden van de bundel worden de deeltjes in de verticaal getransporteerd, tegengesteld aan de richting waarin de energie loopt. Wanneer we een twee dimensionale theoretische beschrijving van een interne goldbundel integreren in de tijd vinden we een vergelijkbaar transport van deeltjes, dat echter een te sterke verticale component heeft in vergelijking met de metingen. We verklaren dit verschil door de dichtheidsverandering in de verticaal in rekening te brengen.

Uiteindelijk verlaten we de nauwe tanks van de voorgaande hoofdstukken. We introduceren een drie-dimensionale meettechniek in hoofdstuk 8 en passen die toe om de golfpatronen in een paraboloïde te meten. De golven worden geforceerd door een oscillerende bol aan het oppervlak van de continu gestratificeerde vloeistof in de tank. De golven lopen nog steeds onder een vaste hoek met de verticaal, en lopen daarom dus langs een kegel. Deze golfkegel reflecteert aan de tankwanden, en de gemeten patronen zijn goed te verklaren met drie dimensionale 'ray tracing'. Voor een speciale frequentie vinden we sporen van interne golfenergie op locaties waar de golven pas na vele reflecties kunnen arriveren. Deze locaties blijken overeen te komen met de locaties waar de aantrekkers zich bevinden. Het blijkt dus dat ook in drie-dimensionale domeinen de golfaantrekkers bestaan en een rol spelen in de dynamica.

Dankwoord

Een oprechte dankjewel aan allen die een bijdrage (groot of klein) leverden aan het volbrengen van dit proefschrift. Mijn dagelijkse praktijk is nu al jaren een mix van Engels en Nederlands door elkaar spreken, het onderstaande stuk tekst is hier een mooi voorbeeld van.

Leo, Stuart en Arjen, de geleerde drie-eenheid, komen daarin op de eerste plaats. Het lijkt een groot risico, drie begeleiders, maar voor een onrust als ik is het heerlijk om constant tussen de verschillende opvattingen te schakelen.

Leo, vanaf de dag dat ik begon aan het project heb je me altijd weer weten te verbazen. Telkens wanneer ik dacht het nu echt te begrijpen, kwam je weer met de volgende gedachte. Voor mij waren de momenten waarop ik jou wist te verbazen, de momenten waarop ik wist dat een nieuwe paper werd geboren. Ik heb grote bewondering voor de manier waarop je steeds weer verder ziet en telkens bereid bent je kennis terzijde te zetten voor een nieuw idee. Velen spreken over interdisciplinair, jij bent het.

Stuart, working with you was a pleasure. You taught me how to make good experiments. With making, I mean designing, running and analysing them. Disregarding all heavy burdens, you always made time for me when things did not work out downstairs in the lab. With you I can always share the joy of creating nice pictures from our experiments, or better, nice movies.

Arjen, sluitpost van het trio, omdat je er vol vertrouwen in had dat de andere twee al genoeg waren. Je was van groot belang, je pragmatisme en gevoel voor relativering maakte dat ik altijd even kon binnenlopen voor een stand-van-zaken gesprekje. Al pratende ordende ik mijn gedachtes en kon dan weer verder. Juist in het laatste jaar was dat geen overbodige luxe toen bij vlagen, de tig verschillende projecten voor chaos in mijn hoofd zorgden. Daarnaast ben je de verpersoonlijking van het feit dat een goede wetenschapper, naast onderzoek doen, ook visie en beleid moet ontwikkelen.

Twee studenten uit Utrecht hebben een belangrijke bijdrage aan dit proefschrift geleverd. It was my pleasure to work with Pieter and Chrysanti(cc) in the lab. With their help more could be done and spending the long hours in the lab was much more fun with their presence.

Gedurende mijn promotie ben ik enkele maanden in Woods Hole geweest als fellow op de GFD Summerschool 07. I wish to thank staff and other fellows for the great experience. Special thanks to Claudia, who became more than a supervisor, and to Andrew.

Vele families hebben mij onderdak geboden voor langere of kortere tijd gedurende de tijden dat ik overal en nergens woonde. Bij de families Wiering en Maas op Texel voelde ik me altijd welkom. Families Dalziel-Kennedy and Scase-Turnbull made running in and out Cambridge possible and agreeable. And, when crossing the Atlantic, I could always rely on the hospitality

of family Hyatt-Cenedese on the Cape. Thank you all!

There have been extensive collaborations with scientists in France. Early in my Phd I visited Louis and Thierry in Lyon, later on I worked with Nicolas (Grenoble) and presently I am involved in work with Matthieu (Lyon). These people made me feel like being part of an internal wave family. Merci à tous!

Uiteraard speelt Huib nog immer een rol op de achtergrond en blijft de persoon voor wie ik in gedachten mijn artikelen slijp. Dank voor je immer enthousiaste steun en voor je rol in mijn vorming als wetenschapper. Ook GertJan wil ik bedanken voor stimulerende gesprekken, die gek genoeg voornamelijk in het buitenland plaatsvonden.

Dan, werken op meerdere instituten betekent ook heel veel collegae waar nooit genoeg tijd voor is om ze echt te leren kennen. Een ruwe schatting is dat ik ongeveer 10 kamergenoten heb gehad. Op het NIOZ dank ik de fysica afdeling waar ik altijd met veel genoegen aanschoof bij de morgen koffie discussies. I thank all of the Batchelor laboratory, although being on the run all the time, tea was always the rest moment of the day. Andrew, I'll never forget the dark narrow winding roads of Wales. Dank je wel, Jan Willem, altijd fijn om bij te praten in the Eagle. Op het CWI bedank ik mijn mede MAS'ers. Speciaal dank aan de promovendi met wie ik Arjen moest delen, Peter, Sjors en Julia.

Aangezien experimenten doen ook altijd een technische component heeft, zijn er altijd mensen nodig die daar dan weer verstand van hebben (naast Stuart). Van het NIOZ dank ik Erwin en Martin voor hun inspanningen met het eerste design van de oscillatie tafel. Speciale dank voor Frans, ik zal nooit vergeten hoe wij lange avonden in Cambridge maakten om alles op een andere netspanning aan te passen. Thank you also David, Rob, Neil, Trevor and John, whenever equipment needed some tinkering (small but often large) I could rely on you.

Iedere wetenschapper moet uiteindelijk zijn docenten van de middelbare school bedanken. Zij zijn het die de eerste intresse kunnen wekken. Voor mij waren dhr. Bronkhorst en dhr. Manders daarin erg belangrijk, dank.

Op het grensvlak van het leven binnen en buiten de wetenschap is trouwe klim-, sport- en wetenschaps-vriend Paul. Naast promoveren was er ook dansen, onderbroken door mijn vele afwezigheid, maar toch als het kon heerlijk, dank je wel Rian.

Gavin thank you, whenever, wherever, it's always a pleasure meeting you. Dank ook voor mijn Utrechtse vrienden, Merlijn, Jelmer en Noor en allen die ik te weinig zag de laatste jaren. Mijn oudste vrienden Jesse, Merel, Linde, Pepijn & Kelly dank voor jullie!

Ruben, speciale vermelding voor jou, lieve vriend dank voor wie en wat je bent! Daar hoef ik niets aan toe te voegen en dat doe ik ook niet.

Remie, Jeltje en Liesbeth dit boekje is ook van jullie. Grootmoeder, dank! voor de jaren in Utrecht en voor alles wat we samen beleven. Thijs en Claes, lieve broers wat moet ik zonder jullie constante vraag naar wat echt belangrijk is.

Annemieke, de aantrekker waar mijn leven om draait, dankjewel, voor je geduld als ik weer eens weg moest en voor je liefde.

Curriculum Vitae

Jeroen Hazewinkel was born on 20 December 1980 in Nijmegen. He received his education at the local Waldorf school and obtained his 'VWO' degree in 1999. He moved to Utrecht to study (astro)physics at the University of Utrecht. During the first years in college, he tried to study all disciplines but was soon forced to choose one major. This major was Meteorology and Physical Oceanography for which he also studied for half a year in Bergen, Norway and for some months on Svalbard, (Spitsbergen). He wrote a Masters thesis about the dynamics of tidal inlets and graduated in September 2005. In early 2006 Jeroen started as a PhD researcher at the Royal Netherlands Institute for Sea Research NIOZ, Texel. In the following four years he divided his time between the NIOZ, the Department of Applied Mathematics and Theoretical Physics (DAMTP) of the University of Cambridge and the Centrum Wiskunde & Informatica in Amsterdam. This thesis is the result of those years. In summer 2007, he was also a fellow in the Geophysical Fluid Dynamics Program hosted at Woods Hole Oceanographic Institution. Presently, Jeroen works as a postdoctoral researcher at the Scripps Institution of Oceanography, USA.